LAWRENCE
LIVERMORE
NATIONAL
LABORATORY

LLNL-TH-407435

The affect of erbium hydride on the conversion efficience to accelerated protons from ultra-shsort pulse laser irradiated foils

D.T. Offermann

October 2, 2008

Disclaimer

This work performed under the auspices of the U.S. Department of Energy by Lawrence Livermore National Laboratory under Contract DE-AC52-07NA27344.

THE AFFECT OF ERBIUM HYDRIDE ON THE CONVERSION EFFICIENCY TO ACCELERATED PROTONS FROM ULTRA-SHORT PULSE LASER IRRADIATED FOILS

DISSERTATION

Presented in Partial Fulfillment of the Requirements for
the Degree Doctor of Philosophy in the
Graduate School of The Ohio State University

By

Dustin Theodore Offermann, M.S., B.S.

* * * * *

The Ohio State University

2008

Dissertation Committee:

Doctor Linn D. Van Woerkom, Adviser
Doctor Richard R. Freeman
Professor Richard J. Furnstahl
Doctor Richard E. Hughes

Approved by

Adviser
Graduate Program in
Physics

ABSTRACT

This thesis work explores, experimentally, the potential gains in the conversion efficiency from ultra-intense laser light to proton beams using erbium hydride coatings. For years, it has been known that contaminants at the rear surface of an ultra-intense laser irradiated thin foil will be accelerated to multi-MeV. Inertial Confinement Fusion fast ignition using proton beams as the igniter source requires of about 10^{16} protons with an average energy of about $3MeV$. This is far more than the 10^{12} protons available in the contaminant layer. Target designs must include some form of a hydrogen rich coating that can be made thick enough to support the beam requirements of fast ignition. Work with computer simulations of thin foils suggest the atomic mass of the non-hydrogen atoms in the surface layer has a strong affect on the conversion efficiency to protons. For example, the $167amu$ erbium atoms will take less energy away from the proton beam than a coating using carbon with a mass of $12amu$. A pure hydrogen coating would be ideal, but technologically is not feasible at this time.

In the experiments performed for my thesis, ErH_3 coatings on $5\mu m$ gold foils are compared with typical contaminants which are approximately equivalent to $CH_{1.7}$. It will be shown that there was a factor of 1.25 ± 0.19 improvement in the conversion efficiency for protons above $3MeV$ using erbium hydride using the Callisto laser. Callisto is a $10J$ per pulse, $800nm$ wavelength laser with a pulse duration of $200fs$

and can be focused to a peak intensity of about $5 \times 10^{19} W/cm^2$. The total number of protons from either target type was on the order of 10^{10}. Furthermore, the same experiment was performed on the Titan laser, which has a $500fs$ pulse duration, $150J$ of energy and can be focused to about $3 \times 10^{20} W/cm^2$. In this experiment 10^{12} protons were seen from both erbium hydride and contaminants on $14\mu m$ gold foils. Significant improvements were also observed but possibly because of the depletion of hydrogen in the contaminant layer case.

To my loving wife, Lien-Shin. You have been my support and my motivation.

ACKNOWLEDGMENTS

There are a great number of people and organization that I would like to acknowledge and thank for their contributions to my work over the last six years. First and foremost I wish to thank my wife and family for standing by me while I finish my time as a graduate student. I also would like to express my gratitude to my thesis advisor, Linn Van Woerkom. Not once in the time that I have known him have I had any differences with him both professionally and personally. His guidance and leadership have always been inspirational. I also feel I owe him for the opportunities I now have in my professional life. Because him and Rick Freeman I have been working and interacting with the scientists and laboratory equipment of two of our country's top national laboratories. At these labs, I have made many contacts with leaders in our field. Rick Freeman has been like a second advisor for me ever since he combined his research group with ours a few years ago. It is directly because of Rick Freeman and his presence in the in the High Energy Density Physics field that our research has been geared toward fast ignition inertial confinement fusion. I also want to thank Andy Mackinnon, Mike Key, Prav Patel, and Andrew MacPhee at Lawrence Livermore National Laboratory. For the last two and a half years, these scientist have been my research advisors for me while I have been away from my home base in Ohio. Over the last three years I have been funded and working at Lawrence Livermore National Laboratory.

Every experimental campaign at a large laser facility such as Titan or Callisto requires a team effort. From the set up of all the precision diagnostics and their operation to the planning of the experiment and the purchasing and design of parts and targets, I thank every member of our group at the Ohio State University and our collaboration. Farhat Beg and his students and postdocs of the University of California, San Diego, Rich Stephens and Kramer Akli of General Atomics, Ying Tsui from the University of Alberta, Clif Chen from the Massachusetts Institute of Technology, and all the members the Ohio State University High Energy Density research group, thank you all.

For the two experiments performed for this thesis work, I would not have any results to speak of if were not for the skills and the dedication of the staff of the Jupiter Laser Facility. Specifically I want to tank Dwight Price, Steven Maricle, Rich Combs, Jim Bonlie, Gary Freeze, Roger van Maren, and Jim Hunter. Each of these individuals were able to provide me with my specific request for laser beam configurations and hardware at the target chambers.

Also at Lawrence Livermore National Laboratory, I want to acknowledge the work of Jorge Sanchez, Yuan Ping, Nan Shen, and Walter Unites. Much of the planning of the erbium hydride targets and the etching system use to clean them was done by these individuals. The targets themselves were made and tested by Loren Espada at Sandia National Laboratory.

Simulation for this work were performed by Mark Foord of Lawrence Livermore National Laboratory and by Teresa Bartal of the University of California, San Diego. Calculation for the ionization potentials of gold were provided by Stephanie Hansen of Lawrence Livermore National Laboratory.

VITA

August 2005	M.S. in Physics, The Ohio State University, Columbus, Ohio
June 2002	B.S. in Physics, Seattle University, Seattle, Washington
September 2005 - Present	ILSA Grant, Lawrence Livermore National Laboratory, Livermore, California
January 2005 - Present	Graduate Research Associate, The Ohio State University, Columbus, Ohio
September 2003 - December 2005	Graduate Teacher Associate, The Ohio State University, Columbus, Ohio
January 1999 - June 2002	Teaching Assistant, Seattle University, Seattle, Washington
September 2002	Department of Physics Fellowship, The Ohio State University, Columbus, Ohio
August 2001	Nuclear Energy Research Fellowship, Argonne National Laboratory -West, Idaho
September 2000 - June 2002	Bannan Scholarship, Seattle University, Seattle, Washington
September 1998 - June 2002	Trustee Scholarship, Seattle University, Seattle, Washington

PUBLICATIONS

Research Publications

L. Van Woerkom, K.U. Akli, T. Bartal, *et al*, *Fast electron generation in cones with ultra-intense laser pulses*, Phys. Plasmas, **15**, 056304, 2008.

J. Pasley, M. Wei, E. Shipton, *et al*, *Experimental observations of transport of picosecond laser generated electrons in a nail-like target*, Phys. Plasmas, **14**, 120701, 2007.

A. Link, E.A. Chowdhury, J.T. Morrison, *et al Development of an in situ peak intensity measurement method for ultraintense single shot laser-plasma experiments at the Sandia Z petawatt facility*, Rev. Sci. Instrum., **77**, 10E723, 2006.

Conference Presentations

D.T. Offermann, L.D. Van Woerkom, R.R. Freeman, *et al*, *Observations of Improvement in Conversion Efficiency to Laser Accelerated Protons Using Er-Hydride Coated Targets*, The American Physical Society, High Energy Density Physics April Meeting, 2007.

D.T. Offermann, L.D. Van Woerkom, R.R. Freeman, *et al*, *Observations of the Effect of Er-Hydride Targets on the Conversion Efficiency to Laser Accelerated Protons*, The American Physical Society, Division of Plasma Physics, 2007.

FIELDS OF STUDY

Major Field: Physics

TABLE OF CONTENTS

Chapters:

Appendices:

LIST OF TABLES

Table **Page**

LIST OF FIGURES

Figure **Page**

CHAPTER 1

INTRODUCTION

The eventual goal of man made fusion energy for the benefit of all seems to be perpetually twenty years away. The nuclear reactions which keep the stars burning can be reproduced in laboratory conditions or in thermonuclear weapons. Getting those same reactions to produce energy in a self-sustaining way while producing more energy than what is needed to feed the reaction at the scale of a power plant is still in development. The promise of fusion energy is a clean burning, nearly inexhaustible supply of fuel with little in the way of waste products. This is a wonderful promise when contrasted with green house gas emitting fossil fuels or fission reactors producing toxic, radioactive waste which must be stored for ten thousand years to be safe. One approach to this has been Inertial Confinement Fusion (ICF), which is discussed in more detail in the sections to follow. Inertial Confinement Fusion has been under development for several decades.

It is the goal of this thesis work to address a very specific problem on the path to a particular approach to high gain, laboratory scale fusion. A necessary challenge to overcome in Inertial Confinement Fusion with fast ignition schemes involving proton beams as the igniter is to improve the conversion efficiency from laser energy to the proton beam energy. The following work will present results from two experiments performed at Lawrence Livermore National Laboratory's (LLNL) Jupiter Laser Facility (JLF) where the use of heavy hydrides was explored as an attempt to achieve this goal. Computer simulated plasma experiments and estimations from basic Newtonian physics suggest that heavy hydrides have advantages in producing energetic proton beam when compared with lighter hydrides.

1.1 THESIS OUTLINE

The introductory chapter of this thesis begins by discussing the underlining principles of Inertial Confinement Fusion. This is to establish the purpose and ultimate motivation of the experiments conducted. As ICF is discussed, the distinction between hotspot ignition and fast ignition is presented. Fast ignition, as will be seen, has obvious energy advantages over hotspot ignition, but comes with its own share of technical challenges. The distinction between electron driven fast ignition and proton driven fast ignition is also made. Lastly, the challenges of generating proton beams which can satisfy the requirements for ignition are highlighted.

Theories of ion acceleration are presented in chapter 2. A summary of the solution of the 1-D expansion of a plasma into the vacuum as it is found in the literature on this subject is given. Next the results of simulations also available in the literature on how the surface composition and ion mass influence how energy partitions into the various accelerated ion species are shown. Further simulations were also performed to match and predict the conditions of the experiments conducted for this thesis work. Those results are also shown in chapter as well.

Chapter 3 is about the diagnostic tools used in the experiment to collect the proton and ion data. Details of the two primary diagnostics, radiochromic film packs and a Thomson parabola spectrometer, are given. Each diagnostic required calibration. The radiochromic film in particular required a visit to a proton cyclotron facility to acquire a proton dose response function. The methods used to analyze the data and produce the relevant physical information are included.

Finally, in chapter 4, the results of the two experiments conducted comparing erbium hydride with naturally occurring containment layers found on foils are presented. Here it will be shown that erbium hydride does improve proton conversion efficiency and that the result is consistent with the simulations from chapter 2. In chapter 4, proton data from two other experiments will be presented with the intent of suggesting further challenges on conversion efficiency due to enclosing cone structures that will be a necessary design feature of any proton fast ignition scheme.

1.2 INERTIAL CONFINEMENT FUSION

Inertial Confinement Fusion has been the focus of the United States fusion energy research program for the last several decades [1]. ICF differs from the leading competitive scheme of Magnetic Confinement Fusion (MCF) fundamentally in how the hydrogen isotope fuel remains assembled long enough to burn a sufficient fraction. In magnetic confinement the hydrogen rich plasma is held together by strong magnetics which interact with the current of moving ions in the plasma. For inertial confinement, the freely expanding plasma itself is assembled in such a way that the burn wave outruns the expansion. International efforts as well as domestic attempts at MCF have been underway for several decades. Most notable is ITER [2]. ITER is an acronym for International Tokomak Experimental Reactor. It is a multi-billion dollar project which by the year 2021 is expected the demonstrate the first burning magnetically confined fusion. The term burning specifically refers to a self-sustaining consumption of fuel. A Tokomak style reactor is a toroidal chamber where the plasma flows through it. For MCF to work, the time in which the fuel remains confined multiplied by the fuel's particle density must be sufficiently high that the heating from alpha particles produced by the reaction out runs the energy losses. This is the Lawson criterion and is $n\tau_c = 2 \times 10^{15}$ for $20keV$ plasmas.

At today's forefront of inertial confinement research is the National Ignition Facility (NIF) at LLNL. At NIF, one hundred and ninety-two laser beams will deliver more than a megajoule of light in only a few nanoseconds to drive the compression of a millimeter sized, spherical capsule of frozen deuterium and tritium to the high density of hundreds of grams per cubic centimeter. It is expected that NIF will be able to demonstrate a high gain fusion burn. NIF in its first phase will use the method of indirect drive with hotspot ignition. Later on it will be reconfigured to run direct drive implosions, and with upgrades may even be able to demonstrate fast ignition.

1.2.1 DIRECT DRIVE VERSUS INDIRECT DRIVE

All implosion in ICF operate on a rocket principle whereby the outer shell of the capsule is heated and then ablates off in a radial direction. Momentum conservation means the inner layers of the capsule are forced towards the core. The crucial difference between direct drive and indirect drive is whether or not the energy delivery to the capsule is by direct irradiation from the lasers or indirectly from x-rays produced by the inner walls of a gold cavity called a hohlraum. Hohlraum is a German word which translated to English means cavity. The ICF capsule sits inside the cavity which provides a uniform x-ray field characterized by the blackbody radiation temperature. This is usually on the order of $300eV$ [1].

Hotspot ignition has very stringent conditions on the uniformity of the implosion which is talked about in further detail below. Attempting to maintain a uniform radiation field by focusing 192 laser onto a small target from all sides is difficult. In addition to having good pointing stability of the lasers, each beam must also have a smooth profile at the focus with none of the usual hot-spots found in a laser beam.

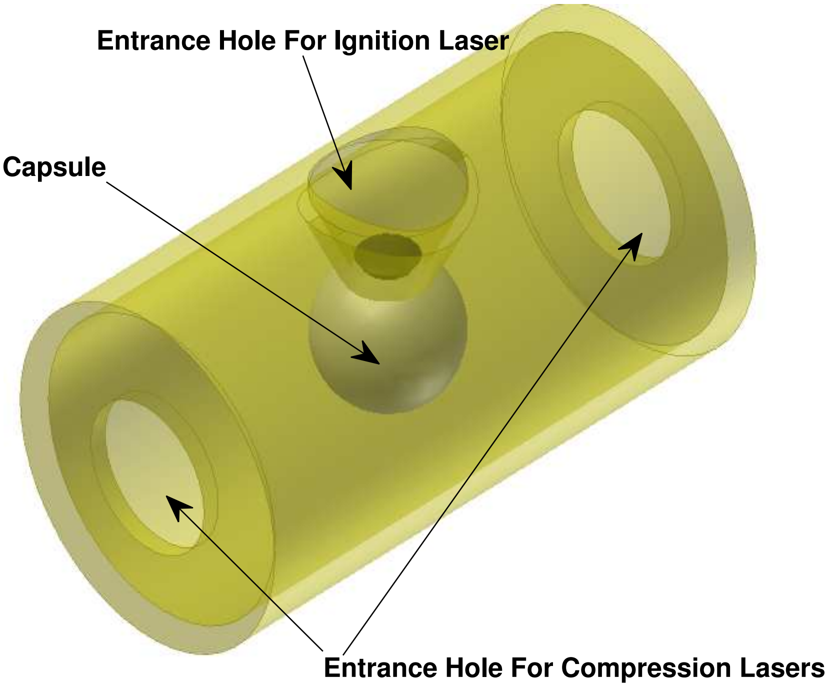

Figure 1.1: An illustration of a gold hohlraum configured for the indirect drive implosion of a capsule with a proton driven fast igntion.

1.2.2 CONFINEMENT TIME AND BURN FRACTION

The most favorable reaction for a fusion burn is by far the combination of deuterium and tritium. The cross-section for this reaction is nearly an order of magnitude more than other nuclear reactions. The reaction products as wells as their kinetic energy are,

$$D + T \rightarrow \alpha[3.5MeV] + n[14.1MeV]. \tag{1.1}$$

The net $17.6MeV$ of energy released per reaction means a total energy release of $3.3 \times 10^{11} J$ for every gram of DT fuel that is burned.

The following subsection follows the summery of gain calculations in papers by J. Lindl [1] and M. Rosen [3]. The trick to high gain fusion is to get a much of a mass of fuel to burn as possible while supplying the least amount of energy to initiate the burn. In ICF, the time in which the fuel is said to be confined can be thought of as the time it takes for points in the imploded capsule to become aware of the vacuum they are expanding towards. Consider a point that is a distance r' away from the center of the fuel. If the compressed capsule has a radius R, then it will take a time $\tau = (R - r')/c_s$ to sense the vacuum. Here, c_s is the usual sound speed of a plasma. We can define the total confinement time as the average time for each point within the volume.

$$\tau_c = \frac{1}{(4/3)\pi R^3}\left(4\pi \int_0^\infty \frac{R - r'}{c_s} r'^2 dr'\right) = \frac{R}{4c_s} \tag{1.2}$$

This is thought of as the time it takes for the fuel to become sufficiently disassembled so that the fusion produced alpha particles no longer heat the plasma and the burn stops.

An estimation of the total fraction of fuel that will be consumed can be estimated by integrating the rate equation over the confinement time. If one considers a fuel which has a 50/50 ratio of deuterium and tritium and call one element of fuel as being a DT pair, then the number density of fuel elements is $n = 2n_D = 2n_T$. The rate of burn is

$$\frac{dn}{dt} = -\frac{n^2}{2}\langle\sigma v\rangle_{DT}, \tag{1.3}$$

where $\langle\sigma v\rangle_{DT}$ is the reactivity of the fuel as the number of reactions per unit volume per unit time averaged over a Maxwellian distribution. Taking the limits of integration to be at $t = 0 \rightarrow n = n_0$ and $t = \tau_c \rightarrow n = n_f$, one gets,

$$\frac{1}{n_f} - \frac{1}{n_0} = \frac{\tau_c}{2}\langle\sigma v\rangle_{DT}. \tag{1.4}$$

Taking the burn fraction to be $f_b = 1 - n_f/n_0$ and substituting the confinement time with the definition above equation becomes

$$f_b = \frac{\rho R}{\rho R + 8m_{DT}c_s/\langle\sigma v\rangle_{DT}}, \tag{1.5}$$

where ρ is the initial fuel number density times the mass of DT (2.5amu), $n_0 m_{DT}$. So the burn fraction depends on the temperature according to the dependence in $8m_{DT}c_s/\langle\sigma v\rangle_{DT}$ and the quantity ρR.

For ignition relevant temperatures around $30keV$, $8m_{DT}c_s/\langle\sigma v\rangle_{DT} = 6g/cm^2$ So to achieve a decent burn fraction of 33%, one needs a ρR of about $3g/cm^2$. With atmospheric densities of hydrogen being around $9 \times 10^{-5} g/cc$, DT capsule with a diameter of just over half a kilometer would be sufficient to satisfy this areal density. If such a sample were heated to an ignition temperature of about three hundred million degrees kelvin then about $1.4 \times 10^{21} J$ of energy would be catastrophically released. This would amount to a three hundred thousand kiloton bomb!

Actual ICF capsules will be compressed to a density of more than $400g/cc$. The corresponding radius for a $\rho R = 3g/cm^2$ is $75\mu m$. In contrast with the super massive bomb mentioned above, the yield of this explosion will be about 17 millitons. This is about the same energy approximately 32 typical fast food cheeseburgers.

1.2.3 HOTSPOT VERSUS FAST IGNITION

Attempting to heat an entire volume of DT to the temperature needed for ignition is a very inefficient way achieve fusion. Instead, two schemes exist where only about 1% of the total fuel mass is heated. The first method, hotspot ignition, is the one which will be demonstrated by NIF in 2009 when the facility goes online. In hotspot ignition, the capsule is prepared so that a dense shell of "cold" fuel surrounds a low density core. During the compression, which is optimized to heat the target as little a possible, the low density core is preserved. Under equilibrium conditions, the entire compressed capsule is said to be isobaric. Given the ideal gas law relationship that the pressure is proportional to the product of the density and the temperature, then regions in the capsule that are dense will be cold relative to the 1% of the capsule that is not dense. The not dense core will be hot to maintain the proportionality. Heating only this small fraction of the fuel means an automatic factor of 100 improvement in the gain relative to heating the entire volume.

If hotspot ignition were made analogous to a diesel engine where the compression of the fuel raises the temperature until it combusts, then fast ignition would be a spark-plug driven engine. Fast ignition, first proposed by M. Tabak [4], involves compressing the capsule to a constant density and then delivering an ultra-intense laser heating beam to the edge of the compressed fuel. An isochoric compressed fuel has substantial benefits over the isobaric fuels of hotspot ignition. The initial fabrication of the capsule allows for more flaws in the symmetry and has lower demands on the driver energy compressing the fuel. The implications are cheaper manufacturing costs of

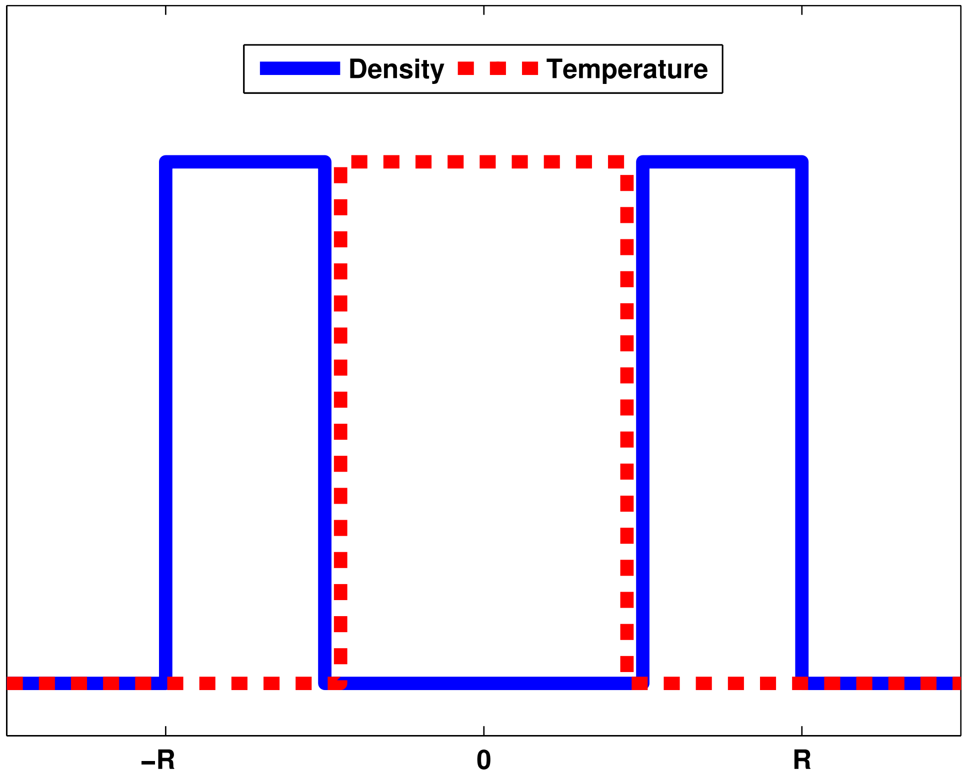

Figure 1.2: An illustration of the density and temperature profiles in an isobaric compressed fuel for hotspot ignition. Where the density is low, the temperature must be high to maintain the constant pressure.

targets and higher energy gains per shot target. With fast ignition, ICF has an increased feasibility as a concept for a fusion burning power plant.

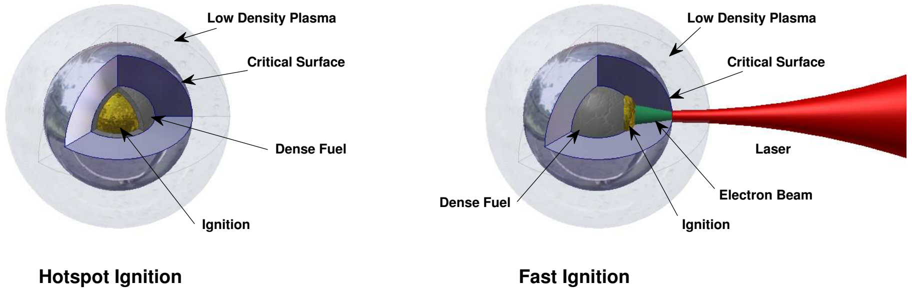

(a) Hotspot Ignition

(b) Fast Ignition

Figure 1.3: On the left, a representation of hotspot ignition where an isobaric fuel forms a natural hot spot in the low density core. On the right, in fast ignition, an isochoric fuel that is ignited on an edge by a short-pulse laser.

The primary reason for the high cost and strict fabrication requirements of hotspot ignition is that hydrodynamic instabilities will destroy the low density bubble before ignition can occur. Among the more famous of these is the Rayleigh-Taylor instability. Any time a dense fluid sits on top of a less dense fluid with a downward acceleration (such as a glass of water that has been inverted), then a small perturbation of the surface at the density boundary will grow at a rapid rate (i.e. the water in the glass will spill out onto the floor). The rate of growth is given by

$$\gamma = \sqrt{\frac{gkA}{1+kL}} - \beta k v_{abl}, \tag{1.6}$$

where L is the characteristic length over which the high density region becomes the low density region, g is the effective acceleration experienced by the fluid during compression, k is the wave number for oscillations at the density boundary, v_{abl} is the velocity of the ablated surface driving the compression, and $A \equiv (\rho_{above} - \rho_{below})/(\rho_{above} + \rho_{below})$ is the Atwood number. So to keep this rate small, one can either minimize the Atwood number or increase the driver energy thereby increasing the ablation velocity.

The technical challenge with fast ignition is the energy transport from the ultra-intense laser to the dense fuel. As a necessary byproduct of the implosion, the DT fuel is surrounded by a cloud of plasma with millimeter scale-lengths. A short-pulse laser incident on this plasma will meet the point known as the critical surface before it reaches the region it must heat. The critical surface is the point where the plasma density is so high that the plasma frequency is equal to the laser frequency. Here the plasma oscillations constructively interfere with the laser propagating in the forward direction and acts like a perfect mirror; sending the laser light away. For a laser wavelength of λ, the critical density n_c solves

$$\omega_p = \sqrt{\frac{n_c e^2}{m_e \varepsilon_0}} = \frac{2\pi c}{\lambda}. \tag{1.7}$$

For $\lambda = 1\mu m$, this corresponds to $n_c = 1 \times 10^{21} cm^{-3}$.

1.3 METHOD OF FAST IGNITION

The get past the critical surface, it is necessary to convert the laser energy to some other form which can overcome transport issues in the over-dense plasma. Two possibilities are relativistic electrons or MeV protons. Each has its own physics challenges and barriers that must be overcome in both simulation and experiment.

1.3.1 ELECTRON FAST IGNITION

In M. Tabak's proposal, energy transport beyond the critical surface will not be laser light, but rather suprathermal electrons accelerated by the laser near the critically dense plasma travel in the propagating direction of the beam. The very strong, self-consistent electric and magnetic fields of the relativistic electron beam are supposed to aid the transport. Simulations show that as the over-dense plasma heats up, the corresponding drop in resistivity results in a the electrons self-collimating. Thus, the energy of the $< 20ps$ burst of relativistic electrons can deposit in a spot with a diameter less than $30\mu m$.

This has not been observed experimentally however. Experiments on cold target have been preformed to measure the beam divergence [5, and references therein]. Imaging the K_α x-rays emission of buried layers placed at known depths within the target was a direct measurement of the position of the hot electrons which cause the K-shell ionization of the layers. For laser intensities greater than $10^{19} W/cm^2$, the full angle of the divergence is greater than 30° and increases proportionately with the intensity. It should be noted that with a cold target, the resistivity of the material increases as it heats. In a hot plasma, the material is in the Spizter regime where the resistivity would fall off $\propto T^{-3/2}$ [6].

1.3.2 PROTON FAST IGNITION

Proton acceleration from thin foils irradiated by ultra-intense lasers has been well studied in the past decade [7, 8, 9, 10, 11, 12]. The dominant mechanism for proton acceleration is the described by the Target Normal Sheath Acceleration (TNSA) model [13, 14]. Conversion efficiency from laser to protons has been observed as high as a few percent. An exciting feature of this mechanism is that ions are accelerated orthogonally to the target surface. So by curving a thin foil into a spherical shape, one can focus the beam. Proton focusing and isochoric heating from proton beams has been demonstrated [15].

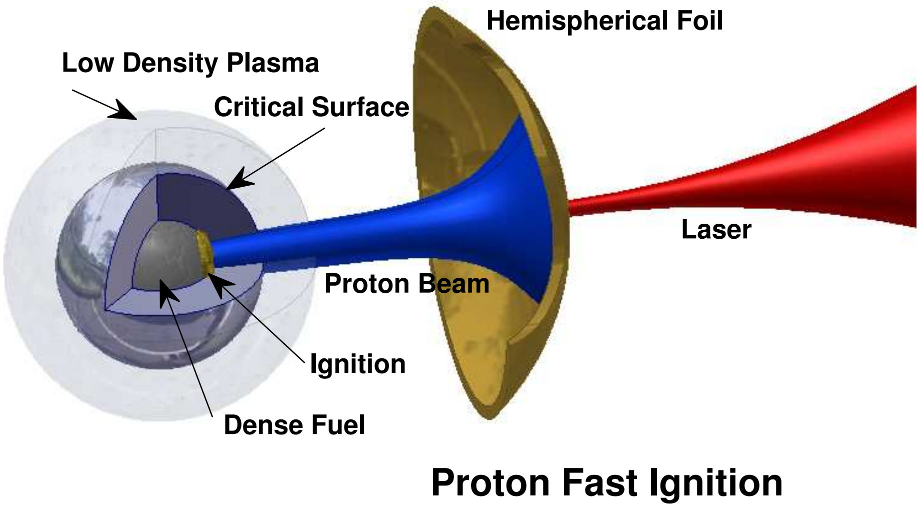

Figure 1.4: Representation of proton fast ignition where a focused proton beam from a hemispherical foil heats an isochoric fuel.

Protons were proposed by M. Roth *et al* [16] as an alternative to electrons for use in fast ignition. Detailed calculations of the energy requirements of a laser accelerated proton beam as an igniter for fast ignition were made by S. Atzeni *et al* [17]. Typical proton beams have a Boltzmann like energy distribution, $dN/d\mathcal{E} \propto \exp(-\mathcal{E}/kT_p)$. As they travel from their source to the dense fuel, the proton beam's peak power will be decreased by the velocity dispersion. The power of the proton beam is,

$$P(t) = 2\frac{\mathcal{E}_{total}}{\tau}\left(\frac{\tau}{t}\right)^5 \exp\left(\frac{-\tau^2}{t^2}\right), \tag{1.8}$$

where the pulse duration is,

$$\tau = \left(\frac{m_p d^2}{2kT_p}\right)^{1/2}. \tag{1.9}$$

Here, m_p is the mass of a proton and d is the distance traveled by the beam since the source. In simulations, a proton temperature of about $3MeV$ to $5MeV$ was found to minimize the proton beam energy requirements. The minimum is due to the velocity dispersion and the optimal proton stopping range in the plasma. The proton beam energy needed for ignition in a $30\mu m$ diameter spot is,

$$\mathcal{E}_{ig}^*[kJ] \approx 90d[mm]^{0.7}/\rho[100g/cc]^{1.3}. \tag{1.10}$$

For a fuel density of about $400g/cc$ the ignition energy is about $15kJ$ if the spherical foil is placed $1mm$ back. The expected available laser energy will be about $100kJ$, which means a conversion efficiency of 15% is needed. That is 2 to 5 times what has been demonstrated in experiment.

It is the goal of this thesis work to explore the possible use of heavy hydrides to improve the conversion efficiency from laser to protons. For protons to be a viable igniter, the target of 15% with an average temperature of about $5MeV$ $MUST$ be demonstrated.

CHAPTER 2

THEORY OF ION ACCELERATION

The observation of protons accelerated from thin foils irradiated by intense, short-pulse lasers ($>10^{18} W/cm^2$) has been an interesting area of study for many years. The highly energetic and directed beams of ions observed have potential applications in imaging, medicine, and isochoric heating in fast ignition. Medical application include the possibility of cancer treatment. Highly energetic protons can travel deep into human tissue and can target tumors. Laser accelerated protons are beam like in nature, and deposit most of their kinetic energy near an energy dependant depth called the Bragg peak. As such, the tumor can be targeted to minimize the collateral damage of the surrounding healthy tissues. Laser accelerated protons are also a useful backlighter in imaging experiments. The protons are short in pulse duration ($\approx 5ps$) and originate from a point like source. Because they are charged particle they have been used to image magnetic field strengths in ICF implosion experiments by measuring the proton deflection [18]. This chapter discusses the isothermal 1-D expansion of a plasma into a vacuum and the Target Normal Sheath Acceleration (TNSA) models; following closely the derivations done by Mora [19] and Wilks *et al* [13]. Next, the affect of ion mass and charge on the fraction of energy partitioned into protons observed in LSP simulations and computed analytically (Foord *et al*) [20] is covered. Simulations using LSP that model the conditions of the experiment performed using the Callisto laser are also presented. Lastly, the possible affect ionization may have on the overall benefit of erbium hydride over plastic targets for energy scales relevant for fast ignition is discussed.

2.1 TARGET NORMAL SHEATH ACCELERATION

Ions accelerated by laser irradiated foils come from both the front and back surfaces of the foil [10]. Ions and electrons are accelerated directly by the laser E and B fields at the front surface by the pondermotive potential. The strong electric fields of the ultra-intense laser 'wiggle' the charged particles in a direction orthogonal to the propagation direction of the laser. The resulting currents are high enough in magnitude to make the $q\vec{v} \times \vec{B}$ force significant. So in addition to a velocity component orthogonal to the laser propagation, there is also a component in the laser direction. Other mechanisms exist that are responsible accelerating particles, however pondermotive scaling has shown good agreement with experiments at intensities around $10^{19} W/cm^2$ [13]. Mostly electrons are accelerated in this manner, but some protons will also be give a velocity in the same direction. Protons accelerated by this mechanism contribute about 1% of the total observed proton beam with kinetic energies greater than $3MeV$ per nucleon at the rear surface [7].

The energy spectrum of the electrons is approximately Boltzmann like and for simplicity, is assumed to fit a a one temperature Boltzmann distribution. The average kinetic energy per electron is give by

$$kT_e \cong mc^2 \left(1 + \frac{2U_p}{mc^2}\right)^{1/2}, \tag{2.1}$$

where $U_p[eV] = 9.33 \times 10^{-14} I[W/cm^2]\lambda[\mu m^2]$ [13] is the pondermotive potential. These hot electrons travel through the target and will travel a distance beyond the foil surface before being stopped by the strong, positive charge left behind. Some of the electrons will escape into the vacuum while others will *reflux* [21] through the target, oscillating several times.

The following rigorous deviation for a 1-D expansion from a semi-infinite slab by P. Mora [19] describes how the laser accelerated electrons create a strong pressure at the vacuum boundary. As the charge separation between the hot electrons and the ion front near the target surface evolves, the ions are pulled away from the target and into the vacuum. Two observations in proton experiments that this model captures are the typical ion distribution, $dN/d\mathcal{E}$, and the sharp cutoff in the spectrum at some maximum kinetic energy, $\mathcal{E}_{max}$.

The setup of the derivation assumes the electrons are initially distributed within a semi-infinite slab for $x \leq 0$. The space at $x > 0$ is vacuum. The energy spectrum in the slab is $n_e = n_{e0} \exp(e\Phi/kT_e)$. The ions are assumed to be at rest. The electrostatic potential Φ satisfies the Poisson equation by,

$$\bigtriangledown^2 \Phi = \frac{e}{\epsilon_0}(n_e - Zn_i). \tag{2.2}$$

Here, Z and n_i are the charge number and ion density respectively. Integrating from $x = 0$ to $x = \infty$ one finds that the initial electric field is $E_{front,0} = \sqrt{2/\exp(1)}E_0$, with $E_0 = (n_{e0}kT_e/\epsilon_0)^{1/2}$.

The ion density and velocity distributions must satisfy the continuity equation and the ion equation of motion,

$$\left(\frac{\partial}{\partial t} + v_i \frac{\partial}{\partial x}\right) n_i = -n_i \frac{\partial v_i}{\partial x}, \qquad \left(\frac{\partial}{\partial t} + v_i \frac{\partial}{\partial x}\right) v_i = -\frac{Ze}{m_i}\frac{\partial \Phi}{\partial x}. \tag{2.3}$$

Assuming quasi charge neutrality ($n_e = Zn_i$) and a space time dependence of the form x/t, the self-similar solution to the above equations is,

$$n_e = Zn_i = n_{e0}e^{-(1+x/c_st)}, \qquad v_i = c_s + x/t, \tag{2.4}$$

where $c_s = (ZkT_e/m_i)^{1/2}$ is the ion sound speed. The local plasma scale length is given by c_st. Solving the above equations in terms of $\mathcal{E} = (1/2)m_iv_i^2$ and differentiating by $\mathcal{E}$ an ion slope-temperature is predicted as,

$$\frac{dN_i}{d\mathcal{E}} = \frac{n_{i0}c_stA}{\sqrt{2ZkT_e\mathcal{E}}} \exp\left(-\sqrt{\frac{2\mathcal{E}}{ZkT_e}}\right). \tag{2.5}$$

The area A is the effective area of the proton source size.

The self-similar solution is only valid if the initial Debye length, $\lambda_{D0} = (\epsilon_0kT_e/n_{e0}e^2)^{1/2}$, is less than the plasma scale length, or equivalently the evolution time must be greater one over the ion plasma frequency, ($\omega_{pi}t > 1$). The plasma frequency is give by $\omega_{pi} = (n_{e0}Ze^2/m_i\epsilon_0)^{1/2}$. The position of the ion front can be estimated by assuming the local Debye length, $\lambda_D = \lambda_{D0}(n_{e0}/n_e)^{1/2}$, is equal to the plasma scale length,

$$\lambda_D = \lambda_{D0}\exp[(1 + x/c_s)/2] = c_st. \tag{2.6}$$

This gives that the ion velocity at the front is given by $v_{i,front} \approx 2c_s\ln(\omega_{pi})$. The corresponding electric field at the front can be found using Newton's second law, $m_idv_{i,front}/dt = ZeE_{front}$. The resulting electric field is $E_{front} \approx 2E_0/\omega_{pi}t$.

A more accurate expression for the electric field strength at the ion front was numerically solved by Mora. The corresponding velocity is,

$$v_{i,front} \cong 2c_s \ln \left(\frac{\omega_{pi}t}{\sqrt{2\exp}} + \sqrt{\left(\frac{\omega_{pi}t}{\sqrt{2\exp}}\right)^2 + 1} \right). \tag{2.7}$$

In the limit that $\omega_{pi}t \gg 1$ the velocity is approximately $2c_s \ln(\omega_{pi}t/\sqrt{2\exp})$. Thus, the maximum ion energy is,

$$\mathcal{E}_{max} \cong 2ZkT_e \left[\ln(\sqrt{2}\omega_{pi}t) - 1/2\right]^2. \tag{2.8}$$

One obvious problem with the isothermal model as derived above that has been pointed out [22, 23] is the total amount of energy into the ions is infinite if the time goes to infinity. The electrons essentially have an infinite reservoir in the in the semi-infinite expanse at $x \leq 0$. Also, the model does not include collisional and radiative losses in the electron energy.

We can write the total ion beam energy by solving $\int(dN_i/d\mathcal{E})\mathcal{E}d\mathcal{E}$ for the entire energy range $0 \leq \mathcal{E} \leq \mathcal{E}_{max}$. Using the distribution described by equation 2.5,

$$\mathcal{E}_{total} = n_{e0}kT_e c_s t A \frac{1}{2} \int_0^{x_m} x^2 e^{-x} dx, \tag{2.9}$$

where $x_m = \sqrt{2\mathcal{E}_{max}/ZkT_e}$. Typically the cutoff energy is much greater than the hot electron temperature and so the quadrature factor above is approximately 2. Thus, the total ion energy is approximately $n_{e0}kT_e c_s t A$.

Additional work by Mora [24] treats the case of a thin foil with finite thickness $L \gg \lambda_D$. Now the total electron energy in the slab is $n_{e0}kT_e LA$. This also gives an absolute upper bound on the time over which the ions can accelerate as $t_{max} = L/2c_s$. At this time, each half of the target has rarefacted in both directions. However, it is noted that the actual acceleration time is significantly less than this. The above time would assume the electron temperature remains constant. In fact, the electrons cool rapidly as the plasma expands, meaning $t \ll t_{max}$.

We can write a conversion efficiency for protons from electrons as the ratio of the two expressions above, $\eta_{e\rightarrow p} = (n_{e0}kT_e c_s tA)/(n_{e0}kT_e LA)$. Using the time as t_{max} the the greatest this conversion efficiency can be is $\eta_{e\rightarrow p} = 50\%$. With typical experimentally observed conversion efficiencies from laser to hot electrons of about 30% [9], the upper limit of laser to proton conversion efficiencies would be 15%.

2.2 INFLUENCE OF HYDRIDES

The ions typically observed in experiments owe their origins to naturally occurring hydrocarbon contaminant layers present on foil surfaces [8]. The thickness of such layers are on the order of a couple of nanometers and have a density similar to that of gasoline [7]. Estimations of the hydrogen abundance suggests that experiments demonstrating laser to proton conversion efficiencies of 2% with $150J$ lasers [25] may be on the verge of depleting the contaminant layer. To counter this limit, hydrogen rich coatings have been suggested.

The benefit of using hydride coatings is two fold. The first is to address the problem of depletion as mentioned above. The second is that the way in which the ion beam energy partitions into the different ion species can be controlled to the advantage of the protons. The mechanism for this is outlined below and is the motivating concept of my thesis.

2.2.1 BACKGROUND WORK

A series of simulations were done by M. Foord, *et al* [26, 20] using the hybrid pic code, LSP (Large-Scale Plasma) [27, 28] to investigate the conversion efficiency from hot electrons to ions for a variety of surface compositions. LSP is numerical code which combines the treatment of fast moving, charged particles with collisional fluid dynamics by implementing both pic calculations and hydrodynamic fluid equation solvers.

Traditional pic (particle in a cell) codes simulate the dynamics and kinematics of large numbers of interacting charged particles by partitioning space into cells. Rather than calculating the interaction forces on each particle, due to all of the other particles individually, only the particles within that particle's cell are computed directly. The interactions of particles outside the cell are treated as the average fields due to the particles within that cell. This greatly reduces the number of calculations needed to simulated the transport of energetic particles though a plasma. Hydrodynamic codes on the other hand treat the plasma as a fluid and consist of iterative numeric solvers of the fluid equations.

The LSP simulations by M. Foord varied the surface layer as different binary mixtures. The injected hot electron distribution and the substrate foil's material and thickness were kept constant. The simulations used a $5\mu m$ gold substrate injected with $2 \times 10^{19} cm^{-3}$ electrons having a temperature of $kT_e = 300keV$ and a forward drift energy of $300keV$. The pulse length was $100fs$. The surface layers used ranged from pure hydrogen to XH_n where X represents atoms of various atomic mass ranging from the light weight of lithium to the more massive, uranium. All of the simulations were in 1-D. The conversion efficiency of the ions and protons from hot electrons are shown in figure 2.1.

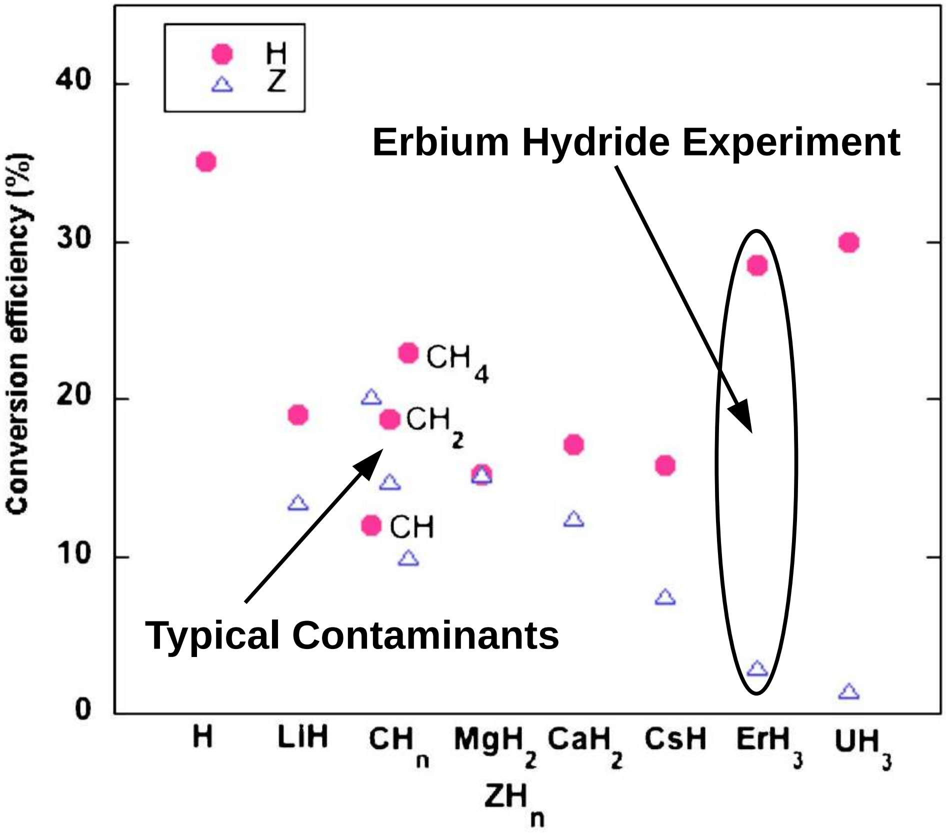

Figure 2.1: Results from LSP simulations showing the dependance of hydride mass on the conversion efficiency to proton. Simulations and figure were produced by Mark Foord, *et al* [20]

One thing LSP lacks is an equation of state for ionization. So an additional assumption of the charge of each ion had to be made. In each case, the maximally ionized state allowed according to field ionization by barrier suppression (FIBS) corresponding to the electric field $\sqrt{n_e kT_e/\epsilon_0}$ was used. Ionization is discussed in greater detail in section 2.3. To further investigate the importance of the charge state of each ion, simulations of $C^{+i}H^+$ were computed for all of the six possible charge states of carbon.

If we assume that the total acceleration time for each ion species is the same and that each experiences the same electric field then the velocity of each ion must satisfy Newton's second law by $m_i(d\vec{v}_i/dt) = Ze\vec{E}$. Taking the electric field to be approximately time independent and noting that the ions are non-relativistic, the total energy to a particular ion species is proportional to Z^2/m_i. Thus, the fraction of energy that is partitioned to the protons is $f_p = (Z_p^2/m_p)/(\sum Z_i^2/m_i)$.

Using this relationship, a semi-empirical fit of the simulated data from LSP gave a weaker scaling on the charge state. In reality, the electric field is time varying in the expanding plasma. The fit found by M. Foord for the fraction of energy into the protons is,

$$f_p = \left(1 + \frac{Z^{1.7}}{MN}\right)^{-1}, \tag{2.10}$$

where M is the mass of the hydride atom divided by the mass of hydrogen and N is the ratio of hydrogen atoms per hydride atom. The total proton beam energy is $f_p\mathcal{E}_{tot} \approx f_p n_{e0} kT_e c_s t A$. Because of the mixture of ion species the sound speed is taken to be an average over the ion concentrations $c_s = (kT_e\langle Z_i^2/m_i\rangle/\langle Z_i\rangle)^{1/2}$ [29].

This result suggests that the conversion efficiency to protons can be improved by using a heavy hydride such as uranium or erbium. The large mass of these atoms means a greater fraction of the energy is parted into the protons. The LSP data even suggests that the proton conversion efficiency approaches the case of a pure hydrogen surface.

2.2.2 SIMULATIONS FOR THIS WORK

Further simulations were performed using LSP to model the experimental data collected from my thesis work. In the experiments an ErH_3 coating was compared with naturally occurring hydrocarbon contaminants on $5\mu m$ gold foils. For these two cases the erbium hydride was assumed to be a pure coating with a density of $7.6g/cc$ and the contaminants were give the composition measured using x-ray photo-emission spectroscopy with an assumed density of $1g/cc$. Details of the contaminant composition and target specifications are given in chapter 4. Like the previous work, all the simulations were in 1-D.

The electron distribution inputed was chosen so that the proton spectrum from the simulation matched that of the experimental data. The best fit seen in figure 2.2 was found using a hot electron temperature of $160keV$, a pulse length of $200fs$, and forward drift velocity characterized by $\gamma\beta = 1$. The variables γ and β have the usual definition from special relativity. After $1.6ps$ the addition of new energy to the ions became insignificant. The total energy to each ion species versus time is shown in figure 2.3.

As chapter 4 will show, the charge state of the carbon was almost entirely C^{+4}. What was unknown, however, was the ratio of hydrogen to the carbon and oxygen observed in the x-ray photo-emission measurement. Hydrogen was not directly detectable, and must be inferred from the abundance of carbon and oxygen. Three cases were simulated for the contaminant layer case. The first was that the carbon ions were all C^{+4} and the oxygen were all O^{+5} with the ratio of hydrogen to carbon and hydrogen to oxygen were both 2:1. The second used the same ions but with the

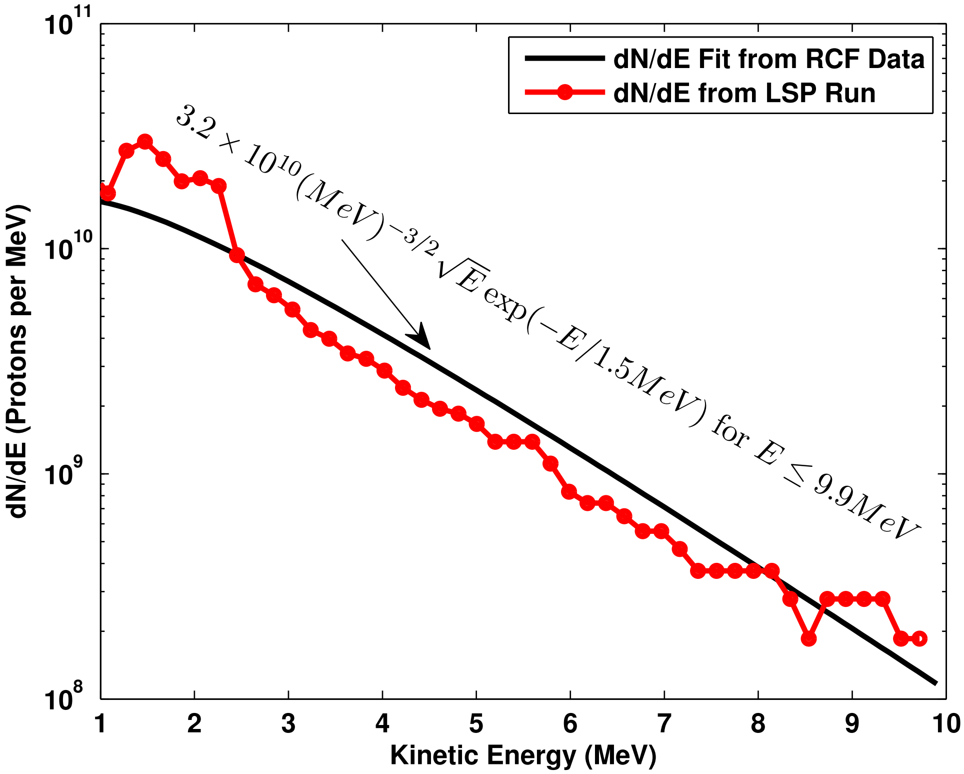

Figure 2.2: A simulated proton spectrum compared with the spectrum derived from experimental results. The electron distribution used in the simulation was chosen to optimize this fit. The amplitude of the simulated spectrum is arbitrary since it was run in 1-D, thus was scaled to match the spectrum from experiment

ratio reduced to 1:1. A third simulation was also done repeating the 2:1 ratio but with each atom fully ionized.

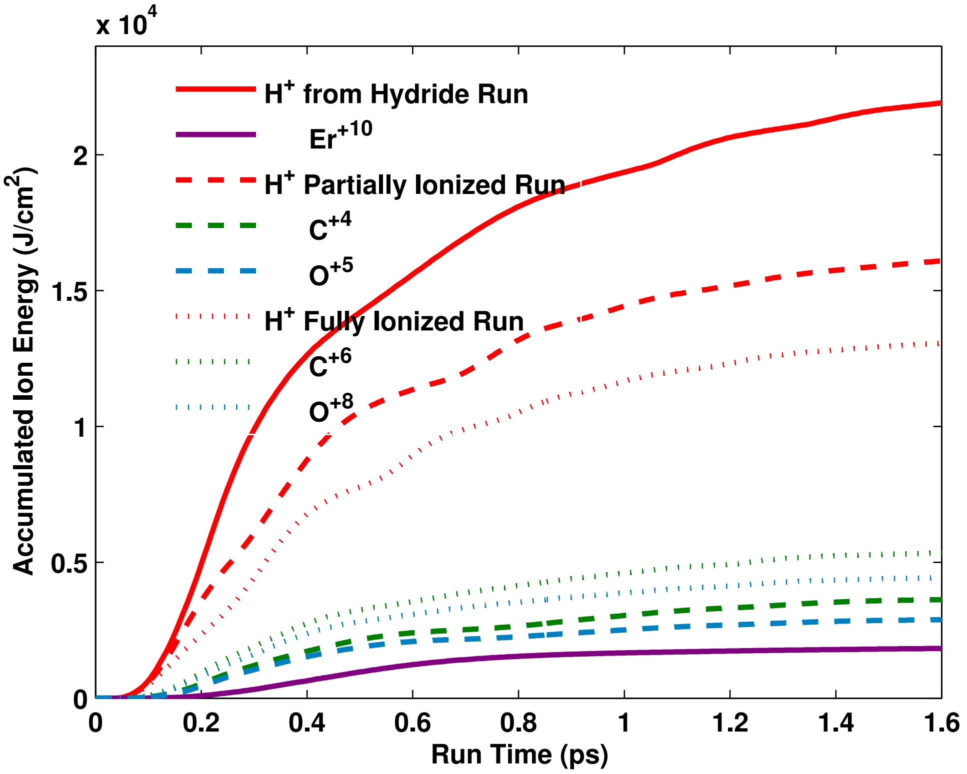

Figure 2.3: LSP results showing the integrated beam energy of each ion species for three separate simulations. The solid lines are from ErH_3. The dashed lines are the three dominant ion species H, C, and O for a partially ionized contaminant layer. The dotted lines are also from contaminants but assume all atoms are fully ionized.

Also unknown and not measured was the ionization state of erbium. Bounds for the possible charge state were inferred from the measured ionization of carbon and gold in the experiments (See chapter 4). Electric fields sufficient to ionize carbon to C^{+4} correspond to Er^{+4}. To ionize up to C^{+5}, would produce Er^{+25}. The actual limit was less than this. Also, it is most likely that the erbium charge state would be distributed over a range of values from Er^{+1} to Er^{+max}. As one last constraint, the proton distributions measured from both experiments was considered. According to the isothermal model the protons and electrons will have approximately equal temperatures. From the Callisto data set, a typical proton temperature fit to a Maxwellian distribution was about $1.7MeV$. With the usual assumption of a 30% conversion efficiency from the $8J$ laser to hot electrons [9], a target thickness of $5\mu m$, and an estimated effective cross-sectional area of the electron beam being $\pi(100\mu m)^2$ [30] the hot electron density would be about $5 \times 10^{19} cm^{-3}$. The corresponding sheath field can ionize up to Er^{+10}. On the Titan laser the energy is $150J$ and the proton temperature around $3MeV$. The electric field is, therefore $\sqrt{10}$ times that of the Callisto data. The upper bound on the erbium in this case would be Er^{+22}. To sample this charge range, three simulations executed different possible values of the erbium charge. These were Er^{+5}, Er^{+10}, and Er^{+15}.

Rear Surface Layer	**Conversion Efficiency**
Pure Erbium Hydride on Gold	
$Er^{+5}H_3^+$	29%
$Er^{+10}H_3^+$	26%
$Er^{+15}H_3^+$	21%
Contaminant Layer (Table 4.1) on Gold	
$C^{+4}H_2^+$ and $O^{+5}H_2^+$	19%
$C^{+6}H_2^+$ and $O^{+8}H_2^+$	15%
$C^{+4}H^+$ and $O^{+5}H^+$	13%

Table 2.1: LSP results for the proton conversion efficiency from electrons from the six simulations executed for this work using $5\mu m$ gold targets. Conversion efficiency is defined as the total proton beam energy counting only protons with a kinetic energy greater than $3MeV$ divided by the total energy of the injected electron pulse.

Table 2.1 shows the conversion efficiency from hot electrons in the six LSP simulations conducted. The pure erbium hydride simulations were of $200nm$ thick coatings on $5\mu m$ gold substrate. The density of the hydride was taken as $7.6g/cc$. As for the contaminant layer simulations the coatings had a density of $1g/cc$ and included the complete atomic composition described by table 4.1 in chapter 4. The thickness of the contaminant layer was also taken to be $200nm$. This was done so that larger zone sizes could be used to allow the simulation a reasonable run time. The actual thickness of the contaminant layer was closer to $1nm$ thick. The difference of using a thicker layer in the simulation is insignificant because the ions at the outermost surface have little or no knowledge of the ions deeper in the layer. The comparison only breaks down in instances where the contaminant layer was fully accelerated in the experiment. This was not likely the case in the Callisto experiment, which will be presented in chapter 4.

2.3 DISCUSSION OF IONIZATION

With the fraction of ion energy partitioned to the protons depending on Z to the power of 1.7, it was interesting to estimate the ionization rates of each ion species for increasing sheath field strengths. The experiments conducted for this work where at laser energies between $10J$ and $150J$. At full scale fast ignition, the laser energy will be closer to $100kJ$. Because erbium has more electrons to give up than carbon, the natural question to ask is at what point does the benefit of ErH_3 over CH_2 cease.

Here ionization of the surface layer due to three mechanisms and how this affects the partitioning of energy as the laser energy is increased is considered. The first and most dominant is Filed Ionization by Barrier Suppression (FIBS) [31]. The electric field due to the sheath is on the order of teravolts per meter. This is comparable the strength of the field due to the atomic nucleus itself. This means that the Coulomb potential is summed with the linear potential of the sheath field. This causes the potential to tilt, creating three distinct regions; the bound electrons within the Coulomb dominated region, a classically forbidden region, and a region where the potential has been pushed to strengths less than that of the trapped electrons. The trapped electrons can quantum tunnel through the classically forbidden region and into the continuum. The rate with which this occurs can be calculated using the standard ADK model [32].

$$\nu_{ADK}[s^{-1}] \approx \frac{6.6 \cdot 10^{16} Z^2}{n_{ef}^{4.5}} \left(\frac{10.87 Z^3 E_{at}}{n_{ef}^4 E} \right)^{2n_{ef}-1.5} \exp\left[\left(-\frac{2Z^3 E_{at}}{3n_{ef}^3 E} \right) \right], \tag{2.11}$$

where $E_{at} = 0.51TV/m$ is the atomic electric field strength and $n_{ef} = Z/\sqrt{U_H/U_Z}$. The ionization potentials U_H and U_Z are for hydrogen $(13.6eV)$ and the ion in question respectively. Values for the ionization potentials available in appendix B. The minimum electric field strength according to FIBS for a given Z is,

$$E_Z^{min} = U_Z^2 \epsilon_0 \pi / eZ. \tag{2.12}$$

A second mechanism for ionization is due to collisions from the relativistic, hot electrons [31]. For collisional ionization the rate is estimated [33, 31] as,

$$\nu_{col} \approx n_e v_e 4\pi a_b^2 \frac{U_H^2}{U_Z kT_e} \ln\left(\frac{kT_e}{U_Z} \right), \tag{2.13}$$

where v_e is the average electron velocity and a_b is the Bohr radius.

The third mechanism is collisions from the cold return current of electrons. To maintain current neutrality, the rate of cold electrons returning must equal the rate exiting through a surface; $v_e n_e = v_e^{ret} n_e^{ret}$. The ionization rate is the same equation used for the hot electron collisions but using the cold electron velocity and density.

To compute the average ionization state of each atom, it is assumed that the time spent in the electric field is the same for each ion. The total ionization rate for a particular ion charge state is the sum of the three contributing equations $\nu_{total,Z} = \nu_{ADK} + \nu_{col}^{hot} + \nu_{col}^{cold}$. The probability of producing ion, Z, is the total rate for one ion species divided by the some total of the rate of all ion species. The average charge is

$$Z_{avg} = \left(\sum_Z Z v_{total,Z} \right) \left(\sum_Z v_{total,Z} \right)^{-1} \tag{2.14}$$

As an upper bound on the the ion charge the case that each atom is fully ionized up to the maximum level allowed according to FIBS (equation 2.12) is also considered. That is Z_{max} is the greatest value of Z which satisfies $E_Z^{min} \leq \sqrt{n_e k T_e / \epsilon_0}$.

The velocity of the cold return current used in the following estimations assumes an electron temperature of about $50eV$ [34]. Recall that for fast ignition $15kJ$ of protons with an average energy of $3MeV$ is required. Assuming that the conversion efficiency from hot electrons to protons is about 50% and that the electron temperature is also about $3MeV$ then for a target with a $200\mu m$ effective diameter and a thickness of $20\mu m$ would have a hot electron density of $10^{23}cm^{-3}$. Densities of about $10^{19}cm^{-3}$ and $10^{20}cm^{-3}$ are typical values corresponding to the laser energies from the two lasers used in the experiment; $10J$ to $150J$. Table 2.2 compares the fraction of ion beam energy partitioned to protons in the cases of CH_2 and ErH_3 for a range of hot electron densities. The two columns on the right show the ratio of the proton fraction for CH_2 and ErH_3. The value of Z for the column on the far right is Z_{max} and for the column left of it is Z_{avg}. Using Z^{max} provides a worst case scenario for the possible benefit of erbium hydride over plastic.

What is observed is that for electron densities of about $10^{22}cm^{-3}$ the fraction of ion energy in protons in the case of erbium hydride falls below that of CH_2. For

	Carbon		Erbium		$\frac{f_p(ErH_3)}{f_p(CH_2)}$	
$n_e(cm^{-3})$	Z_{avg}	Z_{max}	Z_{avg}	Z_{max}	Avg	Max
10^{19}	3.32	4	4.91	13	1.28	1.24
10^{20}	3.67	4	9.79	16	1.26	1.18
10^{21}	3.62	6	17.4	31	1.09	1.11
10^{22}	5.09	6	24.4	40	1.14	0.91
10^{23}	5.15	6	35.0	53	0.91	0.69
10^{24}	3.48	6	42.7	58	0.62	0.63

Table 2.2: Affect of ionization of C vs Er on proton conversion efficiency as a function of n_e with $kT_e = 3MeV$

$10^{19}cm^{-3}$ the erbium hydride produces a 24% to 28% higher fraction of energy to protons.

The bottom line is that for laser energies on the scale of the experiments conducted for this thesis work, erbium hydride should have a better conversion efficiency to protons than plastics or contaminants. The overall improvement should be on the order of about 20% to 30%. For laser energies that are 3 to 4 orders of magnitude greater than the range of this work may see plastics out perform erbium hydride simply because erbium can be ionized to much greater charge states than carbon.

CHAPTER 3

PROTON DIAGNOSTICS

There were two principle diagnostics used in this work. The first was radiochromic film (RCF) packs; useful for measuring several proton beam properties. The second was a Thomson parabola spectrometer; used for measuring the relative ratio of different ion species accelerated with the protons. Other diagnostics were also present during each laser shot. Among those, the single hit CCD spectrometer and the side-on interferometer were useful for comparing different laser shots with similar targets to insure that shot to shot differences in the ion signal were not due to randomly varying laser conditions.

3.1 RADIOCHROMIC FILM

Radiochromic film packs have been demonstrated to be an excellent tool for diagnosing proton beams like those explained in the TNSA model. A typical RCF pack for this work consisted of stacked layers of *GAFCHROMIC*® film along with high impact polystyrene (HIPS) filters. The three kinds of film used listed in order of sensitivity were *HD-810*, *MD-v2-55*, and *HS*; HD-810 being the least sensitive. The active layer of the film is a monomer that polymerizes into a dye when exposed to radiation [35]. Each of these film types darken according to the amount of energy absorbed into the active layer. The film does not require any development or processing before or after exposure. Also, though room lights will add some signal to the background on the film, it is relatively insignificant. Thus, the film can be handled with the room lights on. Lastly, the film can be cut into shapes, used under vacuum, and even placed underwater and still work as designed.

Film packs were wrapped in $25\mu m$ or $50\mu m$ of aluminum foil to prevent exposure from visible/laser light. A typical pack used in a Titan experiment consisted of two $25\mu m$ layers of aluminum foil, six layers of HD-810, and then an alternating series of MD-v2-55 and $16^{th} inches$ HIPS repeating 8 times. For Callisto, a typical pack used $25\mu m$ of aluminum foil, six to seven layers of HD-810, and then five to six layers of HS. Because of the need for the aluminum foil, the lowest proton energy that can be measured in an RCF pack is about $1.5MeV$ if the gel side of the HD-810 faces the target. Carbon ions are also accelerated to high kinetic energies, so the risk of signal contamination from carbon on the first layer of film is also a concern. To avoid this, the first layer of HD-810 is either ignored or all the HD-810 is assembled in the pack with the polyester base facing the target. Either way, this pushes the low energy response of the pack to about $3.4MeV$. The thickness of the active layer may vary 10% from batch to batch and 5% within a batch. This gives rise to an overall uncertainty in the dose of up to 20% [25].

Proton beams from thin foils typically exhibit an $f/1$ beam divergence. To capture the entire beam profile in Titan, $6cm \times 6cm$ packs were placed at $6.5cm$ behind the target. In Callisto, the packs were $2.5cm \times 2.5cm$ and placed $2.5cm$ from the target. A proton with a particular kinetic energy will travel through the film pack, depositing some fraction of its energy as it slows down. Most of the energy will be deposited at the Bragg peak; near where the proton stops. Low energy protons will stop in the first few layers of film, thus giving spectral information. Because the entire beam

		Atomic Percent				**Thick**	**Density**
	Film Layer	**H**	**C**	**N**	**O**	(μm)	**(g/cc)**
HD-810	Polyester Base	36.4	45.5	0.0	18.2	97	1.35
	Active Layer	56.0	31.5	7.5	5.0	6.5	1.08
	Gelatin	53.0	23.0	16.0	8.0	0.75	1.20
HS	Polyester Base	36.4	45.5	0.0	18.2	97	1.35
	Active Layer	56.0	31.5	7.5	5.0	40	1.08
	Polyester Base	36.4	45.5	0.0	18.2	97	1.35
MD-v2-55	Polyester Base	36.4	45.5	0.0	18.2	97	1.35
	Active Layer	56.0	31.5	7.5	5.0	17.5	1.08
	Gelatin	53.0	23.0	16.0	8.0	0.75	1.20
	Acrylic Adhesive	57.1	33.3	0.0	9.5	32	1.20
	Polyester Base	36.4	45.5	0.0	18.2	25	1.35
	Acrylic Adhesive	57.1	33.3	0.0	9.5	32	1.20
	Gelatin	53.0	23.0	16.0	8.0	0.75	1.20
	Active Layer	56.0	31.5	7.5	5.0	17.5	1.08
	Polyester Base	36.4	45.5	0.0	18.2	97	1.35

Table 3.1: The composition and structure of the three kinds of gafchromic®radiochromic film used under vacuum conditions [35].

is captured on the film pack, it is also a reliable means of measuring the overall conversion efficiency from laser to protons.

3.1.1 CALIBRATION

The RCF was calibrated using the cyclotron at the University of California, Davis Campus's Crocker Nuclear Laboratory. Calibrated film for HD-810 and HS had already been produced for a previous graduate student's work [25]. For this work it was necessary to repeat the procedure for MD-v2-55 since the manufacturer has made this the replacement film for the now discontinued HS. To verify consistency with the new calibration, HD-810 was also included. The Crocker cyclotron produces mono-energetic protons with kinetic energies of up to $68 MeV$. The cyclotron can be configured for lower energies as well. The facility is routinely used for radiation testing and for eye cancer proton therapy. Protons are an excellent choice for cancer treatment because the beam can be tuned to deposit most of its energy into the tumor resulting in less collateral damage than conventional radiation treatments.

To calibrate the film, a pack consisting of one of each kind of film was made, starting with the least sensitive and then covering the pack in $25 \mu m$ of aluminum. The pack was then exposed to a $1cm \times 1cm$ square beam of protons with kinetic energies of $63.5 MeV$. Figure 3.1 and figure 3.2 show the setup and exposed film respectively. The high energy protons deposit less than $1 MeV$ each into the active layer of each piece of film. The total proton exposure to the film was controlled by setting the proton flux on the cyclotron and fixing the duration of the beam. The amount of energy absorbed by the active layers of each type of film was computed by integrating stopping powers provided by SRIM [36]. The integration was done with the MATLAB®script shown in appendix A. The total dose in the $1cm^2$ patch was computed as the absorbed energy per proton to the active layer times the proton fluence divided by the film active layer's density times the total thickness of the active layer ($\Delta\mathcal{E} \times (\#\text{ of protons}/cm^2)/\rho\tau$). The thickness and density of the active layer are presented in table 3.1.

After exposure, RCF will continue to darken gradually until it stabilizes after two days [35]. The film was scanned one week after exposure insure that it had reached its asymptotic optical density. The scanner used was the Nikon™Super Coolscan 9000ED. This Nikon product is a professional film scanner which is capable of digitizing the exposed RCF into 16-bit images and can handle optical densities up to 3.05. To test the reliability and range of the scanner, a transmission filter with increasing steps of $0.3 OD$ was scanned. For the resolution used to analyze the data

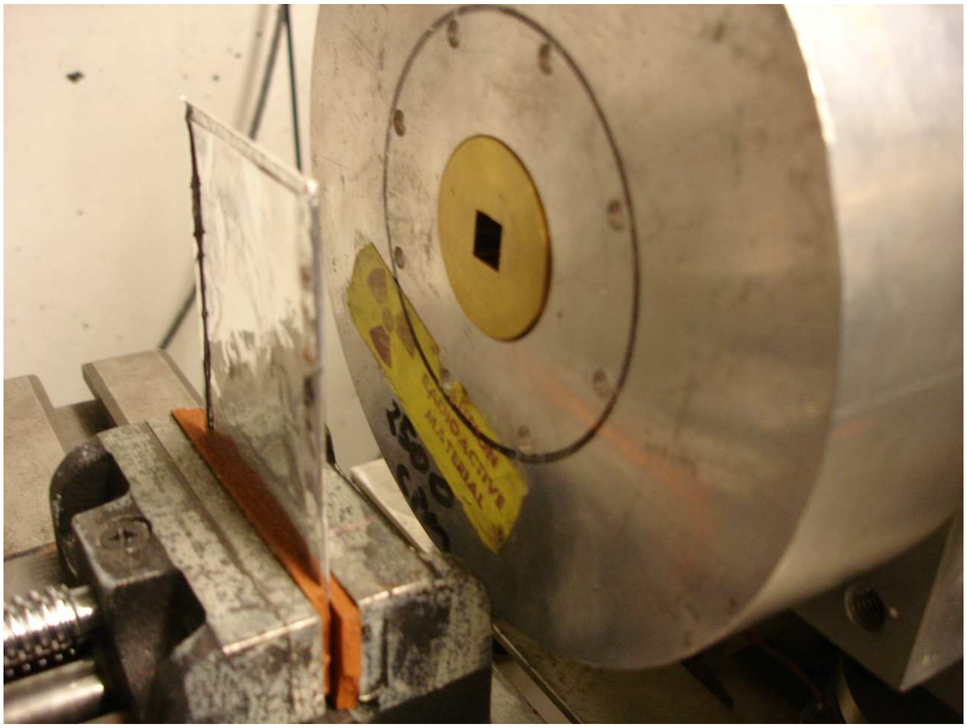

Figure 3.1: Picture of the RCF calibration pack positioned in front of the cyclotron beam output at CNL.

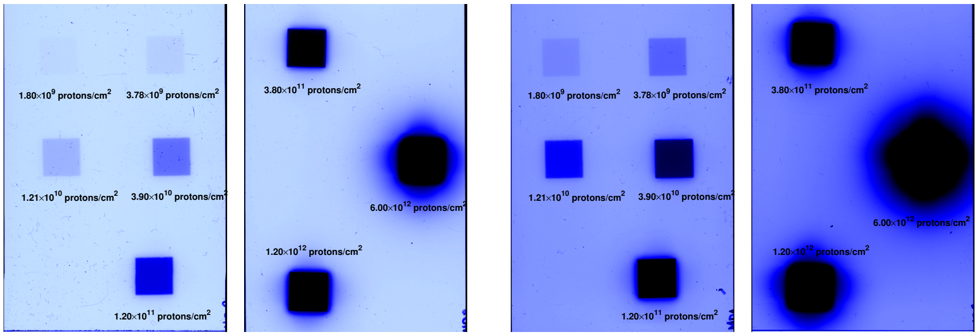

Figure 3.2: Exposed HD-810 and MD-v2-55 film from CNL. On the left is the HD-810 from two packs; one for low proton fluences, and one fore high. On the right are the MD-v2-55 film layers that were positioned behind the HD-810.

(10 pixels per mm) the step from 2.75 to 3.05 was clearly visible through the noise. Figure 3.3 shows the image line-out. This range is suitable since the RCF response becomes nearly flat for densities above 3.0 [25].

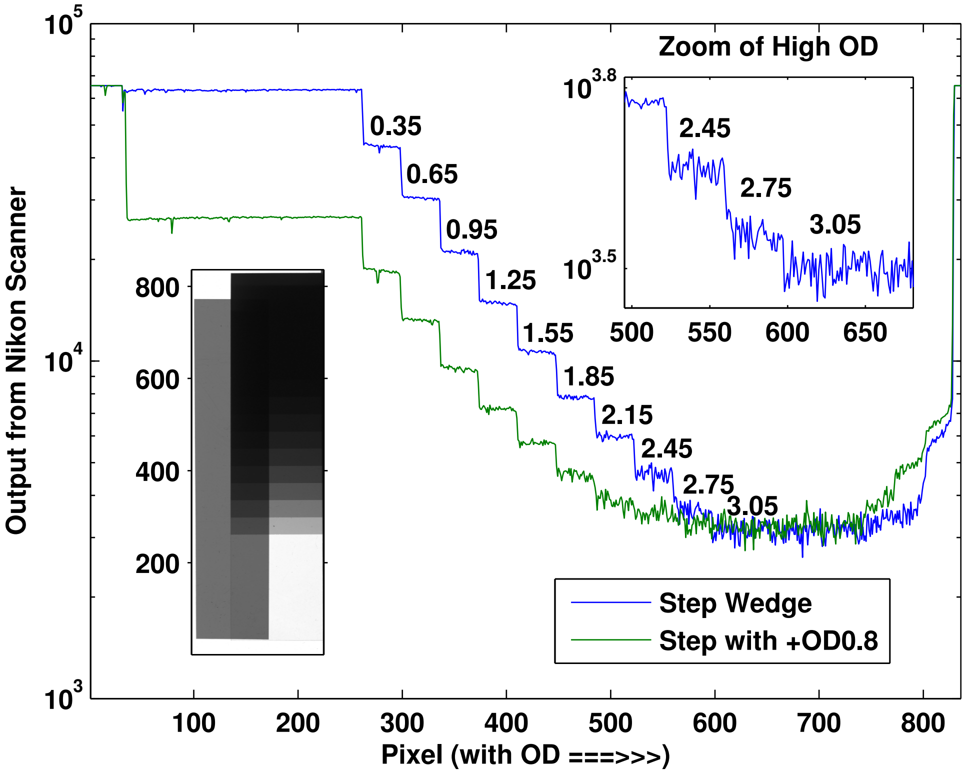

Figure 3.3: Optical Density Range of the Nikon$^{\mathrm{TM}}$Super Coolscan 9000ED. A step wedge was scanned using the Nikon scanner to determine the optical density range of the scanner.

The pixel values of the scanned Crocker Nuclear Lab film was plotted against the calculated doses from the known proton fluences (fig 3.4). The fog level of the film was subtracted from the pixel values. The pixel to dose response was of the functional form,

$$\log_{10}(D_i) = A\sinh(Bx - C) + F + Gx, \tag{3.1}$$

Film Type	**A**	**B**	**C**	**F**	**G**
HD-810	5.87×10^{-8}	37.9	17.8	0.474	1.97
MD-v2-55	2.62×10^{-8}	44.8	18.2	-0.299	2.27
HS	1.01×10^{-4}	24.9	10.1	-0.550	2.29

Table 3.2: The fit parameters for the dose to pixel value for the RCF using equation 3.1.

where $x \equiv (pixel - fog)/65535$ and D_i is the dose at the i^{th} pixel. The values for the fit parameters are listed in table 3.2.

3.1.2 METHOD OF ANALYSIS

Analysis of the RCF pack data was straight forward. After a shot, the film from a pack was digitized using the Nikon scanner. The fog level of the film was found by taking the average pixel value near a corner of the film where no protons were present. Each pixel was then converted into a dose value using equation 3.1. Because each pixel has the same area, the total dose on a piece of film is equal to the average dose value of the pixels. The total energy absorbed by the active layer(s) of the n^{th} piece of film is

$$\mathcal{E}_n = \rho A \tau \langle D_i \rangle. \tag{3.2}$$

The area A is the total area of the film equal to the number of pixels times the area of one pixel. The density and thickness of the active layer of the film is given by ρ and τ respectively.

To get the proton spectrum for the shot it was first necessary to determine how much energy is absorbed by each layer of film in the pack by a single proton with kinetic energy $\mathcal{E}$. Call this function $\Delta\mathcal{E}_n(\mathcal{E})$ for the n^{th} layer of film. The correct

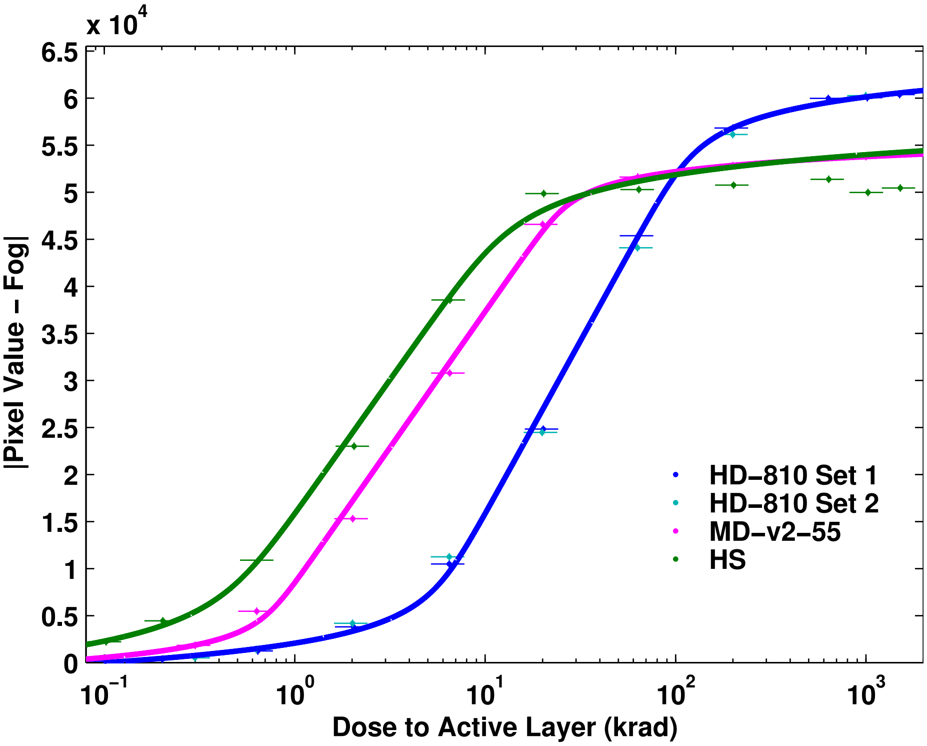

Figure 3.4: Calibration curves from the CNL exposures. The dots are the pixel values for the known doses. The solid lines are fits to the data.

proton spectrum is the distribution $dN/d\mathcal{E}$ that satisfies

$$\int_0^\infty \Delta\mathcal{E}_n \frac{dN}{d\mathcal{E}} d\mathcal{E} = \mathcal{E}_n, \tag{3.3}$$

for all values of n. The amount by which the film darkens for a given amount of absorbed energy does differ slightly for high energy protons versus low energy protons whose Bragg peak is near the active layer [25]. To account for this, a third factor which normalizes the full proton energy range to that of the 63.5 where the film was calibrated should be included. However, the overall affect of this is small and since the experimental goal was to measure a relative difference in the conversion efficiency it has been neglected in my analysis.

Most proton distributions observed tended to be either Maxwellian or Boltzmann like with either a one or two temperature behavior. There was also a sharp high temperature cutoff. The data from Callisto fit nicely to

$$\frac{dN}{d\mathcal{E}} = \frac{2N_0\sqrt{\mathcal{E}}}{\sqrt{\pi}(kT_p)^{3/2}} \cdot e^{-\mathcal{E}/kT_p} \text{ if } \mathcal{E} \leqslant \mathcal{E}_c, \tag{3.4}$$

where N_0 is the total number of protons, kT_p is the temperature and $\mathcal{E}_c$ is the high energy cutoff. Titan data required a two temperature, piecewise defined function,

$$\frac{dN}{d\mathcal{E}} = A \begin{cases} \mathcal{E}^\alpha e^{-\mathcal{E}/kT_{p,c}} & \mathcal{E} \leqslant \mathcal{E}_0 \\ \mathcal{E}_0^\alpha e^{-\mathcal{E}_0/kT_{p,c}+(\mathcal{E}_0-\mathcal{E})/kT_{p,h}} & \mathcal{E}_0 \leqslant \mathcal{E} \leqslant \mathcal{E}_c \end{cases}, \tag{3.5}$$

where $kT_{p,c}$ is the cold slop temperature observed at the low energy part of the spectrum, $kT_{p,h}$ is the high temperature tail, E_0 is the joining point of the two distributions and α is a parameter ranging from 0 to 3. Figure 3.5 shows an example of a Titan shot that was fit using this distribution. The y-axis gives the measured dose in kilorads for each piece of film and the x-axis is the minimum kinetic energy a proton would have to have to even reach that layer of film. The plot in the sub-axes is the distribution $dN/d\mathcal{E}$ that gave the best match to the data. Note that the 7-th layer of film was excluded from the fit. This is because it was the first layer of MD-v2-55 to appear in the pack and was saturated.

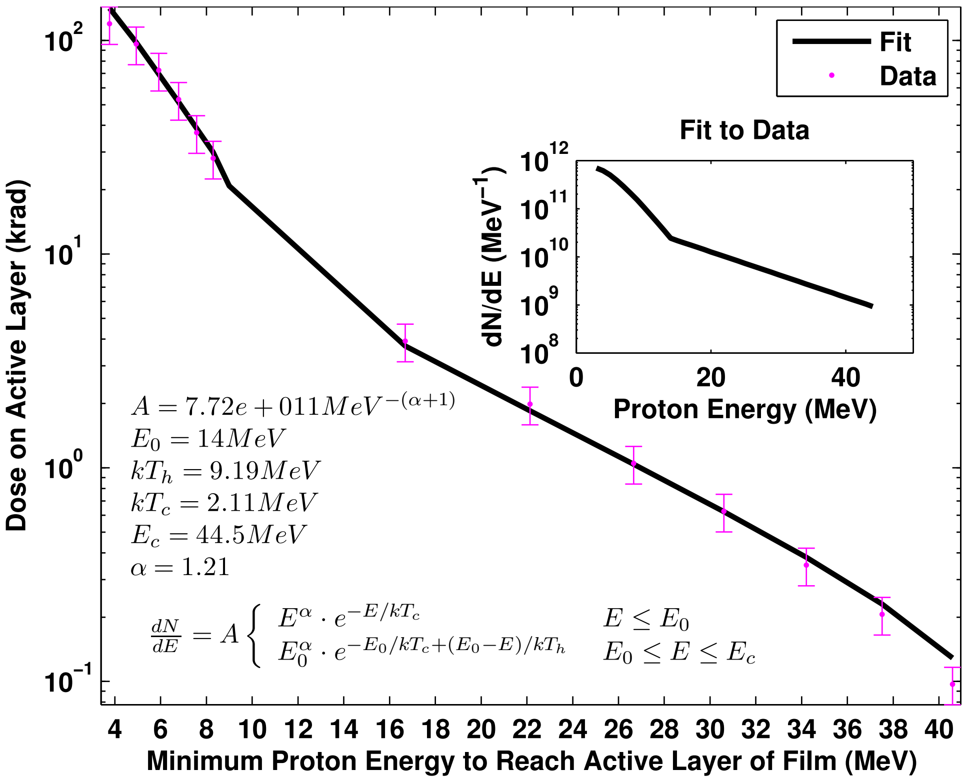

Figure 3.5: Titan RCF data with $dN/d\mathcal{E}$ fit. The points are the dose measured on each piece of film divided by the laser energy. The line is from using the fit distribution integrated against the film pack response to reproduce the measured values.

3.2 THE THOMSON SPECTROMETER

The Thomson spectrometer is a magnetic and electric field spectrometer in which the $\vec{E}$ and $\vec{B}$ fields are parallel. The result is orthogonal terms in the equations of motion of a charged particle with mass m and charge q with an initial velocity in the z-direction v_z, $m\vec{a} = qv_zB\hat{x} + qE\hat{y}$. Solving the system for the amount of time the particle travels the longitudinal distance $z = v_zt$ (assuming $v_z \gg \Delta v_x$ due to the magnetic field), the total displacement in the x-direction is proportional to $(q/m)(1/v_z)$ and $(q/m)(1/v_z^2)$ in the y-direction. For a distribution of v_z, in the x-y plane, one gets parabolic traces where $y \propto (m/q)x^2$. Thus depending on the charge to mass ratio there will be a different trace, and any point along that trace will give the initial kinetic energy of the particle.

3.2.1 CHARACTERISTICS

For these experiments, a Thomson spectrometer designed and built at the Rutherford Appleton Laboratory (RAL) Central Laser Facility (CLF) was borrowed. The spectrometer had permanent nickel plated neodymium magnets for the B-field and angled plates for the E-field. The angled plates allowed for better separation of the charge to mass traces on the detector plane than what could be achieved using parallel plates [37, 38].

The angled electric plates means the electric field is not constant along the ion trajectory. Rather it depends on z according to

$$\vec{E} = [V/(h + z\tan(\theta))]\hat{y}. \tag{3.6}$$

Assuming that the fringe fields are negligible, then the position of a particle with charge q, mass m and initial velocity v_z at the detector plane can be calculated from

Newton's second law. The angle between the plates, θ, is 5.8°. The total displacement in either x or y is the sum of the change that occurs within the field and the change which occurs outside the field. The change outside is simply the free flight tangent to the point where the particle exits the field.

$$\begin{aligned} x &= \frac{1}{2}\frac{q}{m}B\frac{1}{v_z}\left[z^2|_{z=z_1} + (z_2+z_3-z_1)\frac{\partial}{\partial z}\left(z^2\right)|_{z=z_1}\right], \\ y &= \frac{q}{m}\frac{V}{v_z^2\tan^2\theta}\left[\left((h+z\tan\theta)\ln\left(\frac{z}{h}\tan\theta+1\right)-z\tan\theta\right)|_{z=z_2}\right. \\ &\quad \left. + z_3\frac{\partial}{\partial z}\left(\left((h+z\tan\theta)\ln\left(\frac{z}{h}\tan\theta+1\right)-z\tan\theta\right)\right)|_{z=z_2}\right]. \end{aligned} \tag{3.7}$$

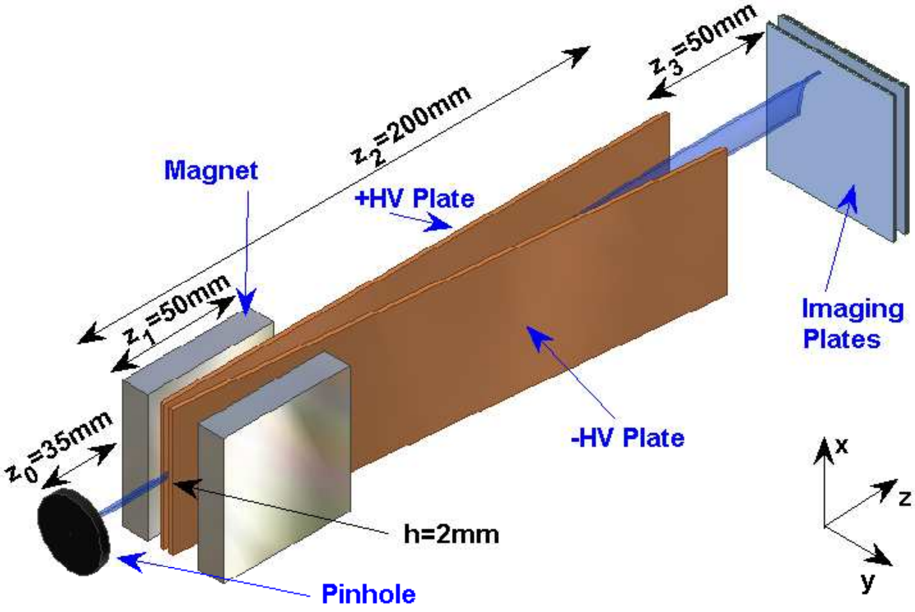

Figure 3.6: A diagram of the Thomson parabola spectrometer showing the dimensions of the major components; pinhole, magnets, electric plates and detector. The angle between the plates is 5.8°.

Typical values for the voltage and magnetic field strength are $4kV$ and $0.6T$, respectively. The dimensions of the major components for the spectrometer are shown in figure 3.6. Plugging in values for each parameter, equation 3.7 reduces to the same proportionality as the parallel plate case. The parabolic traces are,

$$y = p\frac{M}{Z}x^2, \tag{3.8}$$

where M is the ion mass divided by the mass of hydrogen, Z is the charge of the ion divided by the unit charge e and p is a constant. In the displacement from the magnetic field, x, the kinetic energy is give by,

$$\mathcal{E} \cdot x^2 = A\frac{Z^2}{M}. \tag{3.9}$$

The constants p and A were empirically determined by placing a $25\mu m$ aluminum foil filter over the detector and find the x and y values that correspond to the minimum proton kinetic energy that can penetrate the filter. Figure 3.7 illustrates the result from shots taken on Callisto. Here, A is equal to $16.4MeV \cdot cm^2$ and p is $0.05cm^{-1}$ when $4000V$ is applied to the electric plates. For the proton trace, the deflection due to the electric field is small compared to that of the magnetic field, so equation 3.9 is sufficient for determining the energy. For more massive ions the deflection in y is greater. By dividing equation 3.8 by equation 3.9, the relation $E \cdot y = pAZ$ is more accurate. This is because the uncertainty in energy is inversely proportional to the square of y, which for heavier ions is larger than x which gives an uncertainty inversely proportional to the cube of x using equation 3.9.

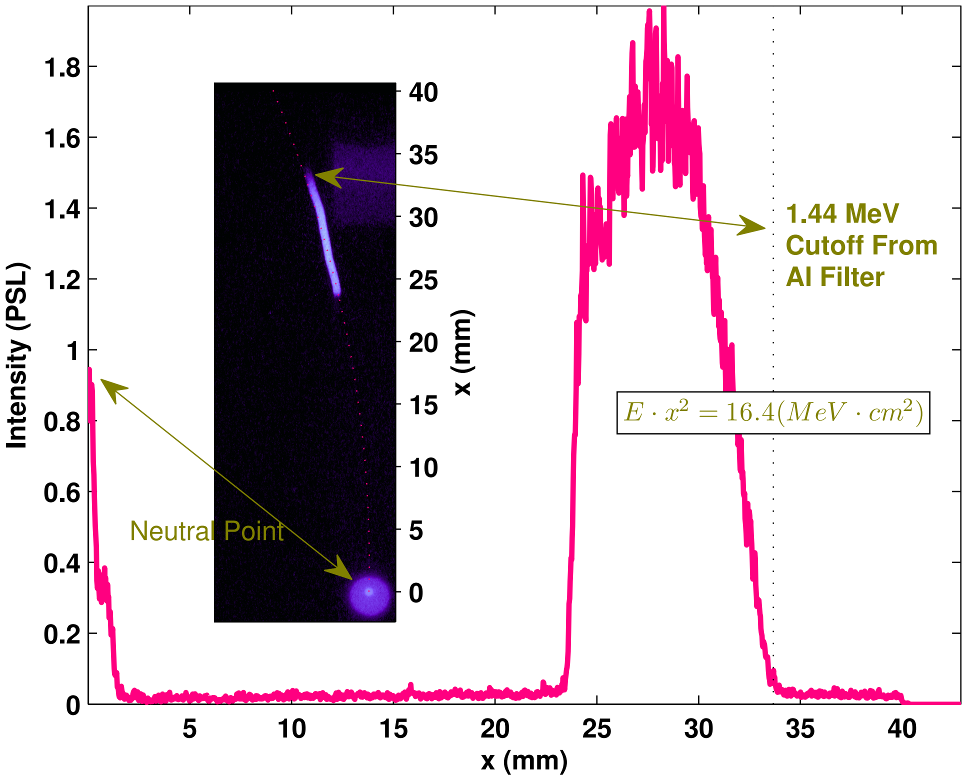

Figure 3.7: Calibration of the energy scale of the Thomson spectrometer. A $25\mu m$ Al filter was placed over the Imaging Plate so there would be a low energy cutoff of $1.4MeV$.

3.2.2 IMAGING PLATES AS A DETECTOR

The RAL Thomson spectrometer was designed to use CR-39 and the detector. This plastic which is used to make the lenses in most sun glasses is ideal since it is insensitive the the x-ray signal. Detection comes in the form of damage tracks formed when ions stop in the material. The size and depth of the damages are functions of the ion mass and energy. Soaking the exposed plastic in a hot bath of sodium hydroxide will enlarge the damages so that they can be easily resolved on a microscope. The total number of ions at a particular energy range can be determined simply by counting the number of damages. The energy range of visible damages depends on how long the CR-39 was etched. A complete spectrum for different ions can be obtained by iteratively etching and counting the tracks. To help in this process, a special scanner and custom software package capable of identifying the ions was built at RAL.

In these experiments, the Thomson spectrometer was less important for obtaining absolute ion numbers. Rather, what was sought was the relative difference in ion species for different target configurations. Imaging plates (IP) made by FUJIFILM Global^{TM}were used instead [39]. Imaging plates use a phosphor layer ($BaFBr_{0.85}I_{0.15} : Eu$) that when exposed to radiation stores energy as defect centers in the crystal lattice [40]. Irradiating the IP with a red, $633nm$, cw read laser results in stimulated emission of blue, $390nm$, photons that are detected and digitized by a photomultiplier tube (PMT). The read laser is focused and scanned over the surface of the IP so that a complete image is scanned. The number of photons read is proportional to the amount of energy absorbed in the IP's active layer. Because the number of excited state emitters decreases when scanned, data that appears saturated can be scanned again and will have a reduced but proportional signal. Two major advantages of imaging plates are that data can be quickly obtained (relative to CR-39) and that each imaging plate is reusable. An exposed IP can be erased fully with an ultraviolet lamp and ready for another use in under 20 minutes.

There are several types of imaging plates available. Each differs in the thickness of the different layers, the number and types of layers, and the overall concentration of the phosphor, $BaFBr_{0.85}I_{0.15}$, in the active layer. Data on the structure and composition was provided by the FUJIFILM$^{\mathrm{TM}}$life sciences sales representative. Inconsistencies in the data provided have lead to some confusion about the density and composition, so a memo was written by C. Chen [41] to interpret what was given. For this work, *BAS-TR* was used. For additional information on the x-ray background and proton spectra, a second IP type, *BAS-SR* was placed behind the BAS-TR. The structure of both of these IP types is shown in figure 3.8. In both film types phosphor is suspended in a urethane mixture. The BAS-SR has a $7\mu m$ protective overcoat which stops ions; making it a poor choice for use in the Thomson spectrometer. The BAS-TR on the other hand has a bare active layer. Both film types also have a base layer which consists of MnO, ZnO, and $Fe203$ suspended in a plastic mixture assumed to be PET. This layer is used to hold the film in the scanner which uses a magnet to secure the imaging plates. The mass ratio of the phosphor to the urethane is 20:1 for both types of film. For BAS-TR the densities of the three layers are $2.7g/cc$ for the active layer, $1.3g/cc$ for the undercoat, and $1.4g/cc$ for the base. For the BAS-SR the densities are $1.5g/cc$ for the overcoat, $3.2g/cc$ for the active layer, $1.5g/cc$ for the undercoat, $1.4g.cc$ for the base, and $2.8g/cc$ for the back.

The FUJIFILM$^{\mathrm{TM}}$scanner used was the FLA-7000. The scanner settings include three levels of PMT sensitivities, S, (S1000, S4000, and S10000); four resolutions, R, ($25\mu m$, $50\mu m$, $100\mu m$, and $200\mu m$); and two latitude settings, L, (L4 and L5). The latitude is the orders of magnitude of analog data values that are digitized into the 16-bit image. The output file of the scanner is a RAW image file format with the

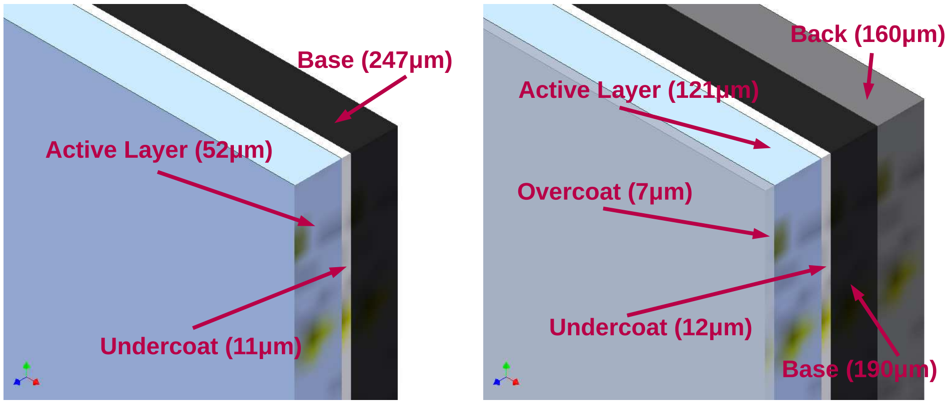

(a) BAS-TR

(b) BAS-SR

Figure 3.8: The structure of FUJIFILM$^{\mathrm{TM}}$imaging plates. Data was provided by the FUJIFILM$^{\mathrm{TM}}$life sciences sales representative. On the left is BAS-TR, and on the right is BAS-SR.

extension *.img along with a settings information file *.inf. The 16-bit pixel values in the IMG file are called quantum levels (QL). FUJIFILM provides a formula which converts quantum levels, which have a logarithmic response to the intensity of stimulated photon emission, to linearized quantity called photo-stimulated luminescence (PSL).

$$PSL = \begin{cases} \dfrac{4000}{S}\left(\dfrac{R}{100}\right)^{2} 10^{\left[L\left(\frac{QL}{65535}^{-1/2}\right)\right]} & \text{if } QL > 0 \\ 0 & \text{if } QL = 0 \end{cases} \tag{3.10}$$

A typical proton spectrum varied less than 3 orders of magnitude in intensity and the tracks from the Thomson had a $200\mu m$ width. Therefore, the ideal settings used were S1000, $25\mu m$, and L4.

For this work, an absolute calibration of the imaging plates was not obtained. A few things must be considered, however, when considering the IP's relative response to ions,

1. The stopping power of the IP for each ion species [42, 39],
2. The fade time associated with the natural decay of the photo-emitters of the active layer [43],
3. The skin depth of the scanner's read laser into the IP [40, 44],
4. The attenuation of stimulated photons by the IP before they can reach the PMT [40, 44],
5. And if multiply scanned, the fraction of erased emitters from each scan [40, 44].

The fade time is the decay of the photo-emitters in the active layer. This is an important effect that must be considered when comparing multiple imaging plates. The effect is independent of the total initial density of photo-emitters, though it is highly dependant on the temperature. For a given temperature the decay can be expressed as a sum of exponential decays. This phenomenon has been well studied and and presented in a paper by O. Hiroko, *et al* [43] for the type BAS-TR imaging plate. The ratio of the signal at time t at a temperature T in kelvin is,

$$\begin{aligned} PSL(t)/PLS_0 = \quad & 0.461 \exp\left[-2.19 \times 10^{8} t \exp\left(-6.14 \times 10^{3}/T\right]\right) \\ & +0.277 \exp\left[-1.60 \times 10^{13} t \exp\left(-1.02 \times 10^{4}/T\right)\right] \\ & +0.230 \exp\left[-7.98 \times 10^{12} t \exp\left(-1.05 \times 10^{4}/T\right)\right] \\ & +0.030 \exp\left[-1.99 \times 10^{12} t \exp\left(-1.05 \times 10^{4}/T\right)\right] \\ & +0.002 \exp\left[-4.96 \times 10^{10} t \exp\left(-1.05 \times 10^{4}/T\right)\right]. \end{aligned} \tag{3.11}$$

The relative difference in the signal becomes less significant if the imaging plates are all scanned after approximately one hour. In the experiments for this work, the imaging plates were scanned after $20min$ in the Callisto experiment and $40min$ in Titan. This was also partly due to coordinating the shared time at the scanner with experimenters from other groups using one of the five other major laser systems in the facility.

Considering the stopping power of the imaging plate, one would expect that for the typical peak ion energies observed in experiments of the non-hydrogen atoms accelerated from thin foils would stop entirely within the active layer. Thus, the PSL signal should be proportional to the ion's initial kinetic energy. However the red reading laser in the scanner will become diffuse as it propagates into the imaging plate. This means the total fraction of the absorbed ion energy detected will be higher for low energy ions which stop near the surface. The difference is dependant on the intensity of the read laser. This low energy weighting is made worse by the fact that the stimulated blue photons are also attenuated in the same way.

Protons, however, have a longer range in the imaging plate material. For kinetic energies above $\approx 3MeV$, less than the total energy of the proton is being absorbed by the active layer. For proton energies significantly higher than $3MeV$, the energy absorbed per unit depth into the IP's active layer becomes nearly constant. Because $3MeV$ protons are of the highest interest for fast ignition, imaging plates are not the best choice for dosimetry.

One final point for consideration when collecting data using imaging plates is the affect of scanning multiple times. For an exposed imaging plate, the signal read and digitized by the scanner may appear partially saturated. However if this happens, a fraction of the of the defect centers in the active layer still remain and can be subsequently scanned with a reduced signal.

To study this effect and produce a scale factor to correct for data where the number of scans differed, an IP was scanned several times past the point where any saturated pixels were showing. Figure 3.9 shows the fraction of signal lost due to scans. The percent reduction in PSL signal from one scan to the next at different places on the

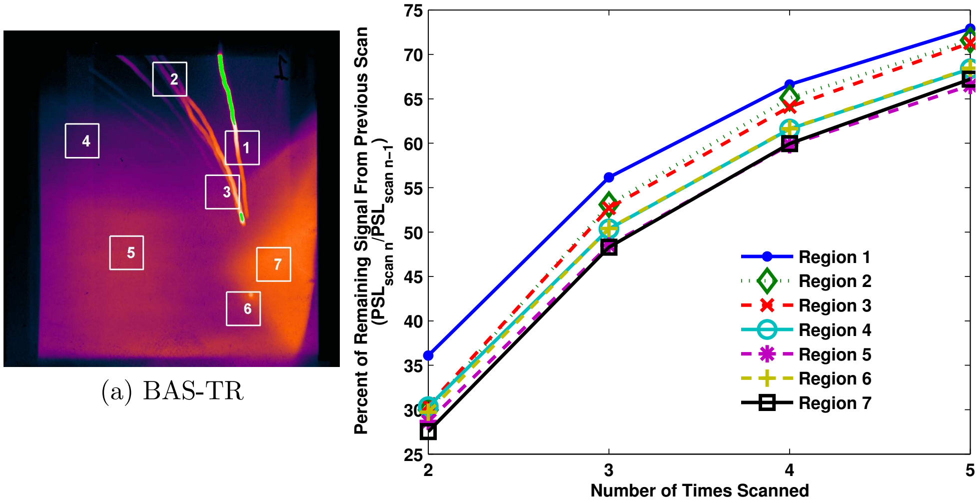

(a) BAS-TR

(b)

Figure 3.9: The fractional loss of the PSL signal due to re-scanning. The curves on the right are taken from the average value within the numbered boxes on the left. Points on each curve are the ratios of PSL signal of the n^{th} to the scan just before it. Box 1 contains $\approx 2MeV$ protons that deposit energy deep within the active layer. Box 2 contains signal from carbon that stops nearer to the surface. Box 3 contains higher energy signal from carbon. Box 4 contains high energy x-ray signal. Box 5 contains a large signal from low energy x-rays. Box 6 contains the neutral point which has a mixture of proton can carbon signal. Box 7 contains very low energy background signal from the etcher.

image from a Thomson parabola spectrum was compared. The images on the IP typically have three features. The first is the ion traces. Second is an overall uniform background due to high energy x-rays, and the third are low energy x-rays which for a radiograph of the internal components of the spectrometer. What was observed was that regions where the signal was high due to low energy photons experienced the highest fractional loss of the signal after the first scan. This was because most low energy photons are absorbed near the surface where the read laser is at its highest intensity. Additionally, the loss decreases after several scans. This was likely because the defect centers near the surface were depleted in the first couple of scans.

3.3 OTHER DIAGNOSTICS USED

The difference in the proton conversion efficiency due to the erbium hydride is small, so a single hit CCD and a side-on interferometer were used to rule out the possibility that other laser effects are responsible for observed differences. The side-on interferometer measures the plasma scale length at both the front and rear surfaces of the target. Changes in the plasma length at the front surface is indicative of changes in the intensity of the pre-pulse. The single hit CCD counts the XUV photons emitted from the target. Since the laser parameters (i.e. focus, pulse length, energy, *etc*) and target thicknesses were kept constant in this experiment, the XUV spectra should be identical.

3.3.1 SIDE-ON INTERFEROMETRY

Side-on interferometry is an effective method for measuring the plasma density [45]. In this diagnostic, a short-pulse laser probe illuminates the target with the beam parallel to the target plane. The beam used is a pick-off of the primary laser used in the experiment so that it can be synchronized in time to be nearly simultaneous with the primary beam. For this experiment the probe was chosen to arrive $50ps$ early. As the probe travels through the plasma formed at the surface of the target it picks up a phase change $\Delta\phi = \int_{\mathbf{l}} n d\mathbf{l}$, where the line integral is over the path l and n is the index of refraction of the plasma. This can be related to the plasma electron density, n_e, by the well known relationship $n = (1 - n_e/n_c)^{1/2}$. The critical density $n_c = (1.11^{13} cm^{-1})\lambda^{-2}$ which depends on the wavelength of the probe laser is the upper limit that can be probed. At this density the plasma acts like a perfect mirror to the probe. It is advantageous to frequency double the probe for transmitting through higher plasma densities and to separate the probe from the bright scattered light from the primary laser with color filters.

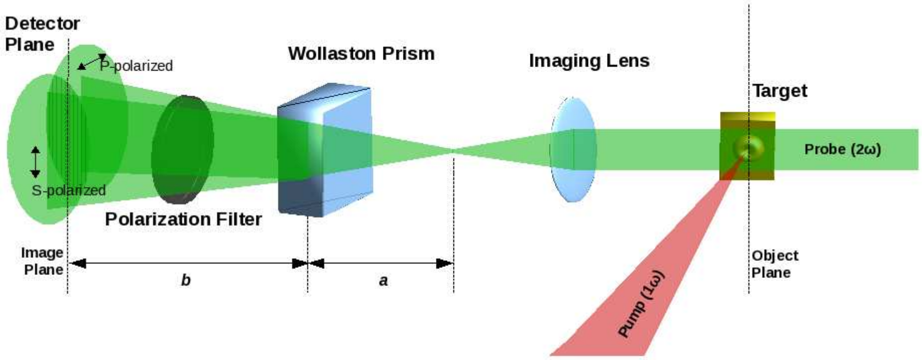

Figure 3.10: An Illustration of the Nomarski imaging interferometer. The Wollaston prism separates the two polarizations of the probe into diverging paths separated by an angle ϵ.

The phase shift can be measured by imaging the target through a Nomarski interferometer seen in figure 3.10. The Wollaston prism splits the polarized light from the probe into two orthogonal components separated by a full angle ϵ. By placing the prism after the focus of the imaging lens, the image plane will see two virtual point sources. The overlapping light from these sources will interfere with a fringe spacing

$$\delta = \frac{b\lambda}{a\epsilon}, \tag{3.12}$$

according to the wavelength, λ, and the geometry of the interferometer seen in figure 3.10. The best contrast occurs when a polarization filter is used to match the intensity of the S and P polarizations. A CCD camera at the image plane measures the fringe shift over the 2-D image of the side-on view of the target. Examples of interferometer data can be seen in section 4.

The ratio Δ of the fringe shift to the fringe spacing is given by the line integral,

$$\Delta = \frac{1}{2\lambda n_c} \int_{\mathbf{l}} n_e d\mathbf{l}, \tag{3.13}$$

where $\mathbf{l}$ is the path of the probe laser through the plasma. To reconstruct the full 3-D plasma density profile from the 2-D data an Abel inversion is often used.

3.3.2 SINGLE HIT CCD

A CCD camera filtered such that only single photons are incident on the chip array has been used successfully in many experiments measuring x-ray line emission in petawatt laser experiments [46, and references therin]. The voltage level read on a particular pixel is proportional to the incident photon energy. Thus, taking a histogram of a single photon counting image will produce an x-ray spectrum. Typically the single hit CCD diagnostic is used to measure K_α photon yields. When a relativistic electron ionizes a K-shell electron from an atom, a photon is emitted when the hole is filled. From that data, a total energy for the hot electrons produced can be inferred.

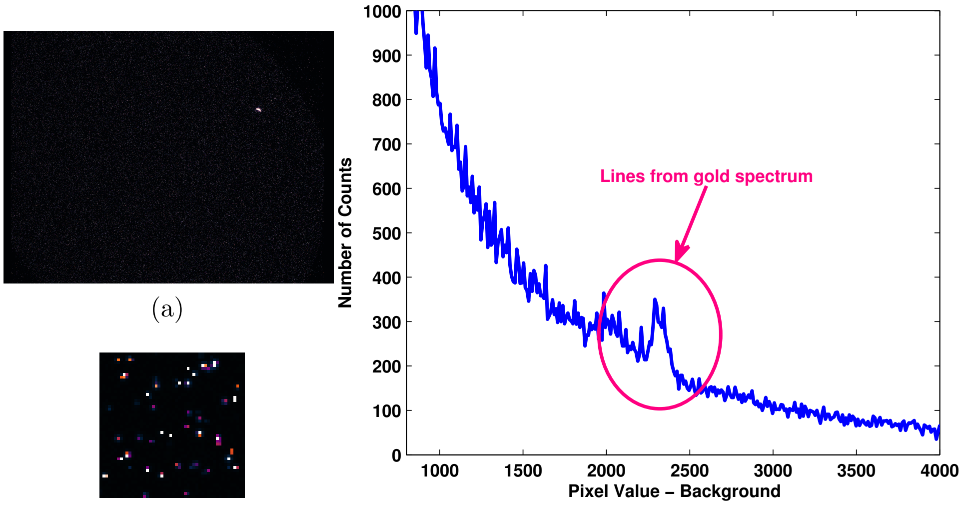

(a)

(b)

(c)

Figure 3.11: Sample single hit CCD data. (a) Raw data image after background subtraction. (b) Zoom on pixels from raw data. (c) Histogram of single hit image.

Most cameras have an optically transparent coating over CCD array to protect it from damage. The CCD camera used in this diagnostic has a bare chip for x-ray detection. To reduce the thermal noise on the camera it is cooled to temperatures between $-20C$ and $-40C$. A beryllium filter is places directly over the chip to block all visible light. The beryllium is transparent to x-rays. The best control for keeping the camera in a single photon counting regime is to place it far from the target. This keeps the total number of hard hits due to gama rays to a minimum as well as the number of desired photons by decreasing the amount of solid angle being sampled.

The number of K_α photons, N_α, produced by the normalized relativistic ion distribution $f(\mathcal{E}, T_e)$ is expressed by [47],

$$\frac{d^2 N_\alpha}{dx d\mathcal{E}} = \eta \rho_{atom} N_e f(\mathcal{E}, T_e) \sigma_K(\mathcal{E}), \tag{3.14}$$

where η is the quantum fluorescence, ρ_{atom} is the density of atoms in the target, and σ_K is the crossection of K_α ionization. For thin targets the number is also enhanced by hot electrons which reflux though the target multiple times.

Assuming that the x-ray emission of the target is isotropic, the total number of detectable K_α photons is given by,

$$N_{\alpha,det} = (Q.E.) \prod_i (T_{i,filter}) \frac{A}{4\pi d^2} N_\alpha, \tag{3.15}$$

where $Q.E.$ is the quantum efficiency of the camera, d is the distance of the camera to the target, A is the area of the CCD chip, and T_i is the percent photon transmission through the i^{th} filter including propagation through air.

For the purposes of this work, it was not necessary to know the absolute electron density and temperature. The targets shot for comparison of proton conversion efficiency each had the same thickness and material. The filters and alignment of the single hit CCD did not change. Any relative change in the absolute number of counted photons was sufficient to know if something had changed in the laser and target conditions.

CHAPTER 4

HYDIRDE EXPERIMENTS

To observe the predicted benefit of erbium hydride over the typically used contaminant originating proton beams two experiments were conducted the the Lawrence Livermore National Laboratory's Jupiter Laser Facility. The the first experiment was on the Ti:Sapphire based CPA Callisto laser system. The second was the on the higher energy OPCPA based Titan laser system. In this chapter details about the targets, experimental setup, and observed results from the principle diagnostics are presented.

4.1 TARGETS

The targets used in these experiments were produced at Sandia National Laboratory by coating gold foil over a glass substrate followed by coating erbium hydride over the gold. The targets can be described in four categories;

1. gold foils with an erbium hydride layer and a contaminant layer
2. gold foils with an erbium hydride layer only
3. gold foils with a contaminant layer only
4. gold foil with no contaminants or hydride layers.

The area of the hydride coating was smaller than the gold coating which allowed targets to be cut from the sample edges which were free of hydrides. Every surface of the sample had a contaminant layer at the surface which was unavoidable. Without a means of removing the contaminant layer all the irradiated targets would have been in categories 1 or 3. To observe the conditions described by categories 2 and 3 an argon ion sputtering gun was used to remove the contaminant layer.

4.1.1 SPECIFICATIONS

When the targets were made, either $5\mu m$ of gold or $14\mu m$ of gold was coated onto a one inch diameter glass substrate. The erbium hydride was coated over a smaller diameter over the gold to a thickness of $200nm$. Erbium hydride itself is not a molecule. Rather, it is like a solution of erbium and hydrogen. To insure that the coating was ErH_3 and not some other hydride such as ErH_2, x-ray diffraction measurement of the the surface performed at Sandia confirmed that the lattice structure was that of ErH_3.

The surface analysis was conducted at LLNL using x-ray photoemission spectroscopy. In this measurement, a sputtering gun was used to remove a finite thickness of material while measuring the x-ray spectrum to identify the atomic species at the surface. So in addition to the the composition of the surface layer, the thickness of each layer was also determined. For each target, the structure from front to back was $5\mu m$ or $14\mu m$ of gold, $200nm$ of ErH_3, a $4nm$ thick oxide layer, and a $1nm$ thick contaminant layer. The composition of the contaminant layer is presented in table 4.1. Because the targets without erbium hydride were cut from an edge of the same sample having erbium hydride, the contaminant layer was assumed to be approximately the same.

Atom[a]	Atomic Percent
Carbon	49.8
Nitrogen	1.3
Oxygen	36.7
Fluorine	1.4
Erbium	10.8

[a] Hydrogen was not directly detectable

Table 4.1: Composition (Atomic Percent) of the contaminant layer for $Au - ErH_3$ and Au targets.

One drawback to the x-ray photoemission measurement was that the hydrogen x-ray signal was not detectable. The presence of hydrogen must therefore be inferred from the abundance of carbon and oxygen. If one assumes that the carbon and oxygen detected are molecular CH_2 and H_2O then the density of hydrogen can be estimated in the following way. First, assume that the contaminant layer has the density of gasoline [7], which is about $1g/cc$. The total number of hydrogen atoms is approximately the mass density times Avogadro's number times the number of hydrogen atoms per pseudo-molecule (stoichiometry from table 4.1) divided by the mass per mole of that pseudo-molecule. The result is,

$$\frac{\rho N_a (2a_C + 2a_O)}{a_C m_C + \ldots + a_{Er} m_{Er} + (2a_C + 2a_O) m_H} = 3 \times 10^{22} cm^{-3}, \tag{4.1}$$

where $a_C = 49.8$, $a_O = 36.7$ and so on from table 4.1, and m_C, *etc* are the atomic masses of each element. This means that for a $1nm$ thick contaminant layer and an effective proton source area of $\pi(100\mu m)^2$ [30] the total number of protons available before depletion is about 10^{12}.

To place where this contaminant layer would be plotted on figure 2.1 from M. Foord's analysis [20], the ratio of hydrogen to the carbon equivalent mass of the remaining elements was estimated. Neglecting the presence of the erbium, the remaining atoms are similar in mass to carbon. Taking the total mass of each of those elements according to the stoichiometry of table 4.1 divided by the mass of carbon one gets a representative carbon atom for every 1.7 hydrogen atoms ($CH_{1.7}$).

The density of ErH_3 is $7.6 g/cc$. This means a proton density of $8.1 \times 10^{22} cm^{-3}$. In the $200nm$ thick layer with the same effective area as the proton source as the contaminant layer, there are 5×10^{14} protons available. With the necessary number of protons needed for fast ignition being 3×10^{16} [17, 48, 49], the target thickness would have to be a minimum of $12\mu m$ for the same effective area and assuming every hydrogen atom in that area is accelerated in forward.

4.1.2 ETCHER SYSTEM

The ion flow off of the rear surface is laminar [30]. Because of this, unless the $5nm$ of contaminants and oxides are completely burned off during the shot, hydrogen from the erbium hydride would never be seen. So to observe the affect erbium hydride has on the conversion efficiency, it was absolutely necessary to implement a system for removing the contaminant layer. The method chosen was an argon-ion sputtering gun used to etch the target surface. The CommonWealth argon-ion sputtering gun was the same used in the thesis work by M. Allen [50], demonstrating that 99% of the proton energy in beams measured originate from the target rear surface.

Operation of the argon-ion etcher required first achieving a vacuum base pressure of about $9 \times 10^{-5} torr$, and then leaking argon gas through the etcher head to raise the chamber pressure to $2 \times 10^{-4} torr$. A lower base pressure is desirable, but in the interest of time was not practical. For both the Callisto and Titan target chambers it takes nearly an hour of pumping to achieve $9 \times 10^{-5} torr$ and is nearly asymptotic at this point. Because it was necessary to vent the chamber after each shot to collect film and replace the target, longer pump down times would have reduced the number of shots per day for a nearly insignificant lower pressure.

With the argon gas passing through the etcher head, a cathode wire ionizes the gas. A negatively charged grid a the front of the head accelerates and the argon ions in a $3cm$ diameter beam. Lastly, a neutralizer wire just outside the front of the head introduces electrons to make the argon beam charge neutral. The argon beam current used was about $10mA$. The etcher head itself was placed about $15cm$ behind the target. To prevent the beam from hitting the RCF pack behind the target, the etcher head was also inclined 45° for the Callisto run and inclined 40° for Titan. The etcher was activated about one minute before the shot and continued to operate as the laser was fired.

The rate the etcher removed atoms from the target surface was measured *in situ*. A sample of the gold foil with erbium hydride was placed in the target chamber and microscope glass slide was used to cover and protect a portion of the sample. The etcher was turned on and allowed to run for several minutes. Afterwards, the sample was removed from the target chamber and scanned using a microprofilometer. The microprofilometer is a a needle dragged across the samples surface. The scan can resolve step differences on the order of $5nm$. The etch rate measured by this procedure in both the Callisto and Titan target chambers was about $15nm/min$.

It is important to note that etch rate was the net rate at which the surfaces is excavated. As the etcher was running, water vapor and vacuum grease was constantly reattaching to the surface. The $15nm/min$ was the difference of particle being removed with the rate of particles adsorbing back. The result was that the contaminant layer could never be fully removed. No matter how long the etcher was allowed to

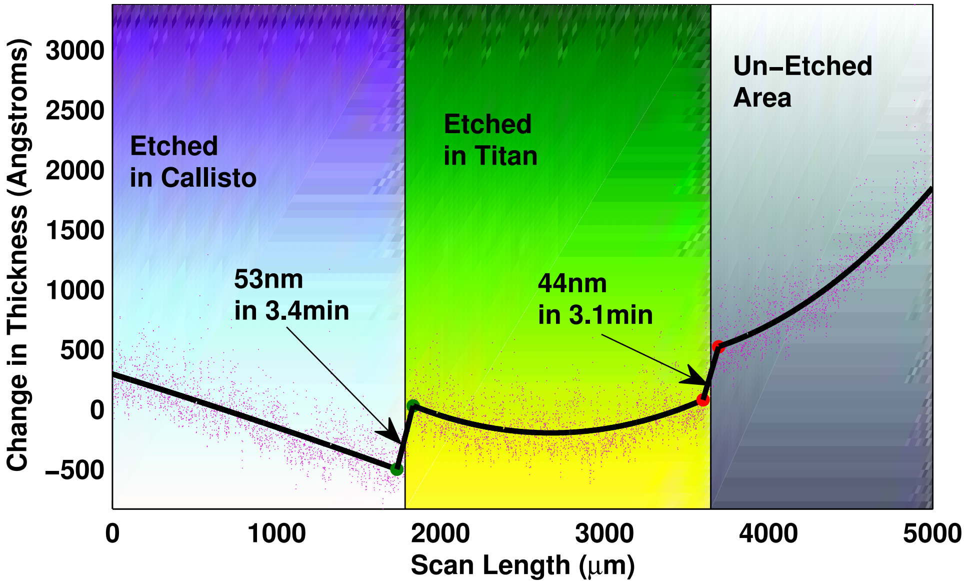

Figure 4.1: Microprofilometer scan of $Au - ErH_3$ after etching for 3.4 minutes with an argon-ion beam of about $10mA$. A glass slide was placed over half the sample so that a step could be measured in the profile. The rate of change in hydride thickness is about $15nm/min$.

run some ion signal from carbon or oxygen was always present. The rate at which a monolayer of water forms was possibly about a monolayer per microsecond.

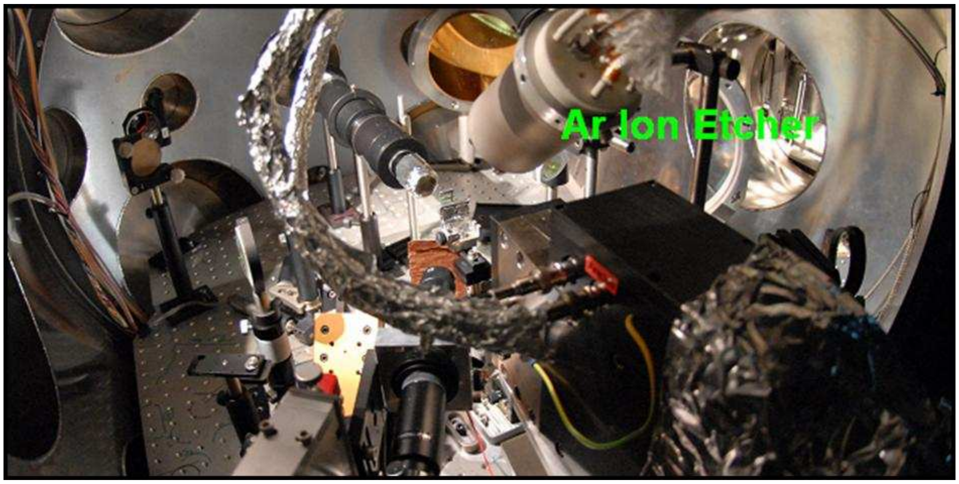

Figure 4.2: A picture taken inside the Callisto chamber with a view looking from behind the Thomson spectrometer. The argon-ion etcher can be seen above the Thomson.

This rate, however, is dependent on the vacuum pressure, the target temperature, and the reactivity of the target material. For example, a cleaned gold foil will regrow contaminants slower than aluminum as shown in the thesis work of M. Allen [50] (a review of adsorption of water is also covered). The surface concentration of a particular adsorbate with a vacuum pressure P is approximately give by,

$$n_s[molecules/cm^2] = 3.5 \times 10^{22} \frac{P[torr]}{\sqrt{m_{molecule} T}} \tau_0 e^{\Delta H_{ads}/RT}, \tag{4.2}$$

where m is the molecular mass of the adsorbate, R is the gas constant, T is the temperature in Kelvin, τ_0 is the vibrational period of the adsorbate ($\sim 10^{-12} s$), and ΔH_{ads} is the heat of adsorption. For gold, a target for which the etcher has been demonstrated to work effectively, $\Delta H_{ads} = 3kcal/mol$. At the other end, aluminum with $\Delta H_{ads} = 15kcal/mol$ was shown to be difficult to clean using the etcher system.

The irradiated foils cut from the samples were approximately $3mm \times 1mm$ in dimensions. To mount them in the chamber, they were glued to an aluminum bracket which allowed the side-on interferometer probe an obstruction free view of both the front and rear surface of the target. To know the degree to which the etcher heats the target a black-body emissivity measurement was made while etching for about 7 minutes. The temperature was about $200C$. This is important to know since at about $400C$ ErH_3 begins to boil off hydrogen and becomes ErH_2.

4.2 CALLISTO RUN

The first experiment conducted to observe the affect of erbium hydride was at the Callisto (formerly JanUSP) laser. Callisto is classified as a $40TW$ laser which places it a the lower end of today's state-of-the-art short-pulse lasers. A number of experiments exploring the physics of proton acceleration have been conducted with this system in the past [7, 11]. Proton beams typically produced by this laser have peak beam energies of about $10MeV$ with conversion efficiencies from laser to protons with an energy above $3MeV$ on the order of a tenth of a percent.

4.2.1 SET-UP

Callisto is a Ti:Saphhire, Chirped Pulse Amplification (CPA) laser system with a carrier wavelength of $800nm$. The FWHM pulse length is $200fs$. The system front end is a Spectra-Physics^{TM}Tsunami Ti:Saphhire oscillator. Pulses from this are chirped in a a 4-F diffraction grating stretcher. The pulse is then amplified by a regenerative amplifier and followed by a series of bow-tie configured multi-pass

65

Figure 4.3: An Autodesk^{TM}drawing of the Callisto chamber. Not shown are the swinging doors on either side.

amplifiers. Each amplifier uses a Ti:Saphhire crystal for the gain medium and are pumped by Nd:YAG lasers. A saturable absorber is also used after the regenerative amplifier to remove pre-pulse. The resulting output just before the main amplifier are $200mJ$ pulses with a repetition rate of $10Hz$. The main amplifier consists of large Ti:Sapphire disks which are pumped by more than $100J$ of frequency doubled laser light from the Janus laser. The chirp on the amplified pulse is removed under vacuum by a parallel diffraction grating compressor just before the beam is directed into the Callisto target chamber. The final beam energy is on the order of $10J$.

The targets were irradiated at an incident angle of 28° using an f/3 off-axis parabola to focus the beam. The peak intensity, I_{PEAK} for a diffraction limited focus at normal incidence would be,

$$\mathcal{E}_{laser}\left(2\pi\int_0^\infty\int_{-\infty}^\infty \exp\left(\frac{-4\ln(2)t^2}{\tau_{FWHM}^2}\right)\exp\left(\frac{-2r^2}{\omega_0^2}\right)dtrdr\right)^{-1}\approx 1.3\times 10^{21}W/cm^2, \tag{4.3}$$

for $\tau_{FWHM} = 200fs$ and $\omega_0 = 2(f/\#)\lambda/\pi \approx 1.5\mu m$. A diffraction limited beam is a high demand for a laser system. A measurement of the actual focal spot was made by imaging an attenuated beam with a microscope coupled to an 8-bit CCD camera. This method requires only running the low energy pump lasers as well as placing a series of neutral density filters in the beam path early up the laser chain. The lens on the microscope objective would otherwise damage with even microjoules of energy. The actual focal spot for a full system shot would be modified by a number of factors including B-Integral, which is an intensity dependant modulation of the phase. Because of thermal effects in the amplifiers, the phase can also vary from shot to shot. This makes knowing the actual peak intensity on every shot virtually impossible. However, an attenuated image of the focal spot provides more information than assuming a diffraction limited beam. The corresponding peak intensity from the images obtained was about $5 \times 10^{19} W/cm^2$.

Targets were positioned and aligned in the target chamber under vacuum. In the morning of each day, and sometimes in the afternoon as well, the position of the best laser focus was defined by imaging the focus with a microscope and then placing a $10 \mu m$ thick quad mesh grid at the point of best focus. Two imaging systems were used to define the mesh grid position, one viewing the target edge on and the other viewing the front surface from the angle of the specularly reflected light from the laser. The microscope was on a motorized mount and could be driven out of the way after it was no longer needed. Targets were mounted on an X-Y-Z motorized translation stage. Once the position of best focus was defined on the two imaging systems, the target was driven into the correct place. For rotation, the target was turned in place when mounted using the side-on imaging system to minimize the apparent thickness of the foil.

The diagnostics in the target chamber were placed at distances such that the signal on the detectors would avoid saturation. The RCF pack was located $2.5 cm$ behind the target, along the target normal axis. The Thomson spectrometer was also placed along the target normal axis, with the pinhole $14 cm$ away from the target. Ideally, the Thomson should have been placed further back, but the size of the vacuum chamber made this impossible. As a result, some of the proton date from the imaging plates appeared slightly saturated. Re-scanning the imaging plates one to two times was sufficient, however to recover a non-saturated data set. Figure 4.4 shows the layout of the principle diagnostics.

This experiment had the benefit of new diffraction gratings used for the beam compressor as well as a newly coated off-axis parabola. The final reflection off of the gratings in the compressor is the weakest link in a CPA system. With a relatively

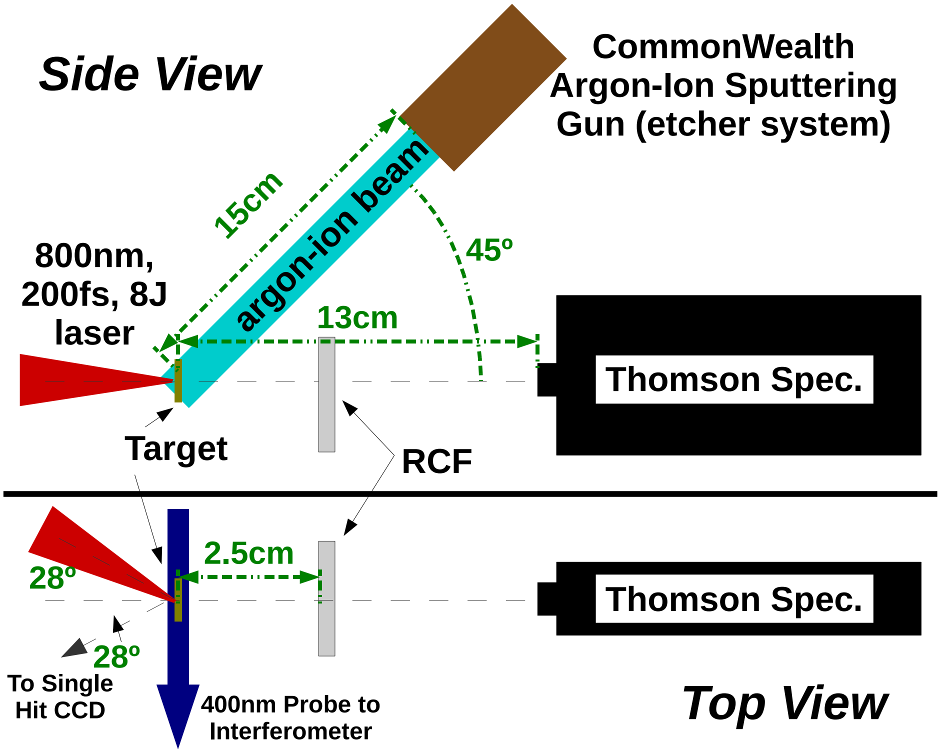

Figure 4.4: Diagram of the setup for the Callisto experiment; side-on view and top view.

low damage threshold compared with dielectric laser mirrors, the maximum energy of the laser is often designed to keep the intensity just low enough to avoid damaging the gratings for the largest beam diameter that is cost effective. Damage on the gratings can cause ineffective pulse compression as wells as disrupt the phase, causing a significantly reduced peak intensity due to poor focusing.

4.2.2 RESULTS

Figure 4.7 shows the dose on each layer of RCF from the film packs where the laser conditions were determined to be approximately the same by the Single Hit CCD, side-on interferometer, and laser energy meter. The laser energies varied between $6J$ and $8J$. In the final week of the experiment new damage spots on the diffraction gratings had been noticed which correlated with a drop in the proton beam energy and the disappearance of the x-ray signal on the Single Hit.

When analyzing the RCF, it was necessary to interpolate over the missing data. Each layer of film had a hole in the middle which allowed the Thomson to have a line of sight view to the target. The missing proton data on the film accounted for about 5% of the total dose on the first few layers of film. On the last few layers, it was as much as 30% of the beam, however, the total dose on those layers was only a couple of percent of the dose on the first layers of film. The edges of the proton beam were also cut off because of the need to lower the film pack slightly to allow clearance for the argon-ion etching beam. This also represented about 5% of the total dose on the effected pieces of film. Because the proton beam divergence decreases as the kinetic energy increases, only the first couple of layers were affected by this.

There were three specific observations from the RCF data. First, when the contaminants were etched from the gold, the overall proton energy was reduced to about 1% of the energy in the un-etched case. Second, gold with contaminants and gold

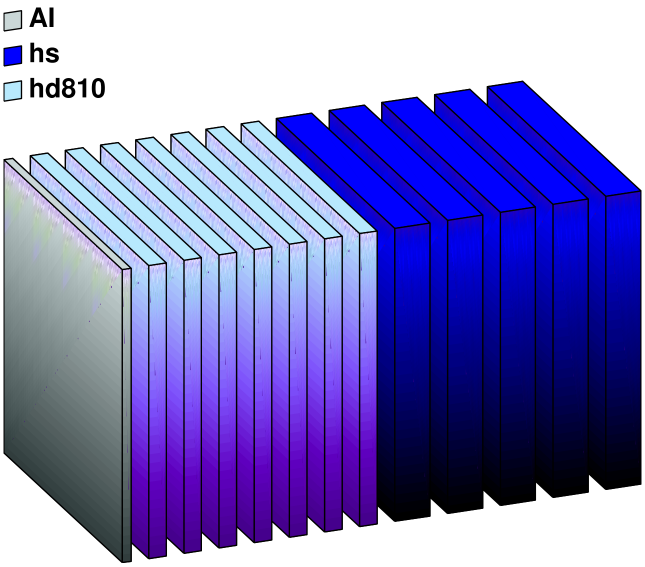

Figure 4.5: A typical RCF pack configuration for Callisto. The stack from the side facing the target to the back was $25\mu m$ Al foil, 7 layers of HD-810 (gel side forward), and 5 layers of HS. The 7^{th} layer of HD-810 was substituted with HS for some shots.

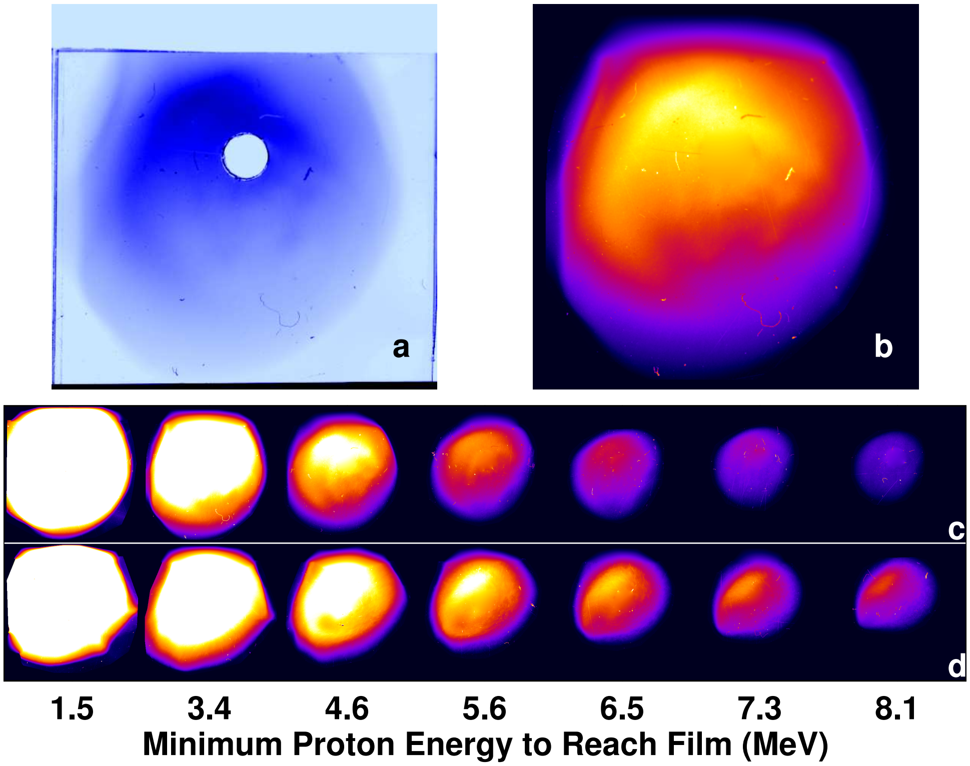

Figure 4.6: Sample RCF data from Callisto. Figure a) shows a false colored piece of film from a pack. Figure b) shows the same piece after converting the pixel values to dose and interpolating over the missing sections of the beam. Figures c) and d) show the dose converted images for two shots, gold with contaminants and gold with erbium hydride respectively.

with ErH_3 with contaminants had nearly identical proton energy spectra. Third, the overall proton beam energy was consistently higher in the case of gold with ErH_3 and no contaminants than in any other case.

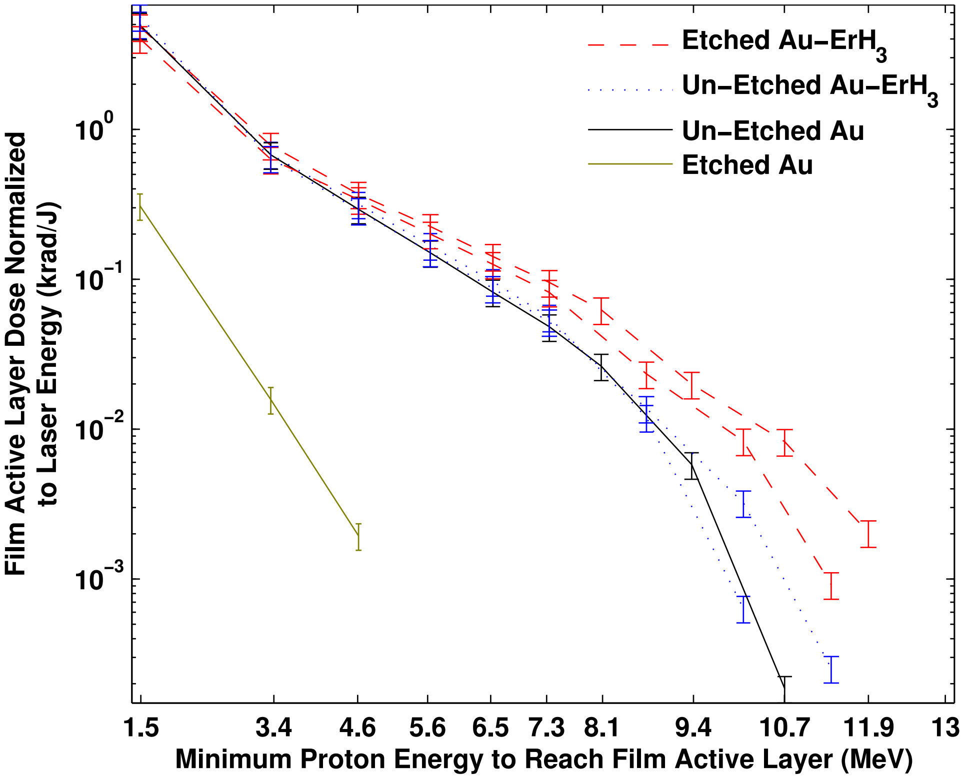

Figure 4.7: Proton dose per laser energy computed from RCF. Except in the case of the etched gold, each shot had a maximum proton energy of about 10 MeV. $Au{-}ErH_3$ produced the same proton beam as Au when un-etched. Etching $Au - ErH_3$ results in an increase in the proton signal.

The data showed a reasonable fit to the Maxwellian distribution shown in equation 3.4 in chapter 3. The proton temperature was typically around $kT_p = 1.6MeV$. The Total number of protons was about $N_0 = 5 \times 10^{10}$. The peak proton energy was about $\mathcal{E}_c = 10MeV$. When fitting the data, the first layer of film had to be ignored due to possible signal contamination from carbon ions. As such, the range of the data fit was valid for protons with kinetic energies above $3.4MeV$.

The conversion efficiencies from laser to protons for all the Callisto data were about one tenth of those typically obtained on higher peak power laser systems. The lower intensity available on Callisto compared with that of petawatt class lasers means a lower average electron temperature. The conversion efficiencies were consistent with other works and scaling laws [7, 11, 9]. For the case of targets with contaminants the conversion efficiency for protons above $3.4MeV$ was $0.12 \pm 0.006\%$. The deviation of 5% is the standard deviation from the three shots with contaminants presented in figure 4.7. For the case of erbium hydride with etching, the conversion efficiency was $0.15 \pm 0.016\%$. Thus, the case of erbium hydride showed a factor of 1.25 ± 0.19 improvement over protons originating from contaminants. Recall from chapter 2 that the improvement from simulation was about 1.37, but could be as low as 1.11 with the uncertainties in the degree of ionization of erbium and the relative abundance of hydrogen in the contaminants.

The x-ray background on the imaging plates made it impossible to view any ion signal from erbium using the Thomson spectrometer. As long as there were light weight ion's such as carbon and hydrogen, the efficiency of heavy ion acceleration remained low [31, 51]. Spectra from hydrogen and from carbon, on the other hand, were clearly visible. From the Thomson data, one was able to examine the effectiveness of the etching system as well as compare and contrast the relative abundance of ion species in the interesting cases outlined above.

Figure 4.8 shows Thomson spectra for three cases. On the left is gold with contaminants, the middle is gold with erbium hydride and contaminants, and the right is gold with erbium hydride after etching. Remarkably similar were the ion spectra for the two cases with contaminants, with or without erbium hydride. This further supports the argument that the erbium hydride buried beneath more than a nanometer of contaminants will have no influence on the physics of the ion acceleration which is happening at the outermost surface.

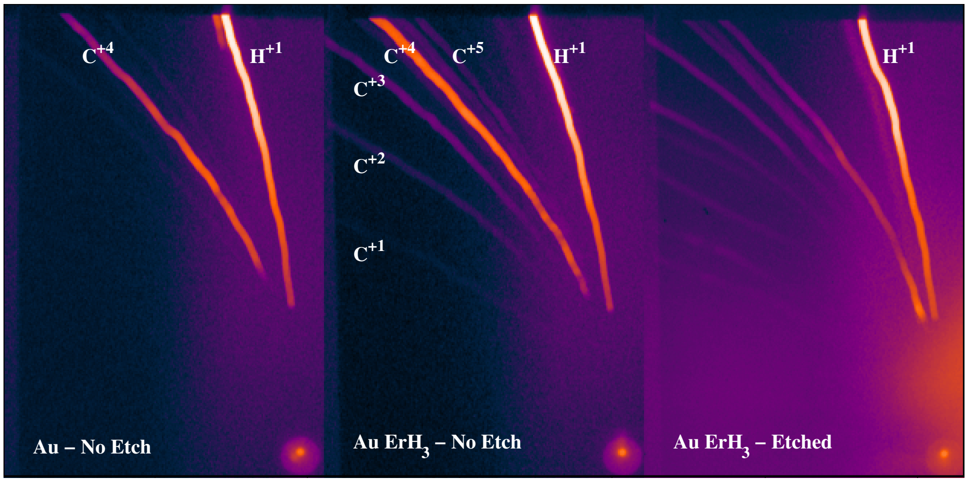

Figure 4.8: Thomson spectrometer data for typical gold foil shots in Callisto. Spectra for the un-etched cases of Au with contaminants and $Au - ErH_3$ with contaminants are similar. Etched $Au - ErH_3$ shows an overall decline of ion signal except that of protons.

Also of particular note is that the carbon ions appear enhanced at the +4 charge state. This enhancement is logical because of the dramatic increase in the ionization potential after +4. The ionization potentials of carbon have gradual increases for the first four sequential ionization states. The 5^{th} electron, however, is much more difficult to remove with an ionization potential that is an order of magnitude greater than the previous ionization state, as can be seen in appendix B.

Because of the imaging plates proximity to the etcher head in the target chamber, a bright blob of signal appears over the region near the neutral ion point on the detector. Despite that, two things are clearly observable in the case of etched erbium hydride targets. First is that the proton signal remained relatively unchanged compared with that of the contaminants. Second is that the carbon signal was significantly reduced. There was a slight increase of the appearance of +5 carbon which was probably due to collisional ionization from the argon ions in the etching beam. Because the proton signal remained high while the carbon signal decreased suggests that the overall adsorption of ions during the etching process was small compared to the removal rate of the etcher.

4.3 TITAN RUN

The second erbium hydride experiment was completed using the Titan laser system in the Jupiter Laser Facility at Lawrence Livermore National Laboratory. Five gold targets were irradiated in the time allotted. The beam time given on the Titan laser was essentially a bonus opportunity to study if the erbium hydride would continue to demonstrate improved proton beams with nearly 20 times the laser energy. The thickest targets available to shoot were $14 \mu m$ gold foils. There was concern shooting targets this thin since prior to this $14 \mu m$ to $15 \mu m$ was the low limit of target survivability against pre-pulse. Typical protons produced on the Titan laser have peak proton kinetic energies of about $50 MeV$ with a conversion efficiency of 2% to 3% from laser to protons above $3 MeV$.

4.3.1 SET-UP

Titan is a $150 J$ laser with a carrier wavelength of $1.053 \mu m$ and a pulse duration of $500 fs$. The laser uses an Optical Parametric Chirped Pulse Amplification (OPCPA) front-end in place of a regenerative amplifier like Callisto. This has the benefit of

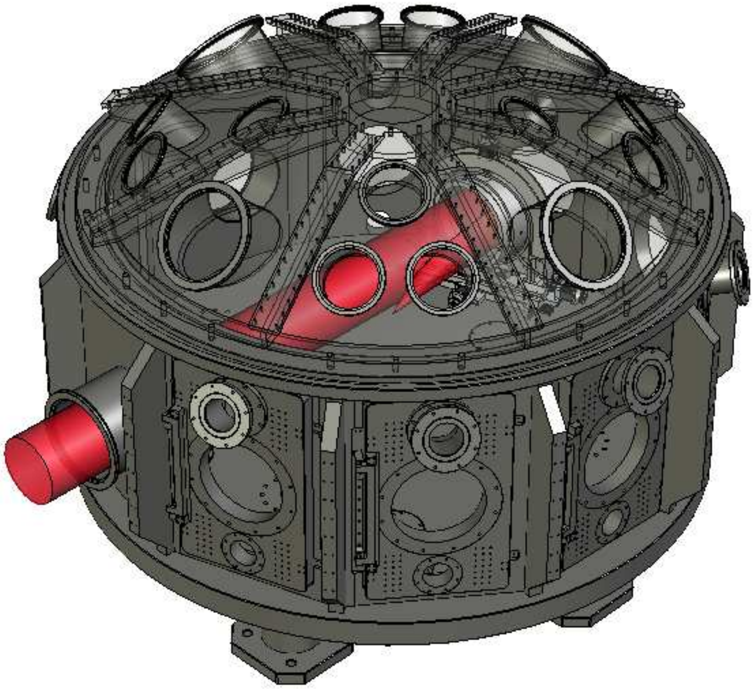

Figure 4.9: A Solidworks$^{\text{TM}}$drawing of the Titan chamber. The roof is shown in transparency to show the focusing optic in the chamber.

lower pre-pulse levels due to amplification of spontaneous emission. The output of the OPCPA undergoes further amplification from a series of Nd:Glass, flashlamp pumped amplifier rods and disks.

The diagnostic arrangement for this experiment was similar to that of the Callisto setup. With 20 times the laser energy, each diagnostic was placed at greater distances from the target to avoid saturation. The RCF pack was placed $6.5cm$ behind the plane of the target, along the target normal axis. The Thomson spectrometer was also placed along the target normal axis with a distance of $36.7cm$ from target to pinhole. This was as far back as the Thomson spectrometer could be placed allowing room for a new diagnostic to measure the electron T-hot distribution that had been placed behind the Thomson [52]. A hole had also been put into the imaging plate along the neutral particle trajectory so that this diagnostic would have a clear line of sight through the Thomson.

The procedure for target alignment differed from that of the Callisto experiment. Rather than positioning the foil under vacuum, an alignment jig setup outside the chamber using high magnification ($> 20\times$), large working distance ($1inch$), three microscope imaging system defined the X-Y-Z alignment of the target. The jig used magnetic kinematic mounts so that the aligned target could be taken off of the jig and placed into the chamber. This greatly speed up the daily shot rate because the next target could be aligned while still pumping the vacuum chamber to its base pressure.

The focusing optic in the Titan target chamber was an f/3 off axis parabola. The laser spot-size at tight focus was similar to that of the Callisto experiment. Because the pulse length was nearly double that of Callisto and the energy nearly 20 times, the peak intensity was about 10 times that of Callisto. The estimated peak was about $3 \times 10^{20} W/cm^2$. A known issue at the time of this experiment, however, was that thermal effects on the index of refraction in the Nd:Glass amplifiers caused significant shot to shot variation on the focal spot-size.

Additionally, like any short-pulse laser system, the level of pre-pulse also varied shot to shot. At the time of this experiment, no direct method had been implemented to monitor this.

4.3.2 RESULTS

With only five laser shots, it is hard to make any conclusions about the results from the Titan data. To be able to say anything, more data is needed. None the less, improvements in the proton conversion efficiency were observed as is shown below.

The RCF data showed a reasonable fit to the Maxwellian-Boltzmann like piece-wise defined distribution in equation 3.4. A sample fit to data collected in Titan is presented in figure 3.5. When fitting the data, the 7^{th} film layer was saturated and was excluded from the data set. This was the first occurrence of MD-v2-55, which has an increased sensitivity over HD-810.

Had only three targets been irradiated; namely, etched gold, gold with contaminants, and etched gold with erbium hydride, the data would suggest a similar result to what was observed in Callisto. For these three shots, the etched gold had about 1% of the proton beam energy seen in the un-etched gold case. The addition of erbium hydride with the contaminant layer removed showed a conversion efficiency from laser energy that *1.36* times that gold with contaminants. Recall once again, that the LSP simulations produced a factor of 1.37.

The two remaining targets produced results which have forced me to rethink what mechanism was at play. Figure 4.11 shows the RCF data for each of the five shots normalized by the laser energy. The solid gold and blue curves as well as the dashed red curve are the results mentioned in the previous paragraph. The solid black curve

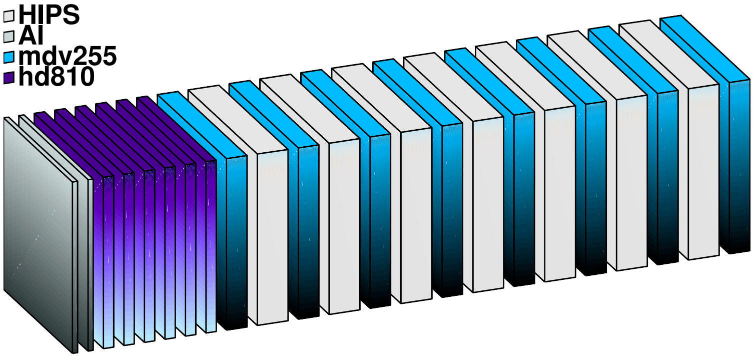

Figure 4.10: A typical RCF pack configuration for Titan. The stack from the side facing the target to the back was 2 layers of $25\mu m$ Al foil, 6 layers of HD-810 (plastic side forward), and an alternating series of MD-v2-55 and $1.5mm$ thick high impact polystyrene filters repeating 8 times.

Target	**Cleaned Using Etcher (yes/no)**	**Number of Protons**[a] **($\times 10^{12}$)**	**Conversion Efficiency**[a]	**Laser Energy (J)**
$Au - ErH_3$	Yes	4.2	3.4%	129
$Au - ErH_3$	No	5.6	5.7%	143
Au	No	3.0	2.5%	137
Au	Pre-Etched[b]	3.5	3.3%	149
Au	Yes	0.6	0.33%	136

[a] Counting only protons above $3MeV$

[b] Etched for $1min$ then allowed to recombine for $15min$

Table 4.2: Titan RCF results for the gold data set.

is a curious, but incomprehensible shot. This was a gold foil that had been etched for about one minute about fifteen minutes before the laser was fired. In the time after the etcher was operated, a fresh layer of contaminants formed on the surface which was not quantified. At the time of the shot, the etcher was not activated. The interesting observation was that the proton spectrum for this case appeared to be similar to the etched erbium hydride.

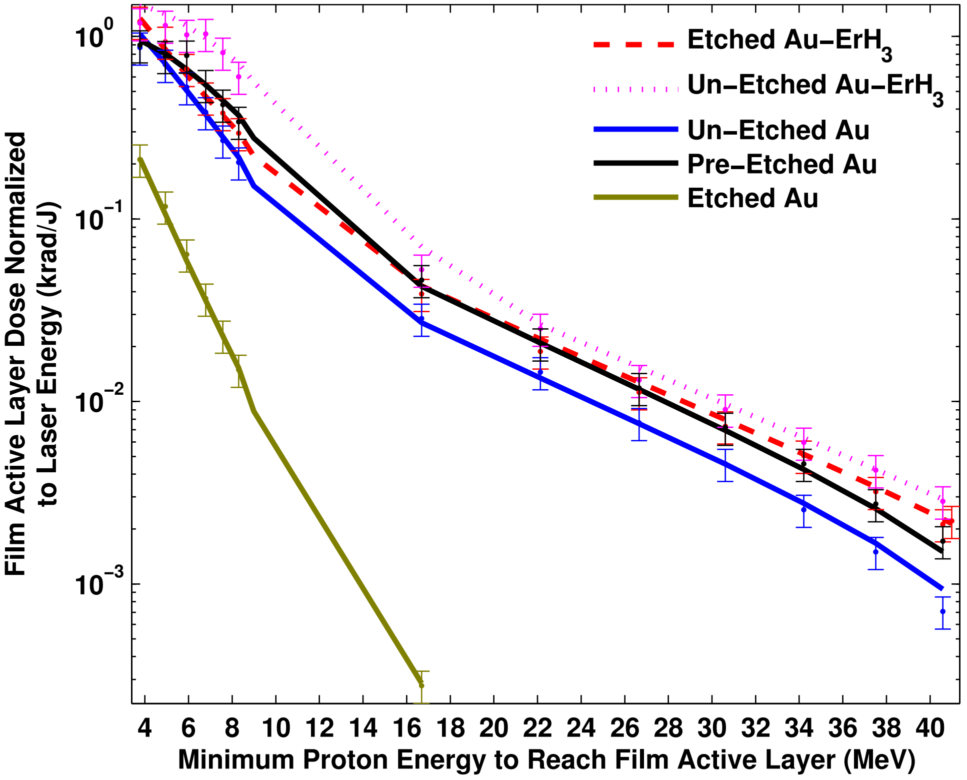

Figure 4.11: Proton dose per laser energy computed from RCF. The $Au - ErH_3$ target produced more energetic proton beams than Au, etched and un-etched.

The dotted magenta data was a gold target with erbium hydride that was *NOT* etched. If the behavior were to be consistent with the Callisto experiment, one would expect the dose on the film to be the same as the un-etched gold. Instead, a proton conversion efficiency that was nearly *5.6%* for protons above $3MeV$, was observed. This was more than double that of protons originating from a contaminant layer.

The single hit and interferometer data for these shots do not reveal anything that might suggest a change in laser conditions which could account for the difference. The self-emission in the vicinity of the laser plasma obscures much of the probe light on the interferograms, but the fringes that are visible due not appear significantly different. A change in pre-plasma scale length at the front surface would have been an indication of a change in pre-pulse conditions.

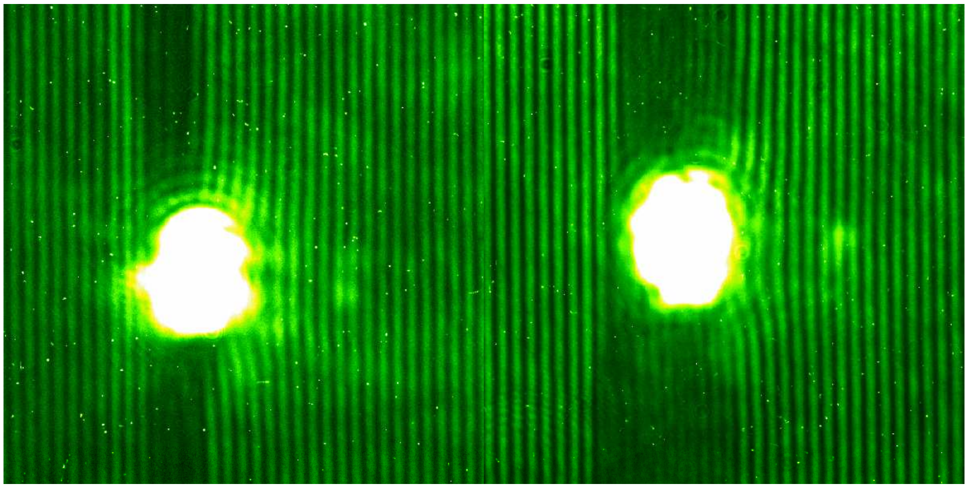

(a) Au With Contaminants (b) $Au - ErH_3$ With Contaminants

Figure 4.12: Interferograms for gold with and without ErH_3 and no etching. Self-emission was high, but the fringes that are visible are not significantly different.

The total x-ray emission from the gold was also similar for each of the five shots. Figure 4.13 shows the single event histogram minus the background versus pixel value for all five shots. The inverted curve is from a copper foil shot for a photon energy calibration. Integrating the total number of counts from each peak, the difference between each shot is only a couple of percent. This would suggest that the energy absorbed from the laser by the hot electrons was at least consistent in each shot.

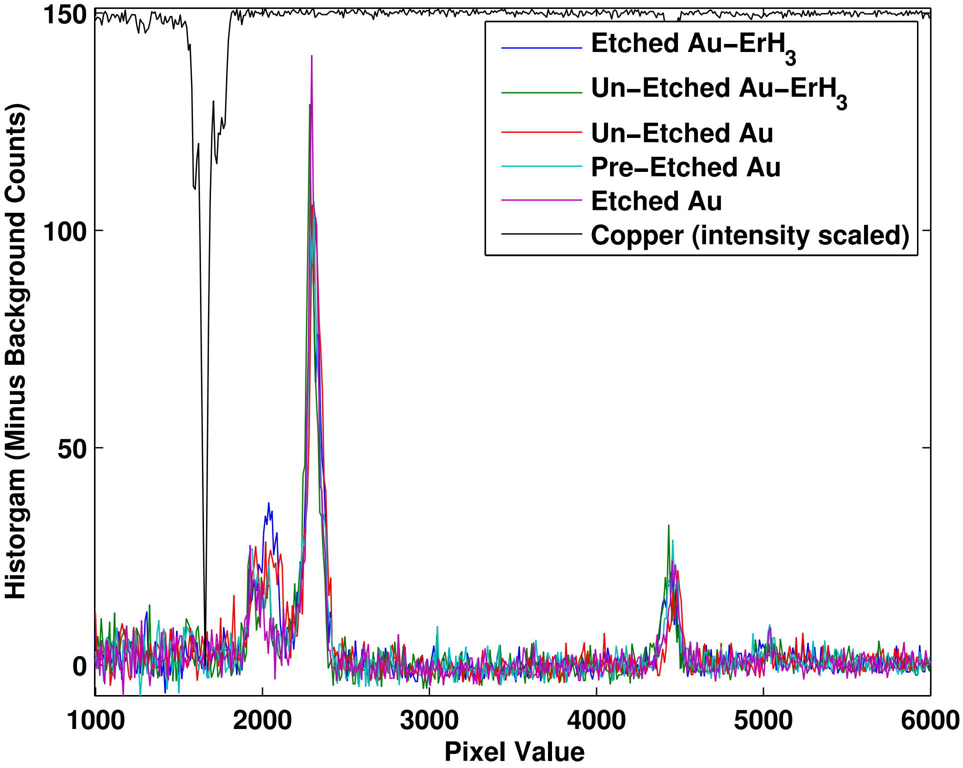

Figure 4.13: The single hit histograms of single event counting minus the background from all five shots in Titan. A sixth histogram from copper is also plotted for comparison of the x-axis against the known $Cu - K_\alpha$ photon energies.

In an experiment conducted by D. Hey [25], the conversion efficiency versus the thickness of the target was explored using the Titan laser. A good agreement with an inversely proportional scaling to the target thickness was demonstrated which was reinforced by LSP simulations. However, once the target thicknesses became less than or equal to about $15\mu m$, the conversion efficiency reached a plateau at about 2.5%. One possibility for the breakdown of the thickness scaling was suggested to be due to a shock breakout from the pre-pulse creating a plasma scale-length on the rear surface. However, this was dismissed as being unlikely since the peak proton energy did not change significantly. The peak proton energy should fall off as the plasma scale length increases [11].

A second plausible argument was that the protons from the contaminant layer were being depleted. From the estimates on the proton density, for a $200\mu m$ diameter proton source, there would only be about 10^{12} protons available before the layer was depleted (refer to the contaminant analysis in section 4.1.1). From table 4.2 counting only protons with a kinetic energy greater than $3MeV$ there are about 4×10^{12} protons on the film pack. The case of un-etched gold from this experiment showed a 2.5% conversion efficiency, consistent with D. Hey's result. With the addition of the thicker hydride layer depletion could only occur if 10^{14} protons were being accelerated. Though this is not a conclusive argument, it would be curious to see what would happen if thinner targets were used where the thickness scaling would predict even more protons.

One particularly useful target irradiated in Titan was that of the etched gold foil. By removing the contaminants from the back surface of the gold, the over all proton conversion efficiency was reduced to about 1% of that of the un-etched case. This is consistent with the work of M. Allen [7], demonstrating the rear surface mechanism as the dominant means of accelerating ions. Figures 4.14 and 4.15 show the raw film data for un-etched and etched gold respectively. In addition to an obviously lower dose on the film, the beam diameter also appears smaller in the etched case as well as having a lower peak proton kinetic energy ($< 22MeV$).

What was most interesting about this shot was that with the light elements gone, the heavier gold ions were efficiently accelerated. A one centimeter burn was visible on the front surface aluminum foil protecting the film pack which was $6.5cm$ behind

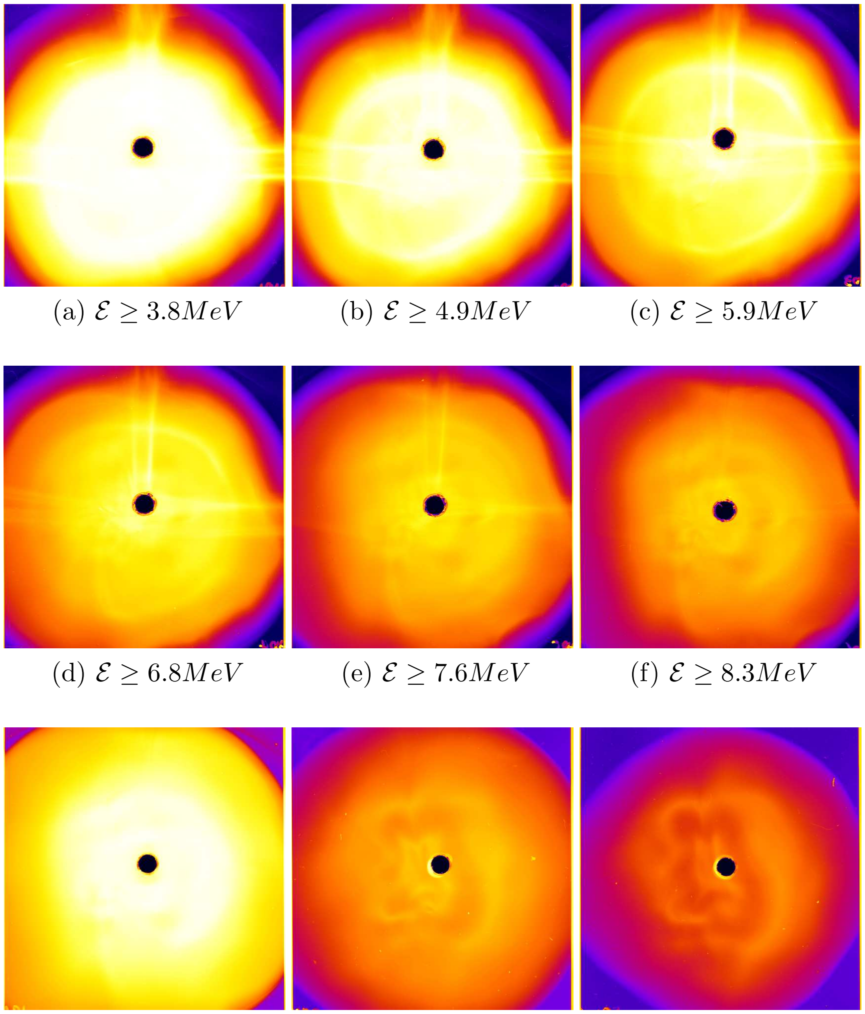

(a) $\mathcal{E} \geq 3.8MeV$ (b) $\mathcal{E} \geq 4.9MeV$ (c) $\mathcal{E} \geq 5.9MeV$

(d) $\mathcal{E} \geq 6.8MeV$ (e) $\mathcal{E} \geq 7.6MeV$ (f) $\mathcal{E} \geq 8.3MeV$

(g) $\mathcal{E} \geq 9.0MeV$ (h) $\mathcal{E} \geq 16.7MeV$ (i) $\mathcal{E} \geq 22.1MeV$

Figure 4.14: The first 9 layers of RCF raw data showing a proton beam from an un-etched gold foil target on Titan.

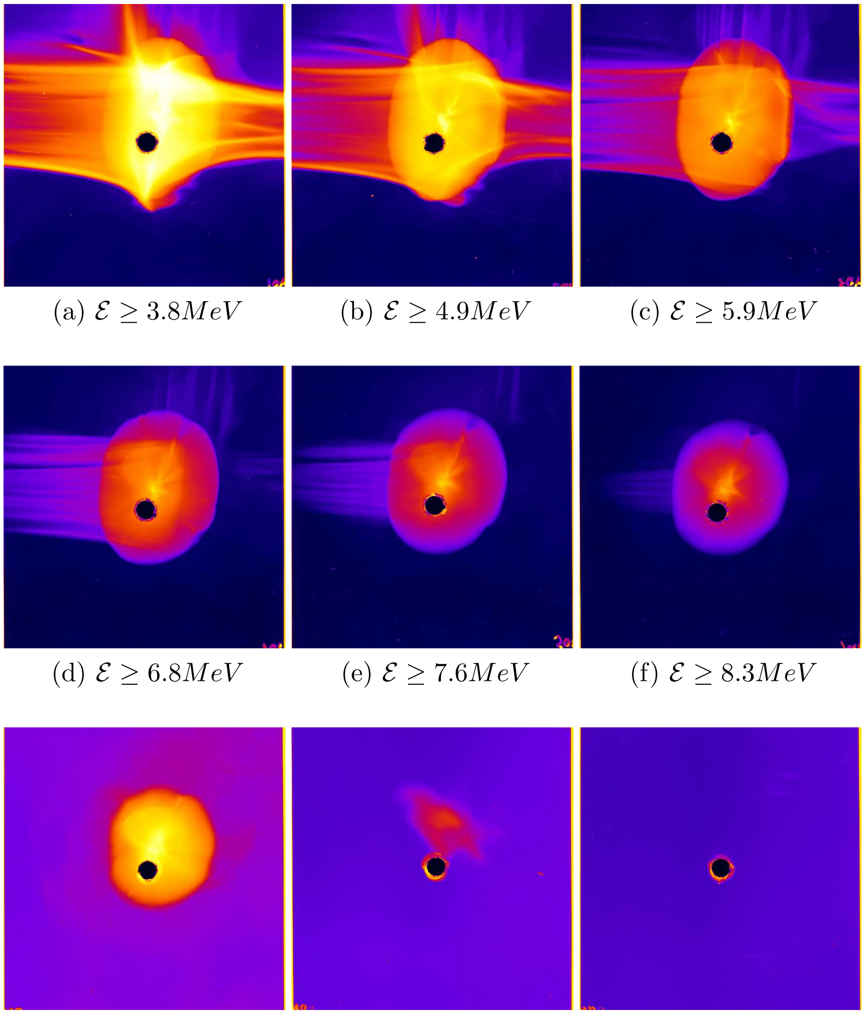

(a) $\mathcal{E} \geq 3.8MeV$ (b) $\mathcal{E} \geq 4.9MeV$ (c) $\mathcal{E} \geq 5.9MeV$

(d) $\mathcal{E} \geq 6.8MeV$ (e) $\mathcal{E} \geq 7.6MeV$ (f) $\mathcal{E} \geq 8.3MeV$

(g) $\mathcal{E} \geq 9.0MeV$ (h) $\mathcal{E} \geq 16.7MeV$ (i) $\mathcal{E} \geq 22.1MeV$

Figure 4.15: RCF raw data showing a proton beam from an etched gold foil target on Titan.

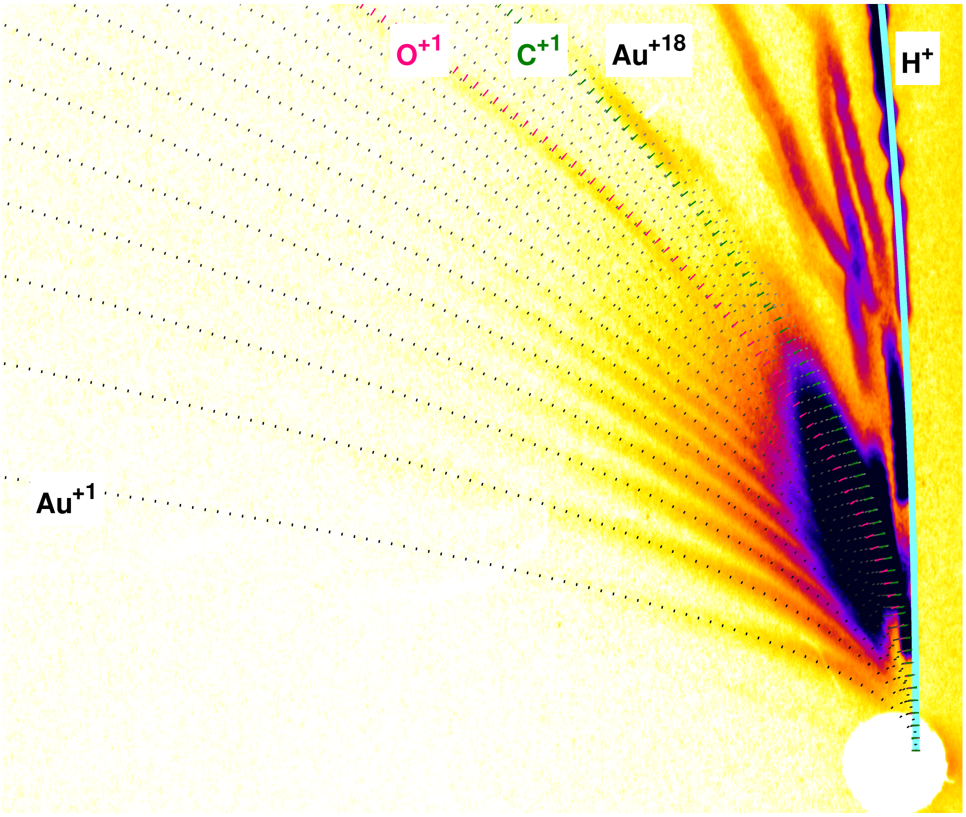

Figure 4.16: Etched gold foil in Titan. With the contaminants removed, gold ions were efficiently accelerated to several MeV. Gold was ionized up to the 18th charge state.

the target. The ion spectra from gold ions were also, for the first time in the experiment, visible above the background on the Thomson. Regrettably, the signal was even saturated beyond recovery. Figure 4.16 shows the data with dotted curves representing the calculated position for where the respective ion traces should appear. The tracks begin to smear together at the higher ionization values for gold, but it does seem that Au^{+18} was produced. The abundance of gold ions from +1 to +18 were about the same for each. The average value of the charge state of gold would have, therefore, been about +9. Recall again that from the simulation, Er^{+10} was assumed. Comparison of the ionization rates for erbium and gold suggest the charge state should be the similar for both for charges less than +18.

4.3.3 ENCLOSED GEOMETRIES (CONES)

One additional challenge that proton fast ignition must deal with is the inclosing cone structure which will protect the hemispherical shell from the plasma blow-off of the compressed fuel capsule. Figure 4.17 shows the RCF from a curved film pack which viewed protons emitted from the tip of a cone target as well as off of the edges. The cone was a witches hat shape with a flat tip having a $20\mu m$ diameter. The cone opening was a 30° full angle. The film pack was about $12cm$ long and $5cm$ wide. It was given a $5cm$ radius of curvature bending inward. The pack was positioned so that each point along the center line of the film was $5cm$ away from the cone. The total viewing angle was about 12° below the cone tip axis and wrapping upward to about 130° over the top of the cone. There was no hemispherical foil in the cone, rather the aim was to put the laser directly into cone opening and observe the hot electron distribution using the x-ray imaging diagnostics. What was observed on the proton pack was a circular beam from the tip of the cone, but also observed was a very bright proton beam off of the cone wall. Protons from the wall may be less bright were there a hemisphere located further away from the tip, resulting in less laser light directly incident on the cone wall near the tip. Energy loss due to ions from surfaces other than the spherical foil will likely be a concern for fast ignition. Another concern is that the cone on the laser side of the hemisphere will fill up with plasma from the pre-pulse pre-heating [53].

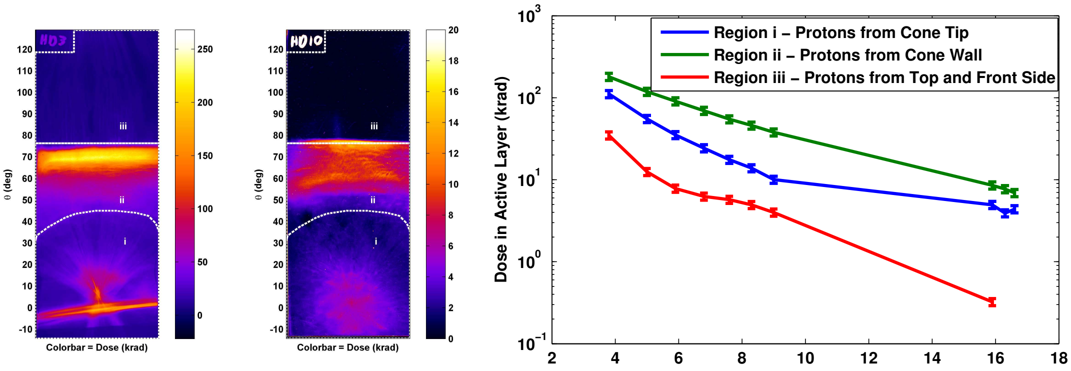

(a) $\mathcal{E} \geq 5.9MeV$ (b) $\mathcal{E} \geq 16.6MeV$ (c) Doses From Each Region

Figure 4.17: RCF from a curved film pack positioned over a copper cone target. The pack was given a $5cm$ radius of curvature. It was positioned over the target so that the tip of the cone pointed at a spot $12mm$ above one end of the pack and every point on the pack was $5cm$ from the target. The total collection angle along the length of the pack was about 120°.

A second target configuration was also explored using a hole in a washer to inclose a hemispherical foil. A copper mesh grid was positioned outside of the foil so that the size of the proton focus could be measured by counting the number of mesh elements visible on the RCF. A proton beam originating from the mesh was observed. However, A second beam was also seen, likely coming from the washer surface. This was likely a problem due to a slight misalignment of the laser. This is an example of how the conversion efficiency to *useful* protons might be affected by unwanted ion acceleration.

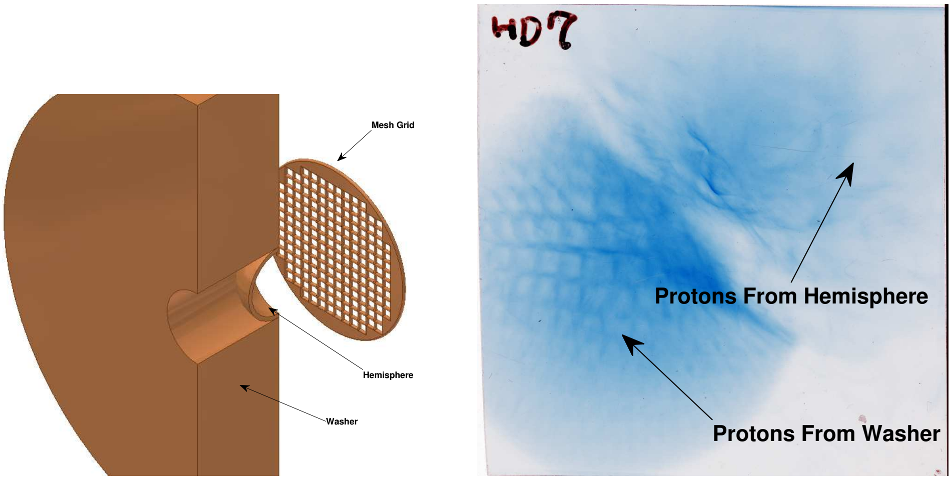

(a) Cartoon of Target (b) RCF

Figure 4.18: A hemisphere target in a washer with a mesh-grid in the proton beam path (*NOT* drawn to scale). The RCF shows two distinct proton sources, one originating from the spherical surface and the other from the flat edge of the washer.

4.3.4 RIPPLED TARGETS

Lastly, shots onto $25\mu m$ thick copper targets which featured ripples on the back surface were conducted to measure the size of the proton emission on the foil. One property of sheath field accelerated protons is that they carry with them surface features of the target. The ripple spacing was $3\mu m$ from peak to peak. Because of the high dose as well as smearing from magnetic fields, the first few layers of film dominated by low energy proton signal did not have resolvable ripples. The higher energy layers of film, on the other hand did. For proton kinetic energies above $34.5MeV$ a size diameter of the proton source area on the foil was estimated to be about $125\mu m$. The beam on the RCF filled a diameter of about $6cm$ which was $6.5cm$ behind the target. The imaging of the ripples is because the protons act like a virtual point source somewhere out in space in front of the target. Solving the simple trigonometry puts the position of the virtual source about $115\mu m$ in front of the target.

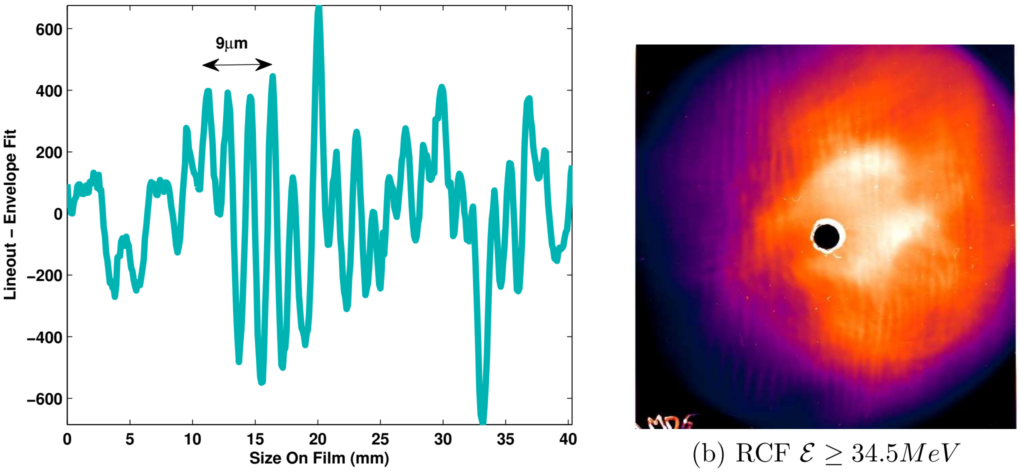

(a) Line Out

(b) RCF $\mathcal{E} \geq 34.5MeV$

Figure 4.19: RCF data from a $25\mu m$ thick Cu with ripples on the back. The ripples were spaced $3\mu m$ apart. The corresponding beam diameter on film implies a $125\mu m$ diameter source size on the foil.

CHAPTER 5

CONCLUSIONS

The number one challenge to overcome for proton fast ignition is to improve the conversion efficiency from the laser energy. The current designs call for 15% of the laser energy to be converted to a proton beam with a characteristic temperature of about $3MeV$ to $5MeV$. To date, conversion efficiencies around 5% represent the state-of-the-art in Petawatt class short-pulse laser experiments involving thin foils.

From simulations and estimations using simple models, heavy hydride coated targets have been suggested as a possible means to increase the conversion efficiency to protons by decreasing the fraction of the total ion beam energy which partitions to non hydrogen atoms. Early simulations on the hybrid pic code, LSP, even suggested ErH_3 could double the conversion efficiency relative to protons owing their origin to hydrocarbon contaminants.

Additional LSP simulations performed to be more consistent with data from ion beams produced in my thesis work lower the expected improvement to a factor of 1.3. In these new simulations, the most significant difference was in the assumed degree of ionization of the carbon atoms in the contaminant layer. In the previous work which observed the factor of two, carbon was taken to be fully ionized. In my experiments, carbon was found to be ionized up to +4 and because of the step change in the ionization potential beyond that, the distribution was almost entirely denominated by +4. This lower ionization state means that less energy partitions into the carbon than it would in the fully ionized case. Thus, the proton conversion efficiency from contaminants was better than predicted by early works and when compared with ErH_3, the erbium hydride was found to have less of a gain.

5.1 AFFECT OF HYDRIDES WITH CALLISTO

The goal of the Callisto experiment was to observe the change in conversion efficiency using erbium hydride versus contaminants. The experiment did observe an improvement when using erbium hydride. The ratio of the proton conversion efficiency for protons greater than $3MeV$ from erbium hydride to those from contaminants was 1.25 ± 0.19. This was fully consistent with the LSP simulated results.

The biggest uncertainty in the experiment was knowing whether or not the contaminant layer was being successfully removed from the erbium hydride's surface. Without removing the contaminant layer, no direct comparison can be made between ErH_3 and hydrocarbons since the TNSA mechanism is a surface phenomenon. From the analysis of the Thomson spectrometer data combined with the direct measurement of the change in target thickness as a result of the argon-ion etching system used to remove the contaminants, it is likely that most of the contaminant layer was removed while a small percentage of the surface did recombine with vacuum grease and water in the target chamber.

The Thomson spectrometer data for any target, with or without erbium hydride, revealed no significant differences in the ion spectra as long as the etcher was not used. When the etcher was used on gold, the overall ion signal from all species disappeared. When the etcher was used on targets with erbium hydride, the carbon signal was was degraded while the proton signal remained strong. The carbon signal was stronger in the case of etched erbium hydride relative to etched gold. This says that the adsorption rate at the erbium surface is greater than gold. However, the adsorption did not appear to be so strong that erbium hydride could not be cleaned.

5.2 AFFECT OF HYDRIDES WITH TITAN

In the Titan experiment, there was no opportunity to repeat any of the shot configuration. As a result, there are no reliable statistics to suggest the exact amount or cause of the observed improvements in the conversion efficiency. Targets with erbium hydride did show an improvement over contaminants, none the less. As before, etched gold saw a reduced ion signal of all species. The proton conversion efficiency was about 1% the energy of all other cases. The $14\mu m$ gold foil with contaminants had an efficiency of 2.5% which is consistent with all other experiments conducted on this laser system, with gold targets of the same thickness. Etched erbium hydride showed a factor of 1.36 times that, which at first glance would seem consistent with the Callisto data as well as the LSP simulations. However, the next shot was a foil with erbium hydride, but with the contaminants left on the target. Here, the conversion efficiency was more than twice that of the gold with contaminants!

A surface analysis of the contaminant layer suggests that it has about 10^{12} protons to accelerate for typical proton source sizes. The proton spectra observed by the RCF for every shot, not counting the etched gold, had about 5×10^{12} protons counting only those with a kinetic energy above $3MeV$. The most likely explanation for the observed differences in conversion efficiency was because of depletion of hydrogen in the case without erbium hydride. More data is needed to make an real conclusions, however. Though, if the 5.6% conversion efficiency that was observed was due to a depletion issue then the one over the target thickness scaling in the efficiency might result in the 15% needed by shooting $5\mu m$ thick targets with the $200nm$ thick hydride coating.

The Thomson data from the Titan experiment was useful and exciting for the one shot with the cleaned gold. It was exciting because with the contaminants removed, the only thing left to accelerate was gold itself. And sure enough gold was accelerated with high enough efficiency to saturated the imaging plates in the Thomson spectrometer and put a $1cm$ diameter burn mark on the aluminum foil protecting the film pack. By counting the number of charge states observed in the gold and comparing with the ionization potentials of erbium, the average charge state of erbium was estimated to be about +9 or +10 with a maximum at about +18.

5.3 IMPLICATIONS FOR FAST IGNITION

Coatings of ErH_3 clearly have advantages over contaminant layers which are closely approximated by $CH_{1.7}$. At the energy scale of these two experiments the heavy hydride outperformed the hydrocarbons by a factor of 1.25 or better. For Titan, the real advantage seemed to be the abundance of hydrogen in the hydride relative to the contaminant layer. The real question is how will ErH_3 stand against a thick plastic coating of CH_2. In both of these targets the number density of hydrogen is about the same. The erbium is about 10 times more massive than the carbon, which means the mass scaling for the proton conversion efficiency favors ErH_3 for a better proton beam. However, the fraction of beam energy partitioned to they hydrogen decreases as the charge state of the hydride increases. Erbium can ionize to much higher charge states than carbon, as carbon only has six electrons to lose. Fast ignition scale lasers will deliver about one hundred kilojoules of energy which is about ten thousand times the energy in the Callisto experiment. It is possible that the corresponding sheath field will be strong enough to ionize the erbium to a point where CH_2 produces much better proton beams. It will be interesting to follow the scaling of proton experiments as short pulse facilities reaching these energies start to come online.

5.4 CLOSING REMARKS

The small improvement made in the proton conversion efficiency observed in this work by itself is not enough to achieve the requirements of fast ignition. That isn't to say that other acceleration mechanisms don't exist which may work. Even if proton fast ignition does ultimately prove to be impossible, other applications for what we achieve are out there. Proton beams have demonstrated success in the treatment of cancer. So if protons are unable to rise to the call of clean burning energy, they are already there to help the sick.

APPENDIX A

CODE WRITEN FOR ANALYSIS

All of the analysis for this work was completed using MATLAB®. The following are excerpts of the functions and script files that were written. The programming language of MATLAB®is a high level language which is command line and function oriented. The core environment is matrix array operations oriented; hence the name *MAT* rix *LAB* oratory.

A.1 RADIOCHROMIC FILM

The following is the code written for analyzing RCF packs.

A.1.1 PROCESSING FILM

Two analyze the large volume of film, it was useful to write a graphical user interface (GUI) that could load every layer of film from a pack and perform the needed steps. The procedure after inputting the image files into the program was,

1. subtract the fog level on each layer of film,
2. convert the pixel values to dose,
3. subtract background from due to electrons, etc.,

4. call the program to fit $dN/d\mathcal{E}$,

5. and save all the working data with the raw data in a single file.

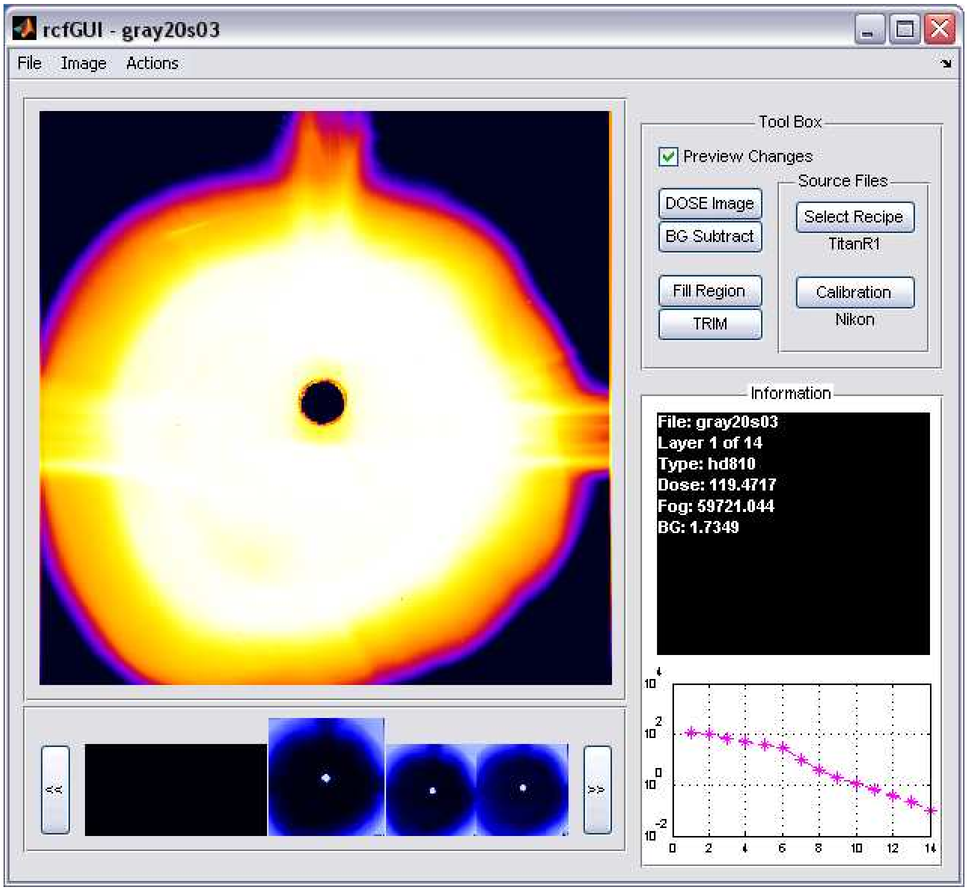

☑ Preview Changes

Select Recipe: TitanR1

Calibration: Nikon

File: gray20s03
Layer 1 of 14
Type: hd810
Dose: 119.4717
Fog: 59721.044
BG: 1.7349

Figure A.1: A screen-shot of the RCF GUI written to analyze the radiochromic film from packs.

A.1.2 FILM PACK RESPONSE

The computationally intensive part of the analysis was integrating the stopping powers for each layer in the film pack. So it was best to do this once and then create a recipe file that could be linked to each film pack constructed according to that recipe. To generate the recipe file wrote two programs were written. The front end program that was actually called was a command line function where one could input the pack configuration using two letter symbols for each layer type and the energy range as a vector. The energy vector in MATLAB®is called as `E=1:(29/1999):30;`. This would create a vector E with 2000 energy points, evenly spaced between $1MeV$ and $30MeV$. The variable pack might be `pack={'Al25','DH','DH','M2'}`, which would be a film pack of $25\mu m$ of aluminum followed by two layers of HD-810 (plastic side forward) and a layer of MD-v2-55. Possible values for inputs to the pack are given in table A.1.

Code	**Description**
`'HD'`	HD-810 film with the gel side facing the target
`'DH'`	HD-810 film with the plastic side facing the target
`'HS'`	HS film
`'MD'`	MD55 film
`'M2'`	MD-v2-55 film
`'EB'`	EBT film
`'PSx'`	High Impact Polystyrene 1.5mm thick
`'Alx'`	Aluminum with integer thickness x in microns
`'Cux'`	Copper with integer thickness x in microns
`'Tix'`	Titanium with integer thickness x in microns
`'Tax'`	Tantalum with integer thickness x in microns
`'Fex'`	Iron with integer thickness x in microns
`'Aux'`	Gold with integer thickness x in microns

Table A.1: Possible input for packmaker.m. The options indicating x is an integer value of the thickness in microns. If omitted the program assumes $25\mu m$ by default.

packmaker.m

```
function packinfo = packmaker(pack,E)
% This function will create an out put struct file to be
%  used in the rcfGUI as the recipe file.
%  E is a vector of the "evenly spaced" energy values in MeV
%  pack is a cell array of strings indicating the pack
%  construction

% Vector coordinates to draw representative pack layers
x=[0,0,0,0;.1,.1,.1,.1;0,.1,.1,0;0,.1,.1,0;0,.1,.1,0;0, ...
    .1,.1,0]’;
y=[0,5,5,0;0,5,5,0;0,0,5,5;0,0,5,5;0,0,0,0;5,5,5,5]’/3;
z=[0,0,5,5;0,0,5,5;0,0,0,0;5,5,5,5;0,0,5,5;0,0,5,5]’/3;
thick = 0;cscale = 5/3+.01;

% Colormaps to paint pack components
temp = flipud(hotblue(72)); temp = temp(21:52,:);
        gold = hot(64);
maps = flipud(temp);      % HD810
maps(:,:,2) = temp;       % HD810 Backwards
maps(:,:,3) = paleblue(32); % MD55
maps(:,:,4) = [zeros(32,1),(0:31)’/42,(0:31)’/31]; % MDv255
maps(:,:,5) = [zeros(32,2),((0:31)/31)’]; % HS
maps(:,:,6) = [(.2:(.65/34):.8)’,(.25:(.65/34):.85)’, ...
            (.25:(.65/34):.85)’]; % Al
maps(:,:,7) = .9*ones(32,3); % HIPS
maps(:,:,8) = [.6*ones(32,1),(0:31)’/31,((0:31)’/31+ ...
            .5)/2]; % EBT
maps(:,:,9) = copper(32); % Copper
maps(:,:,10) = bone(32); % Ti
maps(:,:,11) = gold(31:62,:); % Au
maps(:,:,12) = [(0:31)’,(0:31)’,(0:31)’]/64; % Ta
maps(:,:,13) = flipud(copper(32)*.5); % Fe
ptypes = {’hd’,’dh’,’md’,’m2’,’hs’,’al’,’ps’,’eb’,’cu’,...
            ’ti’,’au’,’ta’,’fe’};types = ...
                zeros(size(ptypes));
dt = [.2,.2,.3,.3,.3,.15,.4,.3,.15,.15,.15,.15,.15]; ...
        st = [1,1,2,2,2,.5,3,2,.5,.5,.5,.5,.5];
for n = 1:length(ptypes)
    types(n) = n*(sum(strncmpi(pack,ptypes{n},2))>0);
end
types = types(find(types>0));
map = maps(:,:,types(1));
for n = 2:length(types)
```

```
    map = [map;maps(:,:,types(n))];
end
clf, set(gcf,'renderer','painters'),hold all
for n = 1:length(pack)
    if (strncmpi(pack{n},'al',2) || ...
        strncmpi(pack{n},'cu',2) || ...
        strncmpi(pack{n},'ti',2) || ...
        strncmpi(pack{n},'au',2) || ...
        strncmpi(pack{n},'ta',2) || ...
        strncmpi(pack{n},'fe',2)) && ~isempty(pack{n}(3:end))
        althick = str2double(pack{n}(3:end));
        if althick >= 5000
            x3 = x*8 + thick;
            thick = thick + .9;
        elseif althick >= 4000
            x3 = x*7 + thick;
            thick = thick + .8;
        elseif althick >= 3000
            x3 = x*6 + thick;
            thick = thick + .7;
        elseif althick >= 2000
            x3 = x*5 + thick;
            thick = thick + .6;
        elseif althick >= 1500
            x3 = x*4 + thick;
            thick = thick + .5;
        elseif althick >= 1000
            x3 = x*3 + thick;
            thick = thick + .4;
        elseif althick >= 500
            x3 = x*2 + thick;
            thick = thick + .3;
        elseif althick >=100
            x3 = x*1 + thick;
            thick = thick + .2;
        else
            x3 = x*st(find(strncmpi(ptypes,pack{n},2))) ...
                + thick;
            thick = thick + dt(find(strncmpi(ptypes, ...
                pack{n},2)));
        end
    else
        x3 = x*st(find(strncmpi(ptypes,pack{n},2))) + thick;
```

```
        thick = thick + dt(find(strncmpi(ptypes,pack{n},2)));
    end
    y3 = y;
    z3 = z;
    c3 = z + find(types==find(strncmpi(ptypes, ...
            pack{n},2)))*cscale;
    fill3(x3,y3,z3,c3)
end
Lbl = {'hd810','hd810','md55','mdv255','hs','Al', ...
        'HIPS','ebt','Cu','Ti','Au','Ta','Fe'};
for n=1:length(types)
    fill3([0,.1,.1,0],[5/3,5/3,5/3,5/3],[2,2,2.1,2.1]+...
            .2*(n-1),map(32*n,:));
    text(.1,5/3-.1,2.1+.2*(n-1),Lbl{types(n)})
end
hold off
colormap(map),axis image, axis off, axis tight,view([-22,22])

% If energy value is given the call filmpack.m to solve
if nargin < 2
    packinfo.Pack = pack;
    packinfo.ERange = [];
    packinfo.Result = [];
    return
else
    pause(1)
    for n = 1:length(E)
        D(n,:) = filmpack(E(n),pack);
    end
    D = [E',D];
    packinfo.Pack = pack;
    packinfo.ERange = [min(E),max(E)];
    packinfo.Result = D;
end
```

filmpack.m

```
function [EDose,xrange,EnergyINS]=filmpack(EIN,PackComp)
% Compute the absorbed dose each active layer of film for
%  a proton with energy EIN (MeV).

% -------- In microns ---------- DEFAULTS
```

```
ALTHICK        = 25;
HDGELTHICK     = 0.75;
HDACTIVETHICK = 6.5;
HDBASETHICK   = 97;
HSBASETHICK   = 97;
HSACTIVETHICK = 40;
MDBASETHICK   = 67;
MDACTIVETHICK = 16;
MDGLUETHICK   = 20;
MDMIDTHICK    = 25;
M2BASETHICK   = 96;
M2GELTHICK    = 0.75;
M2ACTIVETHICK = 17.5;
M2GLUETHICK   = 32;
M2MIDTHICK    = 25;
PSHIPSTHICK   = 1587.5;
EBACTIVETHICK = 17;
EBBASETHICK   = 97;
EBSURFTHICK   = 6;

dEper = .005;
minE = .05;
% ------------------------------

if nargin < 2
    PackComp = {'HD','MD','HS'};
end
Ion = 'H';
EDose=0; xrange=0; EnergyINS=0;

% Get dE/dx (MeV/mm) for all materials used SRIM
[E,dEdx] = ExtractSRIM([Ion,' in Aluminum']);
sdata(1,:) = {E,dEdx};
[E,dEdx] = ExtractSRIM([Ion,' in Active Layer']);
sdata(2,:) = {E,dEdx};
[E,dEdx] = ExtractSRIM([Ion,' in Polyester Base']);
sdata(3,:) = {E,dEdx};
[E,dEdx] = ExtractSRIM([Ion,' in Gelatin']);
sdata(4,:) = {E,dEdx};
[E,dEdx] = ExtractSRIM([Ion,' in Adhesive']);
sdata(5,:) = {E,dEdx};
[E,dEdx] = ExtractSRIM([Ion,' in HIPS']);
sdata(6,:) = {E,dEdx};
```

```
[E,dEdx] = ExtractSRIM([Ion,' in EBTACTIVE']);
sdata(7,:) = {E,dEdx};
[E,dEdx] = ExtractSRIM([Ion,' in EBTSURF']);
sdata(8,:) = {E,dEdx};
[E,dEdx] = ExtractSRIM([Ion,' in Copper']);
sdata(9,:) = {E,dEdx};
[E,dEdx] = ExtractSRIM([Ion,' in Titanium']);
sdata(10,:) = {E,dEdx};
[E,dEdx] = ExtractSRIM([Ion,' in Gold']);
sdata(11,:) = {E,dEdx};
[E,dEdx] = ExtractSRIM([Ion,' in Tantalum']);
sdata(12,:) = {E,dEdx};
[E,dEdx] = ExtractSRIM([Ion,' in Iron']);
sdata(13,:) = {E,dEdx};

% Create Thickness/Type Arrays
clear TauArray;
clear TypeArray;
IDArray = [];
counter = 0;
for n = 1:length(PackComp)
    layerstring = PackComp{n};
    if strcmpi(layerstring(1:2),'Al')
        counter = counter + 1;
        if length(layerstring)==2
            TauArray(counter) = ALTHICK;
        else
            TauArray(counter) =  ...
                str2num(layerstring(3:end));
        end
        TypeArray(counter) = 1;
        IDArray = [IDArray,n];
    elseif strcmpi(layerstring(1:2),'Cu')
        counter = counter + 1;
        if length(layerstring)==2
            TauArray(counter) = ALTHICK;
        else
            TauArray(counter) = ...
                str2num(layerstring(3:end));
        end
        TypeArray(counter) = 9;
        IDArray = [IDArray,n];
    elseif strcmpi(layerstring(1:2),'Ti')
```

```
        counter = counter + 1;
        if length(layerstring)==2
            TauArray(counter) = ALTHICK;
        else
            TauArray(counter) = ...
                str2num(layerstring(3:end));
        end
        TypeArray(counter) = 10;
        IDArray = [IDArray,n];
    elseif strcmpi(layerstring(1:2),'Au')
        counter = counter + 1;
        if length(layerstring)==2
            TauArray(counter) = ALTHICK;
        else
            TauArray(counter) = ...
                str2num(layerstring(3:end));
        end
        TypeArray(counter) = 11;
        IDArray = [IDArray,n];
    elseif strcmpi(layerstring(1:2),'Ta')
        counter = counter + 1;
        if length(layerstring)==2
            TauArray(counter) = ALTHICK;
        else
            TauArray(counter) = ...
                str2num(layerstring(3:end));
        end
        TypeArray(counter) = 12;
        IDArray = [IDArray,n];
    elseif strcmpi(layerstring(1:2),'Fe')
        counter = counter + 1;
        if length(layerstring)==2
            TauArray(counter) = ALTHICK;
        else
            TauArray(counter) = ...
                str2num(layerstring(3:end));
        end
        TypeArray(counter) = 13;
        IDArray = [IDArray,n];
    elseif strcmpi(layerstring,'HD')
        counter = counter + 3;
        TauArray(counter-2) = HDGELTHICK;
        TauArray(counter-1) = HDACTIVETHICK;
```

```
        TauArray(counter)   = HDBASETHICK;
        TypeArray(counter-2) = 4;
        TypeArray(counter-1) = 2;
        TypeArray(counter)   = 3;
        IDArray = [IDArray,n,n,n];
    elseif strcmpi(layerstring,'DH')
        counter = counter + 3;
        TauArray(counter-2) = HDBASETHICK;
        TauArray(counter-1) = HDACTIVETHICK;
        TauArray(counter)   = HDGELTHICK;
        TypeArray(counter-2) = 3;
        TypeArray(counter-1) = 2;
        TypeArray(counter)   = 4;
        IDArray = [IDArray,n,n,n];
    elseif strcmpi(layerstring,'HS')
        counter = counter + 3;
        TauArray(counter-2) = HSBASETHICK;
        TauArray(counter-1) = HSACTIVETHICK;
        TauArray(counter)   = HSBASETHICK;
        TypeArray(counter-2) = 3;
        TypeArray(counter-1) = 2;
        TypeArray(counter)   = 3;
        IDArray = [IDArray,n,n,n];
    elseif strcmpi(layerstring,'EB')
        counter = counter + 5;
        TauArray(counter-4)  = EBBASETHICK;
        TauArray(counter-3)  = EBACTIVETHICK;
        TauArray(counter-2)  = EBSURFTHICK;
        TauArray(counter-1)  = EBACTIVETHICK;
        TauArray(counter)    = EBBASETHICK;
        TypeArray(counter-4) = 3;
        TypeArray(counter-3) = 7;
        TypeArray(counter-2) = 8;
        TypeArray(counter-1) = 7;
        TypeArray(counter)   = 3;
        IDArray = [IDArray,n,n,n,n,n];
    elseif strcmpi(layerstring,'PS')
        counter = counter + 1;
        TauArray(counter) = PSHIPSTHICK;
        TypeArray(counter) = 6;
        IDArray = [IDArray,n];
    elseif strcmpi(layerstring,'MD')
        counter = counter + 7;
```

```
        TauArray(counter-6) = MDBASETHICK;
        TauArray(counter-5) = MDACTIVETHICK;
        TauArray(counter-4) = MDGLUETHICK;
        TauArray(counter-3) = MDMIDTHICK;
        TauArray(counter-2) = MDGLUETHICK;
        TauArray(counter-1) = MDACTIVETHICK;
        TauArray(counter) = MDBASETHICK;
        TypeArray(counter-6) = 3;
        TypeArray(counter-5) = 2;
        TypeArray(counter-4) = 5;
        TypeArray(counter-3) = 3;
        TypeArray(counter-2) = 5;
        TypeArray(counter-1) = 2;
        TypeArray(counter) = 3;
        IDArray = [IDArray,n,n,n,n,n,n,n];
    elseif strcmpi(layerstring,'M2')
        counter = counter + 9;
        TauArray(counter-8) = M2BASETHICK;
        TauArray(counter-7) = M2ACTIVETHICK;
        TauArray(counter-6) = M2GELTHICK;
        TauArray(counter-5) = M2GLUETHICK;
        TauArray(counter-4) = M2MIDTHICK;
        TauArray(counter-3) = M2GLUETHICK;
        TauArray(counter-2) = M2GELTHICK;
        TauArray(counter-1) = M2ACTIVETHICK;
        TauArray(counter) = M2BASETHICK;
        TypeArray(counter-8) = 3;
        TypeArray(counter-7) = 2;
        TypeArray(counter-6) = 4;
        TypeArray(counter-5) = 5;
        TypeArray(counter-4) = 3;
        TypeArray(counter-3) = 5;
        TypeArray(counter-2) = 4;
        TypeArray(counter-1) = 2;
        TypeArray(counter) = 3;
        IDArray = [IDArray,n,n,n,n,n,n,n,n,n];
    else
        error('Film Type Not Found')
    end
end

stopflag = 0;
travelX = 0; EDose = zeros(length(PackComp),1);
```

```
EnergyIN = EIN(1);
EnergyINS = 0;
oldtype = 0;
for n = 1:length(TypeArray)
    newtype = IDArray(n);
    if oldtype ~= newtype
        EnergyINS(IDArray(n)) = EnergyIN;
    end
    oldtype = newtype;
    nt = TypeArray(n);
    xinlayer = 0;
    while xinlayer < TauArray(n)
        if EnergyIN <= 0, stopflag = 1; break, end
        dEdx = pchip(sdata{nt,1},sdata{nt,2},EnergyIN);
        dx = 1000*dEper*EnergyIN/dEdx;
        dx = min(dx,TauArray(n)-xinlayer);
        xinlayer = xinlayer + dx;
        EnergyOUT = EnergyIN - dx*dEdx/1000;
        if EnergyOUT <= minE, EnergyOUT = 0; end
        travelX = travelX + dx;
        EDose(IDArray(n)) = EDose(IDArray(n)) + ...
            (EnergyIN-EnergyOUT)*(nt==2||nt==7);
        EnergyIN = EnergyOUT;
    end
end
EnergyINS = [EnergyINS,EnergyIN];
if stopflag
    xrange = travelX;
else
    xrange = -1;
end
```

A.1.3 FITTING $dN/d\mathcal{E}$

When fitting a distribution to the RCF dose data, if one wishes to draw a line of the fit over the data points one needs to integrate the fitted function times the single proton response of the film pack and then convert the value to the equivalent dose. When dealing with multiple types of film per pack, this was sometimes tedious. To make the genetic algorithm solve for the least squares difference, it was necessary to adjust the boundaries to of the possible parameter values in-order to shorten the time to find a good convergence with the data. The GUI could be called from a command line as `params=RCFfitGUI(data,recipe,area);`. Data is the vector containing the dose on each layer of film in *krads*, recipe is the output of packmaker.m and area is the total area of the film in cm^2.

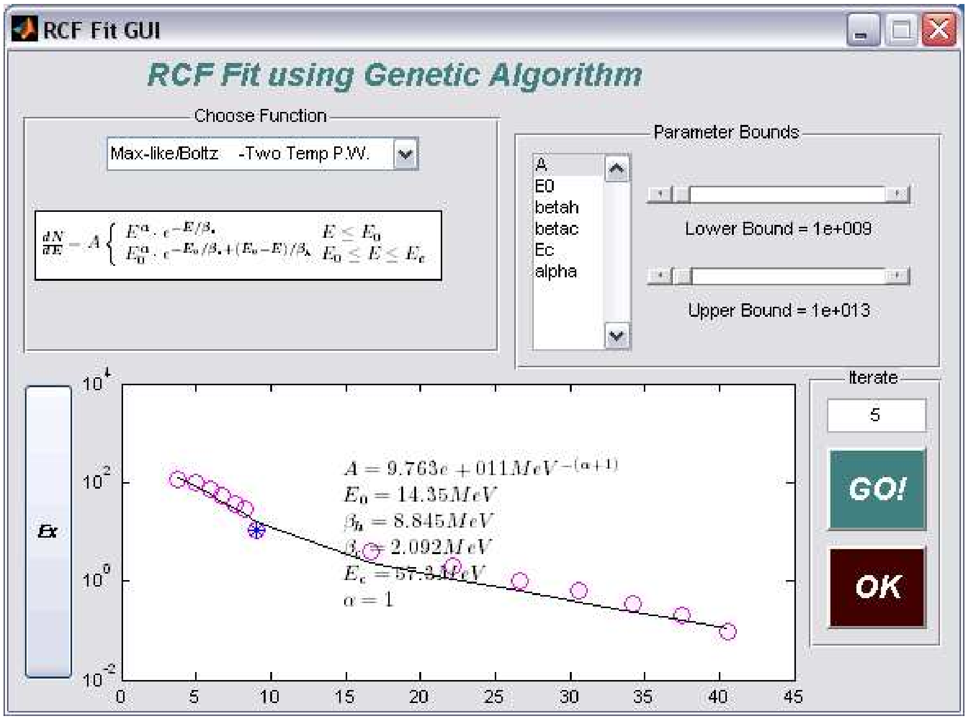

RCF Fit GUI

RCF Fit using Genetic Algorithm

Choose Function: Max-like/Boltz -Two Temp P.W.

$$\frac{dN}{dE} = A\begin{cases} E^{\alpha}\cdot e^{-E/\beta_c} & E \le E_0 \\ E_0^{\alpha}\cdot e^{-E_0/\beta_c+(E_0-E)/\beta_h} & E_0 \le E \le E_c \end{cases}$$

Parameter Bounds: A

Lower Bound = 1e+009

Upper Bound = 1e+013

Iterate: 5

$A = 9.763e+011 MeV^{-(\alpha+1)}$

$E_0 = 14.35 MeV$

$\beta_h = 8.845 MeV$

$\beta_c = 2.092 MeV$

$E_c = 57.3 MeV$

$\alpha = 1$

Figure A.2: A screen-shot of the RCF fitting GUI written to interface with the input parameters of a genetic algorithm written to fit $dN/d\mathcal{E}$.

The GUI calls the function geneticRCF.m to fit the parameters, params to the function N. Params is an array of the parameters described by the arbitray function `N=@(params,E)(...`. ITER is the number of generations the algorithm computes.

The variable p is an initial guess on the values of the parameers and b is a two dimensional array which gives the upper and lower values the the parameters are allowed to take in the program. The call syntax is `params = geneticRCF(ITER,Er,Re,N,p,b);`.

geneticRCF.m

```
function [params,rankings] = geneticRCF(MAXITERATE,...
    REALvals,Response,func,params,parambounds,weights)

% Seed random number generator
rand('state',sum(100*clock));
% Disable warning when rounding
warning('off','MATLAB:intConvertNonIntVal')
warning('off','MATLAB:intConvertOverflow')

SIGDEC      = 5;   % Sig. Decimal Places in params=10^(##)
POPULATION  = 51;  % Population Size
MERCYKILL   = 30;  % Replace with childeren this many
MUTATETHESE = 40;  % Population subject to mutation
MUTATERATE  = 0.1; % Rate of mutation (percent)
MATERATE    = 0.5; % Percent population allowed to bread
TIME2MOVE   = 0.2; % If this percent of the
                        % town is the same then move

% Initiallize Population
if nargin < 7
    %weights = (REALvals(1)-REALvals*.7)/ ...
        max(REALvals(1)-REALvals*.7);
    weights = ones(size(REALvals));
end
TownsPeople = num2str(zeros(POPULATION,...
        length(params)*32),'%.1d');
TownsPeople(1,:) = codesequence(params,SIGDEC);
for n = 2:POPULATION
    for m = 1:length(params)
        params(m) = (parambounds(m,2)- ...
                parambounds(m,1))*rand + ...
            parambounds(m,1);
    end
    TownsPeople(n,:) = codesequence(params,SIGDEC);
```

```
end
rankings = fitness(REALvals,Response,func,...
    TownsPeople,parambounds,weights,SIGDEC);
[rankings,Index] = sort(rankings);
TownsPeople = TownsPeople(Index,:);
params = decode(TownsPeople(1,:),SIGDEC);
ITERATE = MAXITERATE-1;
while ITERATE > 1
    NURSERY = num2str(zeros(MERCYKILL,...
            length(params)*32),'%.1d');
    for k = 1:MERCYKILL
        n = ceil(ceil(MATERATE*POPULATION)*rand); m = n;
        while m==n
            m = ceil(ceil(MATERATE*POPULATION)*rand);
        end
        baby = mate(TownsPeople,n,m);
        if isINbounds(decode(baby,SIGDEC),parambounds)
            NURSERY(k,:) = baby;
        else
            NURSERY(k,:) = adoption(parambounds,SIGDEC);
        end
    end
    TownsPeople((POPULATION-MERCYKILL+1):POPULATION,:)...
                = NURSERY;
    rankings = fitness(REALvals,Response,func,...
            TownsPeople,parambounds,weights,SIGDEC);
    [rankings,Index] = sort(rankings);
    TownsPeople = TownsPeople(Index,:);
    for k = (POPULATION-MUTATETHESE+1):POPULATION
        monster = mutate(TownsPeople(k,:),MUTATERATE);
        if isINbounds(decode(monster,SIGDEC),parambounds)
            TownsPeople(k,:) = monster;
        else
            TownsPeople(k,:) = adoption(parambounds,SIGDEC);
        end
    end
    rankings = fitness(REALvals,Response,func,...
            TownsPeople,parambounds,weights,SIGDEC);
    [rankings,Index] = sort(rankings);
    TownsPeople = TownsPeople(Index,:);
    ITERATE = ITERATE - 1;
    if (sum(rankings(1)==rankings)> ...
            POPULATION*TIME2MOVE) && (ITERATE>0);
```

```
        params = geneticRCF(ITERATE,REALvals,...
                Response,func,params,parambounds);
        break
    else
        params = decode(TownsPeople(1,:),SIGDEC);
    end
end

function inbounds = isINbounds(params,parambounds)
inbounds = 1;
for n = 1:length(params);
    inbounds = inbounds && (params(n) <= ...
        parambounds(n,2)) && (params(n) >= ...
            parambounds(n,1));
end

function child = mate(TownsPeople,n,m)
child = TownsPeople(n,:);
for k = 1:length(TownsPeople(n,:))
    if rand > 0.5
        child(1,k) = TownsPeople(m,k);
    end
end

function freak = mutate(code,MUTATERATE)
freak = code;
for n=1:length(code)
    if rand < MUTATERATE
        freak(n) = num2str(ceil(rand*2)-1,'%.1d');
    end
end

function newbie = adoption(parambounds,SIGDEC)
params = zeros(1,size(parambounds,1));
for m = 1:size(parambounds,1)
    params(m) = (parambounds(m,2)-...
            parambounds(m,1))*rand+...
            parambounds(m,1);
end
newbie = codesequence(params,SIGDEC);

function rankings = fitness(REALvals,Response,...
        func,TownsPeople,parambounds,weights,SIGDEC)
```

```
rankings = Inf*ones(1,size(TownsPeople,1));
CALCvals = zeros(size(REALvals));
E = Response(:,1); dE = (max(E)-min(E))/(length(E)-1);
for n=1:size(TownsPeople,1)
    params = decode(TownsPeople(n,:),SIGDEC);
    if isINbounds(params,parambounds)
        for m = 1:length(REALvals)
           CALCvals(m) = dE*sum(func(params,E) ...
            .*Response(:,m+1));
        end
        rankings(n) = sum(weights.* ...
            (REALvals-CALCvals).^2)...
            /sum((REALvals-mean(REALvals)).^2);
    end
end

function code = codesequence(params,SIGDEC)
code = [];
for n=1:length(params)
    num = uint32(log10(params(n))*10^SIGDEC);
    code = [code,dec2bin(num,32)];
end

function params = decode(code,SIGDEC)
params = zeros(1,length(code)/32);
for n=1:length(params)
    params(n) = 10^(bin2dec(code((1:32)...
        +32*(n-1)))*10^(-SIGDEC));
end
```

A.2 THOMSON SPECTROMETER

One challenge in particular for analyzing the Thomson data was trying to get lineouts of the parabolic traces and the converting the coordinateness to an energy scale. The GUI seen in figure A.3 was written to open the IMG formatted images from the FUJIFILM$^{\text{TM}}$scanner and identify the brightest pixels bound by a manually inputed box. The program took those coordinates and output a spectrum to the MATLAB®command environment for further analysis. The program also fit a parabola to the coordinates.

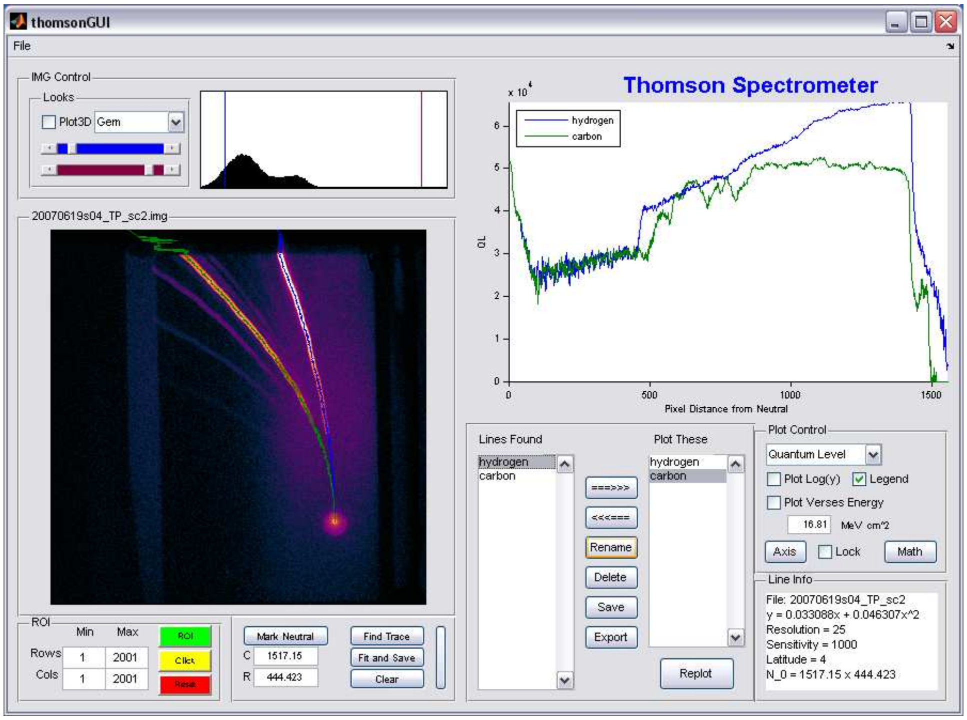

☐ Plot3D: Gem

ROI

	Min	Max
Rows	1	2001
Cols	1	2001

C 1517.15

R 444.423

Lines Found: hydrogen, carbon

Plot These: hydrogen, carbon

Plot Control: Quantum Level

☐ Plot Log(y) ☑ Legend

☐ Plot Verses Energy

16.81 MeV cm^2

☐ Lock

Line Info

File: 20070619s04_TP_sc2
y = 0.033088x + 0.046307x^2
Resolution = 25
Sensitivity = 1000
Latitude = 4
N_0 = 1517.15 x 444.423

Figure A.3: A screen-shot of the Thomson GUI written to take lineouts of the parabolic traces and to convert them to PSL values.

APPENDIX B

IONIZATION POTENTIALS

The following values for the ionization potentials were used in the calculations of this work. The values were obtained from three different sources, NIST [54], ORNL [55], and FAC [56]. The accuracy of the values decreases as the ionization number Z increases. Also presented in each table are the minimum electric field magnitudes needed to ionize according to ADK theory as well as the estimated total ionization rate including FIBS and collisional ionization assuming $kT_e = 1.7 MeV$ and $n_e = 5 \times 10^{19} cm^{-3}$.

Ionization Potentials - Carbon

Z	**IP** (eV)	**Source**	**Minimum E to Ionize** (TV/m)	**Ionization Rate** ($\mathbf{ps^{-1}}$)
1	11.2	NIST	0.022	7.61e+004
2	24.4	NIST	0.052	4.23e+005
3	47.9	NIST	0.13	1.66e+006
4	64.5	NIST	0.18	4.45e+006
5	392	NIST	5.3	0.00119
6	490	NIST	6.9	0.000928

Table B.1: Ionization potentials of carbon along with the minimum electric field needed for field ionization

Ionization Potentials - Oxygen

Z	**IP** (**eV**)	**Source**	**Minimum E to Ionize** (**TV/m**)	**Ionization Rate** ($\mathbf{ps^{-1}}$)
1	13.618	NIST	0.032	1.06e+005
2	35.117	NIST	0.11	4.58e+005
3	54.934	NIST	0.17	1.21e+006
4	77.413	NIST	0.26	1.93e+006
5	113.9	NIST	0.45	5.97e+005
6	138.12	NIST	0.55	3.59e+005
7	739.32	NIST	14	0.000584
8	871.39	NIST	16	0.000485

Table B.2: Ionization potentials of oxygen along with the minimum electric field needed for field ionization

Ionization Potentials - Erbium

Z	IP (eV)	Source	Minimum E to Ionize (TV/m)	Ionization Rate (ps^{-1})
1	5.227	ORNL	0.0047	4.34e+003
2	11.52	ORNL	0.012	2.52e+004
3	25.03	ORNL	0.036	9.57e+005
4	58.89	ORNL	0.15	5.9e+006
5	78.76	ORNL	0.22	1.12e+007
6	96.29	ORNL	0.27	1.88e+007
7	113.8	ORNL	0.32	2.58e+007
8	131.4	ORNL	0.37	2.92e+007
9	157.6	ORNL	0.48	1.09e+007
10	176.5	ORNL	0.54	7.23e+006
11	200.7	ORNL	0.64	2.1e+006
12	234.6	ORNL	0.8	1.31e+005
13	268.4	ORNL	0.96	5.79e+003
14	290	ORNL	1	1.2e+003
15	311.2	ORNL	1.1	231
16	344.8	ORNL	1.3	5.09
17	380.8	ORNL	1.5	0.0572
18	415.7	ORNL	1.7	0.00168
19	450.6	ORNL	1.9	0.00102
20	485.4	ORNL	2	0.000938
21	520.3	ORNL	2.2	0.000868
22	555.2	ORNL	2.4	0.000807
23	762	ORNL	4.4	0.000565
24	808	ORNL	4.7	0.000528
25	854	ORNL	5.1	0.000496
26	900.1	ORNL	5.4	0.000468
27	946.2	ORNL	5.8	0.000442
28	992.3	ORNL	6.1	0.000419
29	1049	ORNL	6.6	0.000393
30	1096	ORNL	7	0.000374
31	1143	ORNL	7.3	0.000357
32	1190	ORNL	7.7	0.000341
33	1379	ORNL	10	0.000288
34	1429	ORNL	10	0.000277
35	1478	ORNL	11	0.000266

Continued on next page

Table B.3: Ionization potentials of erbium along with the minimum electric field needed for field ionization

Table B.3 – continued from previous page

Z	**IP** (eV)	**Source**	**Minimum E to Ionize (TV/m)**	**Ionization Rate (ps^{-1})**
36	1528	ORNL	11	0.000256
37	1623	ORNL	12	0.000239
38	1676	ORNL	13	0.00023
39	1815	ORNL	15	0.00021
40	1868	ORNL	15	0.000204
41	2892	ORNL	35	0.000123
42	3025	ORNL	38	0.000117
43	3157	ORNL	40	0.000111
44	3290	ORNL	43	0.000106
45	3423	ORNL	45	0.000101
46	3555	ORNL	48	9.69e-005
47	3731	ORNL	51	9.16e-005
48	3866	ORNL	54	8.78e-005
49	4001	ORNL	57	8.44e-005
50	4137	ORNL	59	8.12e-005
51	4492	ORNL	69	7.37e-005
52	4611	ORNL	71	7.15e-005
53	4731	ORNL	73	6.94e-005
54	4850	ORNL	76	6.74e-005
55	5241	ORNL	87	6.16e-005
56	5368	ORNL	89	5.99e-005
57	5643	ORNL	97	5.64e-005
58	5764	ORNL	99	5.51e-005
59	12190	ORNL	4.4e+002	2.26e-005
60	12540	ORNL	4.6e+002	2.18e-005
61	12880	ORNL	4.7e+002	2.12e-005
62	13230	ORNL	4.9e+002	2.05e-005
63	14490	ORNL	5.8e+002	1.84e-005
64	14870	ORNL	6e+002	1.78e-005
65	15500	ORNL	6.4e+002	1.69e-005
66	15820	ORNL	6.6e+002	1.65e-005
67	64370	ORNL	1.1e+004	2.84e-006
68	65700	ORNL	1.1e+004	2.76e-006

Ionization Potentials - Gold

Z	**IP (eV)**	**Source**	**Minimum E to Ionize (TV/m)**	**Ionization Rate ($\mathbf{ps^{-1}}$)**
1	9.226	NIST	0.015	4.66e+004
2	16.09	FAC	0.022	1.44e+005
3	28.138	FAC	0.046	1.36e+006
4	42.003	FAC	0.077	8.07e+006
5	57.575	FAC	0.12	3.11e+007
6	73.151	FAC	0.15	8.55e+007
7	92.06	FAC	0.21	1.47e+008
8	111.076	FAC	0.27	1.88e+008
9	129.294	FAC	0.32	2.04e+008
10	148.862	FAC	0.38	1.59e+008
11	165.175	FAC	0.43	1.48e+008
12	250.3	ORNL	0.91	1.46e+004
13	274.7	ORNL	1	2.28e+003
14	299.1	ORNL	1.1	297
15	323.5	ORNL	1.2	32.6
16	365.1	ORNL	1.4	0.17
17	391.8	ORNL	1.6	0.00942
18	432.9	ORNL	1.8	0.00109
19	487.4	ORNL	2.2	0.000934
20	516.8	ORNL	2.3	0.000874
21	545.7	ORNL	2.5	0.000823
22	599.7	ORNL	2.8	0.00074
23	654.2	ORNL	3.2	0.000671
24	708.8	ORNL	3.6	0.000613
25	763.3	ORNL	4	0.000564
26	817.9	ORNL	4.5	0.000521
27	872.4	ORNL	4.9	0.000485
28	930.9	ORNL	5.4	0.00045
29	986.2	ORNL	5.8	0.000422
30	1042	ORNL	6.3	0.000396
31	1097	ORNL	6.7	0.000374
32	1152	ORNL	7.2	0.000353
33	1207	ORNL	7.7	0.000335
34	1516	ORNL	12	0.000258
35	1575	ORNL	12	0.000247

Continued on next page

Table B.4: Ionization potentials of gold along with the minimum electric field needed for field ionization

Table B.4 – continued from previous page

Z	IP (eV)	Source	Minimum E to Ionize (TV/m)	Ionization Rate ($\mathbf{ps^{-1}}$)
36	1634	ORNL	13	0.000237
37	1692	ORNL	13	0.000228
38	1751	ORNL	14	0.000219
39	1810	ORNL	15	0.000211
40	1888	ORNL	15	0.000201
41	1920	ORNL	16	0.000197
42	1960.56	FAC	16	0.000193
43	2024.73	FAC	17	0.000186
44	2256.76	FAC	20	0.000164
45	2315.85	FAC	21	0.000159
46	2381.39	FAC	21	0.000154
47	2441.42	FAC	22	0.00015
48	2637.7	FAC	25	0.000137
49	2706.55	FAC	26	0.000133
50	2868.36	FAC	29	0.000124
51	2939.06	FAC	29	0.000121
52	4879.79	FAC	80	6.69e-005
53	5013.76	FAC	82	6.48e-005
54	5155.83	FAC	85	6.28e-005
55	5307.28	FAC	89	6.07e-005
56	5451.88	FAC	92	5.88e-005
57	5593.26	FAC	95	5.7e-005
58	5846.23	FAC	1e+002	5.41e-005
59	5993.11	FAC	1.1e+002	5.26e-005
60	6155.64	FAC	1.1e+002	5.1e-005
61	6303.19	FAC	1.1e+002	4.96e-005
62	6718.87	FAC	1.3e+002	4.6e-005
63	6850.31	FAC	1.3e+002	4.49e-005
64	6995.37	FAC	1.3e+002	4.38e-005
65	7129.02	FAC	1.4e+002	4.28e-005
66	7754.57	FAC	1.6e+002	3.88e-005
67	7910.77	FAC	1.6e+002	3.79e-005
68	8208.42	FAC	1.7e+002	3.63e-005
69	8354.52	FAC	1.8e+002	3.55e-005
70	18034	FAC	8.1e+002	1.41e-005
71	18391	FAC	8.3e+002	1.37e-005
72	18786	FAC	8.5e+002	1.34e-005

Continued on next page

Table B.4 – continued from previous page

Z	**IP** (**eV**)	**Source**	**Minimum E to Ionize** (**TV/m**)	**Ionization Rate** ($\mathbf{ps^{-1}}$)
73	19149.4	FAC	8.7e+002	1.31e-005
74	21469.5	FAC	1.1e+003	1.14e-005
75	21923	FAC	1.1e+003	1.11e-005
76	22495.9	FAC	1.2e+003	1.07e-005
77	22865.4	FAC	1.2e+003	1.05e-005
78	91498.2	FAC	1.9e+004	1.78e-006
79	93244	FAC	1.9e+004	1.74e-006

BIBLIOGRAPHY

[1] J. Lindl, "Development of the indirect-drive approach to inertial confinement fusion and the target physics basis for ignition and gain," *Phys Plamsas* **2** (1995) 3933.

[2] M. Key, "Status of and prospects for the fast ignition inertial fusion concept," *Phys. Plasmas* **14** (2007) 055502.

[3] M. D. Rosen, "The physics issues that determine inertial confinement fusion target gain and drvier requirements: A tutorial," *Phys. Plasmas* **6** (1999) 1690.

[4] M. Tabak, J. Hammer, M. E. Glinsky, W. L. Kruer, S. C. Wilks, J. Woodworth, E. M. Campbell, M. D. Perry, and R. J. Mason, "Ignition and high gain with ultrapowerful lasers," *Phys. Plamsas* **1** (1994) 1626.

[5] J. S. Green, V. M. Ovchinnikov, R. G. Evans, K. U. Akli, H. Azechi, F. N. Beg, C. Bellei, R. R. Freeman, H. Habara, R. Heathcote, M. H. Key, J. A. King, K. L. Lancaster, N. C. Lopes, T. Ma, A. J. MacKinnon, K. Markey, A. McPhee, Z. Najmudin, P. Nilson, R. Onofrei, R. Stephens, K. Takeda, K. A. Tanaka, W. Theobald, T. Tanimoto, J. Waugh, L. Van Woerkom, N. C. Woolsey, M. Zepf, J. R. Davies, and P. A. Norreys, "Effect of laser intensity on fast-electron-beam divergence in solid-density plasmas, journal = Phys. Rev. Lett., year = 2008, volume = 1, number = 3,".

[6] R. Freeman, K. Akli, D. Batani, S. Baton, S. Hatchett, D. Hey, M. Key, J. King, A. Mackinnon, P. Norreys, R. Snavely, R. Stephens, C. Stoeckl, R. Town, and B. Zhang, "Experiment vs. theory on electric inhibition of fast electron penetration of targets," in *32nd EPS Plasma Physics conference*. Tarragona, Spain, 2005.

[7] M. Allen, P. K. Patel, A. Mackinnon, D. Price, S. Wilks, and E. Morse, "Direct experimental evidence of back-surface ion acceleration from laser-irradiated gold foils," *Phys. Rev. Lett.* **93** (Dec, 2004) 265004.

[8] R. Snavely, M. Key, S. Hatchett, T. Cowan, M. Roth, T. Phillips, M. Stoyer, E. Henry, T. Sangser, M. Signh, S. Wilks, A. Mackinnon, A. Offenberger,

D. Pennington, K. Yasuike, A. Langdon, B. Lasinski, J. Johnson, M. Perry, and E. Campbell, "Intense high-energy proton beams from petawatt-laser irradiation of solids," *Phys. Rev. Lett.* **85** (2000) 2945.

[9] J. Fuchs, P. Antici, E. d'Humieres, E. Lefebvre, M. Borghesi, E. Brambrink, C. Cecchetti, M. Kaluza, V. Malka, M. Manclossi, S. Meyroneinc, P. Mora, J. Schreiber, T. Toncian, H. Pepin, and P. Audebert, "Laser-driven proton scaling laws and new paths towards energy increase," *Nature* **2** (2006) 48.

[10] J. Fuchs, Y. Sentoku, E. d'Humieres, T. Cowan, J. Cobble, P. Audebert, A. Kemp, A. Nikroo, P. Antici, E. Brambrink, A. Blazevic, E. Campbell, J. Fernandez, J. Gauthier, M. Geissel, M. Hegelich, S. Karsch, H. Popescu, N. Renard-LeGallaudec, M. Roth, J. Schreiber, R. Stephens, and H. Pepin, "Comparative spectra and efficiencies of ions laser-accelerated forward from the front and rear surfaces of thin solid foils," *Phys. Plasmas* **14** (2007) 053105.

[11] A. Mackinnon, M. Borghesi, S. Hatchett, M. Key, P. Patel, H. Campbell, A. Schiavi, R. Snavely, S. Wilks, and O. Willi, "Effect of plasma scale length on multi-mev proton production by intense laser pulses," *Phys. Rev. Lett.* **86** (2001) 1769.

[12] A. Mackinnon, Y. Sentoku, P. Patel, D. Price, S. Hatchett, M. Key, C. Andersen, R. Snavely, and R. Freeman, "Enhancement of proton acceleration by hot-electron recirculation in thin foils irradiated by ultraintense laser pulses," *Phys. Rev. Lett.* **88** (2002) 215006.

[13] S. Wilks, A. Langdon, T. Cowan, M. Roth, M. Singh, S. Hatchett, M. Key, D. Pennington, A. MacKinnon, and R. Snavely *Phys. Plasmas* **8** (2001) 542.

[14] S. P. Hatchett, C. G. Brown, T. E. Cowan, E. A. Henry, J. S. Johnson, M. H. Key, J. A. Koch, A. B. Langdon, B. F. Lasinski, R. W. Lee, A. J. Mackinnon, D. M. Pennington, M. D. Perry, T. W. Phillips, M. Roth, T. C. Sangster, M. S. Singh, R. A. Snavely, M. A. Stoyer, S. C. Wilks, and K. Yasuikec *Phys. Plasmas* **7** (2000) 2076.

[15] P. Patel, A. Mackinnon, M. Key, T. Cowan, M. Foord, M. Allen, D. Price, H. Ruhl, P. Springer, and R. Stephens, "Isochoric heating of solid-density matter with an ultrafast proton beam," *Phys. Rev. Lett.* **91** (2003) 125004.

[16] M. Roth, T. Cowan, M. Key, S. Hatchett, C. Brown, W. Fountain, J. Johnson, D. Pennington, R. Snavely, S. Wilks, K. Yasuike, H. Ruhl, F. Pegoraro, S. Bulanov, E. Campbell, M. D. Perry, and H. Powell1, "Fast ignition by intense laser-accelerated proton beams," *Phys. Rev. Lett.* **86** (2001) 436.

[17] S. Atzeni, M. Temporal, and J. Honrubia, "A first analysis of fast ignition of precompressed icf fuel by laser-accelerated protons," *Nucl. Fusion* **42** (2002) L1.

[18] A. Mackinnon, P. Patel, M. Borghesi, R. Clarke, R. Freeman, H. Habara, S. Hatchett, D. Hey, D. Hicks, S. Kar, M. Key, J. King, K. Lancaster, D. Neely, A. Nikkro, P. Norreys, M. Notley, T. Phillips, L. Romagnani, R. Snavely, R. Sthephens, and R. Town, "Proton radiaography of laser-driven implosions," *Phys. Rev. Lett.* **97** (2006) 045001.

[19] P. Mora, "Plasma expansion into a vacuum," *Phys. Rev. Lett.* **90** (2003) 185002.

[20] M. Foord, A. Mackinnon, P. Patel, A. MacPhee, Y. Ping, M. Tabak, and R. Town, "Enhanced proton production from hydride-coated foils," *J. Appl. Phys.* **103** (2008) 056106.

[21] M. Nakatsutsumi, R. Kodama, Y. Aglitskiy, K. Akli, D. Batani, S. Baton, F. Beg, A. Benuzzi-Mounaix, S. Chen, D. Clark, J. Davies, R. Freeman, J. Fuchs, J. Green, C. Gregory, P. Guillou, H. Habara, R. Heathcote, D. Hey, K. Highbarger, P. Jaanimagi, M. H. Key, M. Koenig, K. Krushelknick, K. Lancaster, B. Loupais, T. Ma, A. Macphee, A. Mackinnon, K. Mima, A. Morace, H. Nakamura, P. Norryes, D. Piazza, C. Rousseaux, R. Stephans, M. Storm, M. Tampo, W. Theobald, L. V. Woerkom, R. Weber, M. Wei, and N. Woolsey, "Heating of solid target in electron refluxing dominated regime with ultra-intense laser," *J. Phys. Conf. Series.* **112** (2008) 022063.

[22] A. Baitin and K. Kuzanyan, "A self-similar solution for expansion into a vacuum of a collisionless plasma bunch," *J. Plasma Phys.* **90** (1998).

[23] P. Mora, "Collisionless expansion of a gaussian plasma into a vacuum," *Phys. Plamsas* **12** (2005) 112102.

[24] P. Mora, "Thin-foil expansion into a vacuum," *Phys. Rev. E* **72** (2005) 056401.

[25] D. S. Hey, *Laser-Accelerated Proton Beams: Isochoric Heating and Conversion Efficiency.* PhD thesis, University of California, Davis, 2007.

[26] M. Foord, P. Patel, A. Mackinnon, S. Hatchett, M. Key, B. Lasinski, R. Town, M. Tabak, and S. Wilks, "Mev proton generation and efficiency from an intense laser irradiated foil," *High Energy Density Phys.* **3** (2007) 365–370.

[27] D. Welch *Comput. Phys. Commun.* **164** (2004) 183.

[28] B. Cohen, A. Langdon, and A. Friedman *J. Comput. Phys.* **81** (1989) 151.

[29] E. Williams, R. Berger, R. Drake, A. Rubenchik, B. Bauer, D. Meyerhofer, A. Gaeris, and T. Johnston, "The frequency and damping of ion acoustic waves in hydrocarbon (ch) and two-ion-species plasmas," *Phys. Plasmas* **2** (1995) 129.

[30] M. Borghesi, A. Mackinnon, D. Campbell, D. Hicks, S. Kar, P. Patel, D. Price, L. Romagnani, A. Schiavi, and O. Willi, "Multi-mev proton source investigations in ultraintense laser-foil interactions," *Phys. Rev. Lett.* **92** (2004) 055003.

[31] M. Hegelich, S. Karsch, G. Pretzler, D. Habs, K. Witte, W. Guenther, M. Allen, A. Blazevic, J. Fuchs, J. Gauthier, M. Geissel, P. Audebert, T. Cowan, and M. Roth, "Mev ion jets from short-pulse-laser interaction with thin foils," *Phys. Rev. Lett.* **89** (2002) 085002.

[32] M. Ammosov, N. Delone, and V. Krainov *Sov. Phys. JETP* **64** (1986) 1191.

[33] V. Tikhonchuk, "Interaction of a beam of fast electrons with solids," *Phys. Plasmas* **9** (2002) 1426.

[34] L. Gremillet, F. Amiranoff, S. D. Baton, J.-C. Gauthier, M. Koenig, E. Martinolli, F. Pisani, G. Bonnaud, C. Lebourg, C. Rousseaux, C. Toupin, A. Antonicci, D. Batani, A. Bernardinello, T. Hall, D. Scott, P. Norreys, H. Bandulet, and H. Pépin, "Time-resolved observation of ultrahigh intensity laser-produced electron jets propagating through transparent solid targets," *Phys. Rev. Lett.* **83** (Dec, 1999) 5015–5018.

[35] "www.gafchromic.com." `http://www.gafchromic.com`.

[36] J. Ziegler, "Srim-2003," *Nucl. Instrum. Meth. B* **219-220** (2004) 1027–1036.

[37] S. Bandyopadhyay, D. Neely, G. Gregori, D. C. Carroll, P. McKenna, M. Borghesi, F. Lindau, O. Lundh, C.-G. Wahlstrom, and A. Higginbotham, "Analysis on a wedge-shaped thomson spectrometer for ion studies," tech. rep., Central Laser Facility, CCLRC Rutherford Appleton Laboratory, 2005/2006.

[38] D. Carroll, K. Jones, L. Robson, P. McKenna, S. Bandyopadhyay, P. Brummitt, D. Neely, F. Lindau, O. Lundh, and C.-G. Wahlstrom, "The design, development and use of a novel thomson spectrometer for high resolution ion detection," tech. rep., Central Laser Facility, CCLRC Rutherford Appleton Laboratory, 2005/2006.

[39] M. Mori, M. Kando, A. Pirozhkov, Y. Hayashi, A. Yogo, N. Yoshimura, K. Ogura, M. Nishiuchi, A. Sagisaka, S. Orimo, M. Kado, A. Fukumi, Z. Li, S. Nakamura, A. Noda, and H. Daido, "New detection device for thomson parabola spectrometer for diagnosis of the laser-plasma ion beam," *Plasma and Fusion Research* **1** (2006) 042.

[40] A. Gonzalez, H. Li, M. Mitch, N. Tolk, and D. Duggan, "Energy response of an imaging plate exposed to standard beta sources," *Appl. Radiat. Isotopes* **57** (2002) 875–882.

[41] C. Chen, "Image plates memo." Private Communication.

[42] S. Taniguchi, A. Yamadera, T. Nakamura, and A. Fukumura, "Measurement of radiation tracks for particle and energy identification by using imaging plate," *Nucl. Instrum. Meth. A* **413** (1998) 119–126.

[43] H. Ohuchi and A. Yamadera, "Development of a functional equation to correct fading in imaging plates," *Radiat. Meas.* **35** (2002) 135–142.

[44] M. Thoms, "The quantum efficiency of radiographic imaging with image plates," *Nucl. Instrum. Meth. A* **378** (1996) 598–611.

[45] R. Bennatar, C. Popovics, and R. Sigel, "Polarized light interferometer for laser fusion studies. review of scientific instruments," *Rev. Sci. Instrum.* **50** (1979) 1583–1858.

[46] C. Stoeckl, W. Theobald, T. Sangster, M. Key, P. Patel, B. Zhang, R. Clarke, S. Karsch, and P. Norreys, "Operation of a single-photon-counting x-ray charge-coupled device camera spectrometer in a petawatt environment," *Rev. Sci. Instrum.* **75** (2004) 3705.

[47] F. Ewald, H. Schwoerer, and R. Sauerbrey, "Kα-radiation from relativistic laser-produced plasmas," *Europhys. Lett.* **60** (2002) 710–716.

[48] M. Temporal and J. Honrubia, "Numerical study of fast ignition of ablatively imploded deuterium-tritium fusion capsules by ultra-intense proton beams," *Phys. Plasmas* **9** (2002) 3098.

[49] M. Temporal, "Fast ignition of a compressed inertial confinement fusion hemispherical capsule by two proton beams," *Phys. Plasmas* **13** (2006) 122704.

[50] M. M. Allen, *Ion Acceleration from the Interaction of Ultra-Intense Lasers with Solid Foils.* PhD thesis, University of California, Berkeley, 2004.

[51] M. Hegelich, B. Albright, P. Audebert, S. Karsch, A. Blazevic, E. Brambrink, J. Cobble, T. Cowan, J. Fuchs, J. Gauthier, C. Gautier, M. Geissel, D. Habs, R. Johnson, S. Karsch, A. Kemp, S. Letzring, M. Roth, U. Schramm, J. Schreiber, K. Witte, and J. Fernandez, "Spectal properties of laser-accelerated mid-z mev/u ion beams," *Phys. Plamsas* **12** (2005) 056314.

[52] M. C.D. Chen, "T-hot cannon x-ray inference." Privat Communication.

[53] L. V. Woerkom, K. Akli, T. Bartal, F. Beg, S. Chawla, C. Chen, E. Chowdhury, R. Freeman, D. Hey, M. Key, J. King, A. Link, T. Ma, A. M. an A.G. MacPhee, D. Offermann, V. Ovchinnikov, P. Patel, D. Schumacher, R. Stephen, and Y. Tsui, "Fast electron generation in cones with ultraintense laser pulses," *Phys. Plasmas* **15** (2008) 056304.

[54] "National institute of standards and technology." `http://www.nist.gov`.

[55] T. Carlson, N. Wasserman, J. McDowell, and C. Nestor, "Comprehensive calculation of ionization potentials and binding energies for mulitply-charged ions," tech. rep., Oak Rdige National Laboratory, 1970.

[56] "The flexible atomic code." `http://http://kipac-tree.stanford.edu/fac`.